To go with the flow: Molecular motors are a drag

Houtman, D.

Publication date
2013
Document Version
Final published version

Citation for published version (APA):
Houtman, D. (2013). *To go with the flow: Molecular motors are a drag*. [Thesis, externally prepared, Universiteit van Amsterdam].

ISBN 978-94-6203-460-0

To go with the flow – Molecular motors are a drag

Dion Houtman

To go with the flow –
Molecular motors are a drag

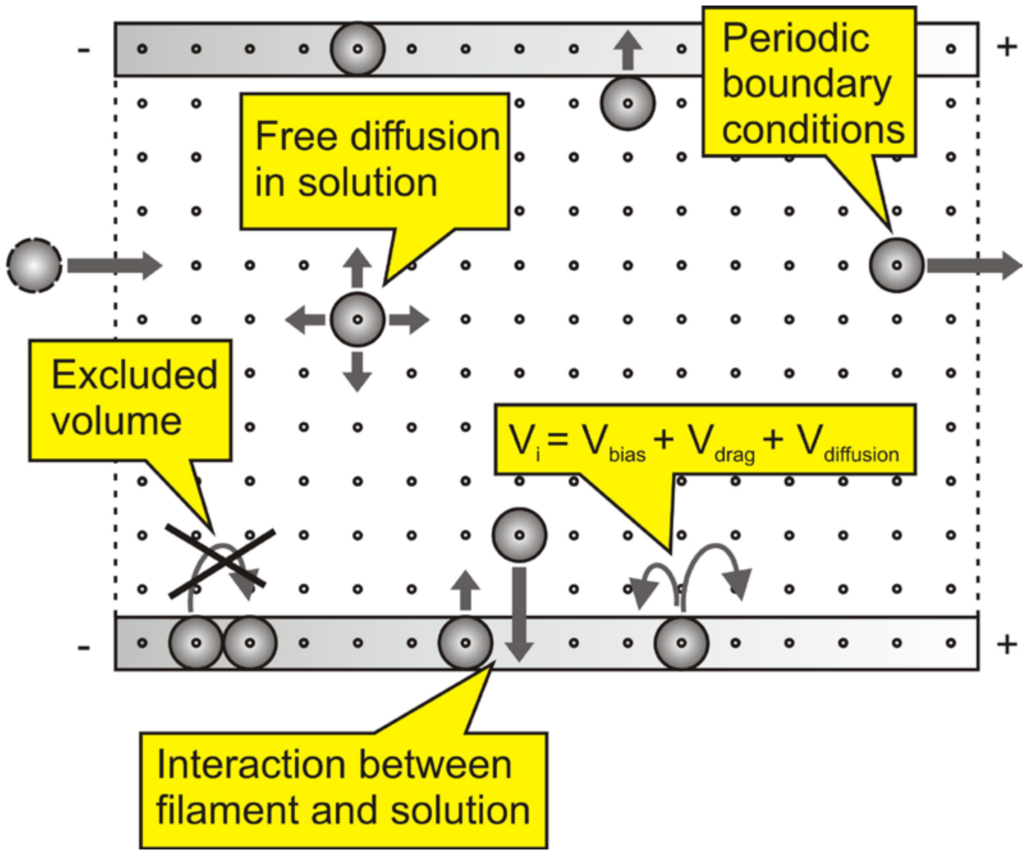

Dion Houtman

To go with the flow
Molecular Motors are a drag

ACADEMISCH PROEFSCHRIFT

ter verkrijging van de graad van doctor
aan de Universiteit van Amsterdam
op gezag van de Rector Magnificus
prof. dr. D.C. van den Boom
ten overstaan van een door het college voor promoties ingestelde
commissie, in het openbaar te verdedigen in de Agnietenkapel
op maandag 11 november 2013, te 14:00 uur

door

Dion Houtman

geboren te Haarlem

Promotor: Prof. dr. E. J. Meijer
Co-promotor: dr. E. Eiser

Overige Leden: Prof. dr. ir. P. J. Schoenmakers
Prof. dr. I. Pagonabarraga
Prof. dr. A. M. C. Emons
Prof. dr. A. M. Brouwer
dr. C. P. Lowe
dr. C. Storm

Faculteit der Natuurwetenschappen, Wiskunde en Informatica

Typeset by LaTeX
Printed and bound by WÖHRMANN PRINT SERVICE
Cover design by Dion Houtman

ISBN: 978-94-6203-460-0

Front Cover: Schematic view of the model system that is described using computer simulations, i.e. a cytoplasmic strand in a plant cell. A solution is embedded between two bio-filaments and mapped on a lattice. Molecular motors carrying organelles move from one lattice node to another. Reproduced with kind permission from EPL (Europhysics Letters) - IOPscience after D. Houtman et al., "Hydrodynamic flow caused by active transport along cytoskeletal elements" *EPL*, 78:18001, 2007.

Contents

Chapter 1

Background Molecular Motors

Processive molecular motors are proteins that derive their name from the fact that they facilitate directed motion. This means they can overcome the stochastic forces that cause Brownian motion. The number of molecular motor proteins in animal and plant cells known to us today ranges in the hundreds but it can be reduced to three families: kinesin, dynein and myosin. There can be many different molecular motors present in one organism, for example in the plant *Arabidopsis thalina* 61 kinesin and 17 myosin motors have been reported [1]. In order to be able to perform directed motion against the omnipresent Brownian forces, motors need to bind to cytoskeletal filaments inside the cell. Kinesin and dynein are associated with motion along microtubules that are an integral part of the cytoskeleton and are essential for mitosis (cell division), vesicle transport and many other processes. Myosin is an actin-related molecular motor: it is mainly known for driving the contractile motion in muscles [2,3]. Moreover, molecular motors are important in the perpetual polymerisation and depolymerisation of actin filaments that gives cells the ability to move on surfaces, and bacteria like *Listeria monocytogenes* to move from one cell to another [4].

In this thesis I am interested in the effect of viscous drag on vesicle transport by processive molecular motors. Therefore, I focus in this chapter only on kinesin and dynein transporting vesicles along microtubules and myosin that are responsible for organelle transport along actin filaments. I am interested in the specific situation of directed transport of organelles and vesicles that is observed in neurons and in cytoplasmic streaming, which takes place mainly in plant cells. In such systems, I study the viscous drag on motors with cargoes and the hydrodynamic interaction with other motors, their cargoes and suspended objects. In order to address questions about the forces needed to move any cargo along a filament embedded in a highly viscous solution and whether the hydrodynamic coupling between motors and the solvent is relevant for fast transport in cells, I give here a brief review over experimental findings.

Fast Vesicle Transport - Experimental Facts

Fast vesicle transport was mainly observed and studied in neurons and plant cells. In neurons or neurites (projections from the neuron, which can be either a dendrite or axon) vesicle transport is provided by kinesin and dynein motors moving along tubulin filaments. In plant cells, this fast transport is associated with the ”streaming” of organelles dragged along actin filaments by myosin motors. Organelle is the generic name of small self-contained objects with specific functions that are found inside the cells. Examples are the power generating mitochondria in eukaryotic cells and chloroplast that provides photosynthesis in plants and algae. Fast streaming of organelles inside cells is called *cytoplasmic streaming* [5,6].

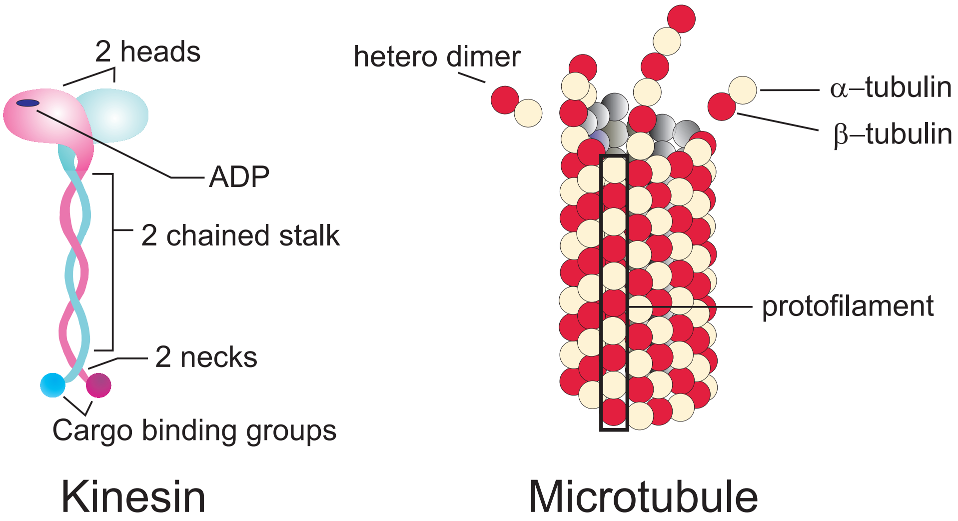

Figure 1.1: *Schematic illustration of kinesin (3kin) and a microtubule. Left: The kinesin shown here is composed of two chains. The top part contains the two head groups also known as motor domains (*$\approx$*10 nm long). The intertwined chains are called flexible stalk. It differs from one motor group to another and can also be absent. The stalk is terminated by a group that can bind to vesicles or organelles. Right: Structure of microtubules. The basic building units are the hetero dimers that are made of an* α*- and* β*-tubulin, both being proteins. These polymerise to form a protofilament. Latter self-assemble into microtubules that can grow and shrink continuously, depending on the ATP concentration and forces acting on it. Note that there is only one site per tubulin dimer for a kinesin head to bind to a microtubule [7].*

The Kinesin-Microtubule Complex In *In Vitro* Experiments And In Neurites

All molecular motors derive their motion from hydrolysing adenosine triphosphate (ATP), thereby undergoing a series of conformational changes. How molecular motors move along a bio-filament, which mechanical and viscous forces are involved, and whether they work cooperatively has been intensively studied only in the past twenty years, when optical trap and fibre measurements with nanometre and piconewton sensitivity became available [8, 9]. Svoboda et al. [10] developed an optical-tweezers tool to show that kinesin moves with 8 nm steps along microtubules, hydrolysing with each step an ATP. This step distance is independent of ATP-concentration and load [11]. The motors move with a unidirectional bias corresponding to the polarity of the microtubules, but the underlying physical mechanism has not yet been fully understood [12]. All bio-filaments have a polarisation because of their asymmetric building units (Fig.1.1) leading to a (+) and (-) end. Most kinesins walk toward the (+) end that grows away from the nucleus, while dynein moves to the (-) end. The 8 nm steps kinesin takes correspond also to the spacing of the dimers forming the protofilaments in microtubules (Fig.1.2).

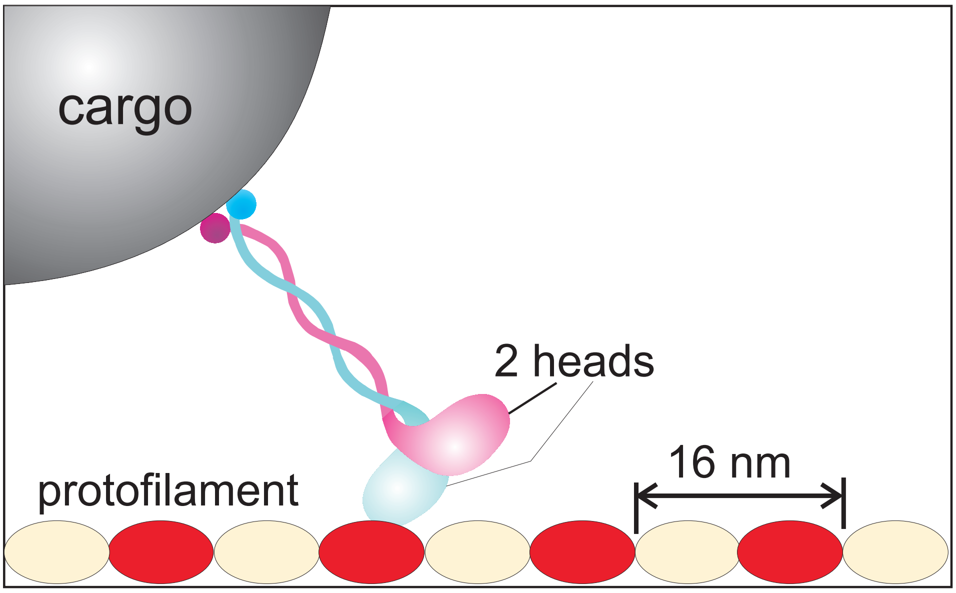

Figure 1.2: *Schematic illustration of kinesin pulling a cargo over a microtubule by taking 8 nm steps. It is believed that the two headed motor domain moves in an asymmetric hand-over-hand fashion [13].*

In contrast to muscle myosin that is known to attach to actin filament, pulling it with one stroke while consuming an ATP, and then releasing it, kinesin is a *processive motor*. This means that, because of kinesin's double-head structure, it can stay attached to the microtubule with one head while moving ahead with the other to the next binding site. In this way it can move along the microtubule many steps before detaching. The distances a kinesin motor can travel in this way can be as large as 5 ± 2 μm, corresponding to 200 - 1000 cycles of ATP. [14]

In 1995 Meyhöfer and Howard [15] performed experiments where kinesins are attached to a glass slide such that their head group is pointing into the solution containing microtubules and ATP. One end of a microtubule was attached to the end of a flexible glass fibre, whose deflection was detected with optical means, allowing to measure the forces generated by a single kinesin molecule binding to the microtubule (Fig.1.1). The force required to stall a single kinesin molecule was 5.4 ± 1.0 pN. Further gliding experiments revealed that a single kinesin molecule can move an attached bead with a speed of about 800 nm/s when the opposing force is smaller than 1 pN [10, 15–17]. However, in order to understand organelle transport in cells one needs to address several other questions. It is known that the size of organelles can vary between tens of nanometres and a few micrometres (see table 1.1 for a number of identified organelles).

Organelle	**Size in nm**	**Reference**
Lysosomes	100-500	[18]
Peroxisomes	150-300	[19]
Endosomes	$\leq$ 500	[20]
Melanosomes	± 500	[21]
Mitochondria	$\leq$ 800	[22]

Table 1.1: *Typical sizes of organelles found in cells.*

Hence, one may ask how the load on a single motor varies for such differently sized cargoes? The main force the motor will have to overcome is the drag force, F_d, it experiences while moving through a viscous medium. Using Stokes' formula [3], $F_\mathrm{d} = 6\pi\eta a v$ (η is the viscosity of the surrounding fluid, a the particle radius and v the velocity of the cargo), the drag force of a vesicle of 1 μm, moving at 800 nm/s, would be 0.02 pN, assuming the inside of the cell has the viscosity of water (η = 0.001 Pas). This is much smaller than the 1 pN force applied in Howard's *in vitro* gliding assays. Thus one can conclude that the drag forces on vesicles in pure water is negligible. However, in real cells the viscosity can be up to three orders of magnitude larger [23–26]. In that case the load on a single motor molecule can become comparable to the force a single motor can execute in one ATP hydrolysing step. Indeed, if the calculation is repeated for a similar vesicle in a *HeLa*-cell[*] (η = 0.398 Pas; calculated from data in [26]) a drag force of 6 pN is found. Hence, when the load becomes larger than the stall force on a single kinesin molecule, the question arises whether more than one motor will be needed to pull vesicles. Ashkin et al. [28] and Hirokawa [29] used electron microscopy imaging on fixed cells to show that some vesicles were attached to the microtubules by 2 - 3 kinesin molecules. Moreover, Tominaga et al. [30] found that 1 μm sized particles can be dragged by two to three processive myosin XI motors along actin filaments. And also an *in vivo* study on organelle transport along microtubules in *Xenopus* melanophores[†] supports the hypothesis that organelle transport involves cooperativity between multiple motors [31].

Another important question follows from the discussion above, namely whether the velocity of a kinesin-driven vesicle (or myosin-driven organelle) is independent of the number of active motors. Several optical trap measurements on single motor interactions with a filament [15,17,32] show that their velocity decreases as the opposing load increases from 1 pN to 10 pN (Fig. 1.3 - Left). For loads of 1-20 pN the vesicle velocity is expected to increase with the number of motors attaching to the vesicle and the microtubule [33]. However, gliding-assay experiments with very high force resolution also show that below a certain load ($<$ 1 pN) the velocity of the transported vesicles becomes independent of the load [34].

Most motility measurements mentioned so far were based on *in vitro* measurements. Already in 1992, Allen et al. [37] measured directly fast transport of vesicles in axons. They found that particles of 50-100 nm in size moved with about 2.5 μm/s, while the average velocity of larger vesicles (0.4-2.5 μm) dropped to 1 μm/s. Moreover, they observed that intermediate sized particles moved in an irregular fashion (called saltatory motion [38–40]): Following a vesicle in time, one can observe that it can move with a given velocity, then stop for a moment and subsequently continue moving in the same direction but with a different velocity. Recent experiments *in vivo* confirm that vesicles alternate between periods of directional and non-directional movement, suggesting that there are periods where a vesicle follows a cytoskeletal track and periods where it diffuses freely [24]. Another *in vivo* study by Hill et al. [23] focused on this random motion and in particular the effect of viscous drag on the speed of vesicle transport in greater detail using time-resolved optical microscopy and micro-rheology *in vivo*. The latter experiment provided a measure for the viscosity that vesicles experience in the cytoplasm of PC12 neurites[‡]. Hill and co-workers found that the PC12 cytoplasm is shear thinning but shows a plateau value in viscosity of about 1.1 $\pm$ 0.25 Pas at small frequencies, which is about a thousand times larger than the buffer solutions used in gliding assays.

---

[*] The HeLa-cell line was derived from cervical cancer cells taken from Henrietta Lacks, a patient who eventually died of her cancer [27].

[†] Pigmented cells of the African clawed frog.

[‡] PC12 is a culture of cancer cells from the adrenal gland of rats.

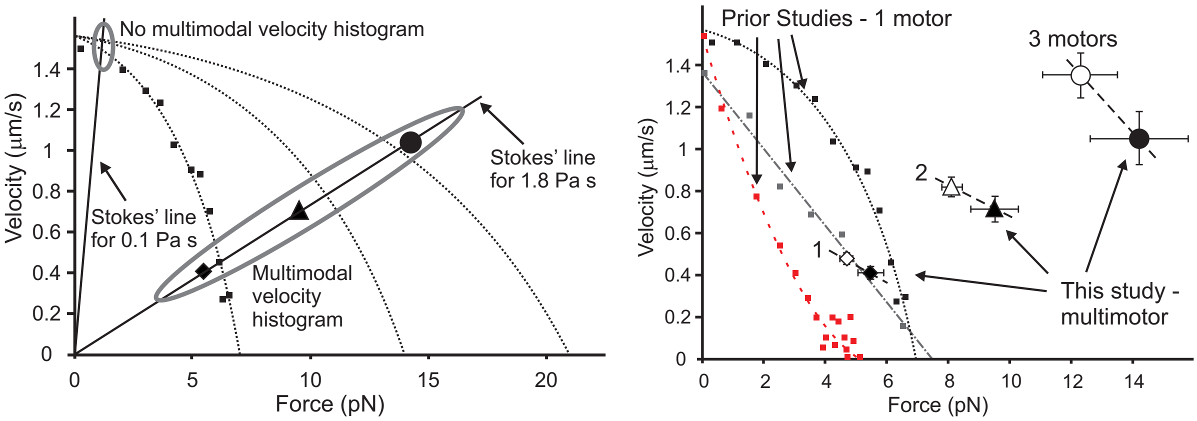

Figure 1.3: *Left - Velocity of vesicles or colloidal probe beads dragged along microtubules by kinesin motors, reproduced from ref. [25], who extended the original figure from [23]. The dots represent experimental data by [17]. The large closed symbols represent experimental data for 1, 2 and 3 motors attached to vesicles of 0.40, 0.36 and 0.40 μm respectively, measured in vivo in NT2 cells. The curves for 2 and 3 kinesin motors are estimates extracted from bead assays, assuming that the load is equally shared by the motors. Two straight lines correspond to Stokes' law for systems with viscosity of 0.1 Pas and 1.8 Pas respectively for a vesicle of 0.4 μm. The contribution of multiple motors is negligible at the low viscosity. For the viscous fluid the force generated by the attached motors is additive. Right - The force-velocity curves from earlier single motor studies (red [15]; grey [35]; black [17]) are compared with multiple motor data [25]. To compare data obtained at different temperatures, it was scaled according to a previously determined Arrhenius equation [36]. Open symbols refer to average vesicle radii of 0.29, 0.29 and 0.26 μm. The black data are the same as in the figure to the left. Note that the smaller vesicles move faster as the acting hydrodynamic drag force is smaller. Both images are reproduced after [25] with kind permission from Springer Science and Business Media.*

Furthermore, the vesicles ($a \approx 0.35$ μm) they studied moved with velocities fluctuating between 0.45 μm/s and 2.1 μm/s at loads varying between 4-15 pN. These irregular velocities may be due to the fact that the viscosity may vary throughout the cell cytoplasm, as it contains many other bio-macromolecules that need not be dispersed homogeneously. The saltatory motion may also be due to the fact that microtubules are not continuous throughout the neurites or axons. Thus a vesicle may encounter gaps in its "track" that can be viewed as broken bridges that have to be overcome. In order to continue their way in the same direction one may hypothesise that it would not be advantageous for motors to reach the other side of the gap purely by diffusion. In this thesis I show that the hydrodynamic coupling between cooperatively moving molecular motors and their cargo may provide a mechanism that helps the vesicles to bridge those gaps (see chapter 4). But also the fast transport of organelles in plants (that is described in the following paragraph) may be understood better when hydrodynamics is taken into account.

Recently it became possible, using quantum dots as markers, to follow the molecular motors *in vivo* directly and construct force-velocity curves (Fig.1.3 - Right). Peaks in the measured velocities suggest that the velocities are constrained to quantised values. A hypothesis has been proposed that each peak represents a different number of motors pulling a vesicle through a viscous solution [25, 31, 41, 42]. An alternative hypothesis is presented by Cai et al. [43] who studied transport in COS-cells*. They suggest that the difference in velocity comes from the presence of different members of the kinesin family with distinct kinetic properties. However, the near integer difference in value between measured drag forces [23, 25, 31] suggest identical motors (see Fig.1.3 - Right). Recent *in vitro* experiments in a medium with a viscosity 1000× that of water showed that numbers of kinesins cooperate when pulling against a viscoelastic drag [45], supporting the cooperativity hypothesis.

Myosin Driven Organelle Transport in Plant Cells

As the aim of this thesis is to study the influence of hydrodynamic interactions on fast organelle transport in cells it is interesting to first identify the situations in which hydrodynamic interactions may play a role. Fast organelle transport is mainly important in plant cells, where it is observed as cytoplasmic streaming [6, 46, 47]. The velocities measured in cytoplasmic streaming exceed those measured for vesicles dragged by kinesins along microtubules in animal cells, and is associated with myosin-actin complexes (Fig.1.4) [48]. Note, however, that kinesin-microtubule assisted organelle transport has also been reported in plants [49]. While many myosins, e.g. the muscle motor myosin II, are non-processive, processive plant myosins have been identified: myosin V, VI, VIII, XI, and XIII [50]. Amongst these groups further variations are known that depend on the species and on the vesicle-binding groups. Myosin walks to the barbed (plus) end of actin filaments with the exception of myosin VI that walks towards the pointed (minus) end [50–52]. An example of these processive myosin are the myosins that are extracted from the alga *Chara corallina*. In *in vitro* motility assays these motors move along actin filaments with a speed of 40-60 μm/s [48, 53] and up to 100 μm/s *in vivo* [5].

Tominaga and co-workers [30] were the first to use gliding assays to measure the motility (movements) of myosin XI extracted from tobacco bright yellow-2 cells of *Nicotiana tabacum* (BY-2 cells). They anchored actin filaments on a glass slide and measured the velocity of a myosin XI coated colloidal bead attaching to the actin filament under different loads. The load was controlled by optical tweezers. They observed a maximum speed of 7 μm/s and determined the step length to be of about 35 nm, a distance very close to that of a repeat unit along F-actin (Fig.1.4).

---

*Cells derived from the kidney cells of the African green monkey with a version of the SV40 genome that can produce large T antigen but has a defect in genomic replication [44].

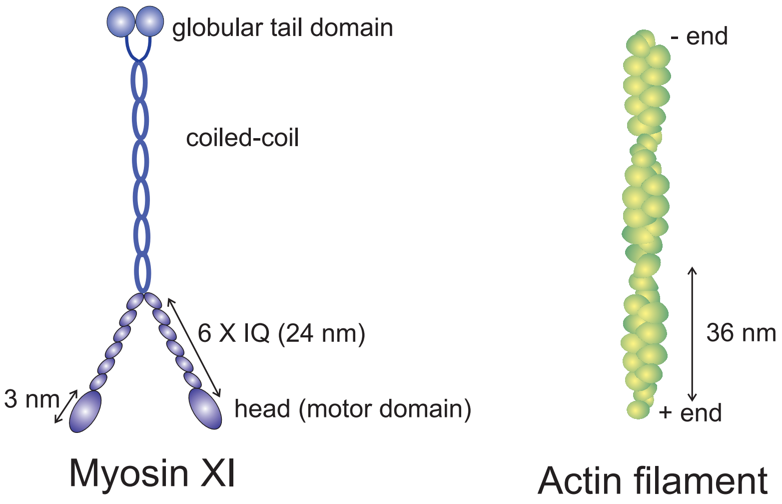

Figure 1.4: *Left: Schematic representation of the dimer myosin XI, redrawn from reference [53]. The head group (heavy chain) binds to the actin filament and contains the ATP binding centre. The head group is followed by the neck region that contains varying binding sites for light chains. In myosin XI the neck contains 6 so-called IQ motives, which bind in turn the protein calmodulin (a calcium binding agent). The neck region is followed here by a* α*-helical coiled-coil region that carries a cargo binding domain. Right: Filamentous or F-actin has a helical structure and is made of two protofilaments that are build up of globular or G-actin. F-actin is about 7 nm thick and has a 36 nm helical repeat structure. Myosin XI slides processively along F-actin in 35 nm steps, toward the plus end [30].*

As mentioned above the hydrodynamic drag on a micron-sized organelle is not much less than the stall force, which supports previous experimental findings that fast transport of organelles must relay on cooperative motion of molecular motors. Furthermore, fast organelle transport sets up a hydrodynamic flow. The latter term refers to the fact that the hydrodynamic flow generated by cytoplasmic streaming also enables the transport of unbound small-molecule nutrients and building material, thereby enabling a rapid supply throughout the large cells [54]. Finally, as mentioned before, organelles move faster *in vivo* than *in vitro*. I will show using the simulations described in chapters 4 and 6 that the organelle velocities are increased via the hydrodynamic coupling between motors. From experiments it is known that when a positive force is exerted on a motor they start moving faster (Kinesin [11]; Myosin-V [55]), the hydrodynamic coupling gives rise to such a force. The simulation results are supported with experimental work in chapter 5.

Chapter 2

Hydrodynamics At Low Reynolds Numbers

Introduction

In the previous chapter molecular motors and their cargoes were introduced. These motors are capable of dragging a cargo through a cell by walking along cytoskeletal filaments. The transport takes place through cytosol, the fluid component of cytoplasm. This fluid has a viscosity a factor 1000 larger than water. Moreover, as their name suggests, the motor proteins are small and their cargoes not much bigger ($\leq 2\mu$m) (see table 1.1), which means that they are subject to thermal forces. As explained in the previous chapter, transport of cargoes by single motors through water has been studied intensively *in vitro* [3, 10, 14–17, 55]. In addition, the first force-velocity curves *in vivo* [23–26, 56] have been reported following the recent introduction of quantum dots as positional markers for molecular motors. None of these studies however, focus on the situation where multiple cargoes are simultaneously transported in the same direction as is the case in cytoplasmic streaming and inside neurons. In this thesis, I reason that this transport is strongly affected by the medium in which it takes place. The larger the fluid's resistance against flowing, i.e. the viscosity, the smaller the influence of thermal forces, and thus, the more efficient the directed transport takes place. Moreover, the actively moving motor-cargo complexes set up a flow field via momentum transfer. I will show in subsequent chapters that the hydrodynamic interactions via momentum transfer between motor-cargo complexes moving in the same direction enhances their transport.

In this chapter the underlying physics will be explained. Firstly, the fluid friction is introduced via the viscosity. Secondly, the equations of continuity and motion, which describe respectively the conservation of mass and momentum in a fluid, are discussed. Next, the interaction of a typical organelle of size 500 nm with the surrounding fluid is studied. This includes quantifying the relevant forces acting upon the suspended organelle and discussing these by means of dimensionless parameters such as the Reynolds, Péclet and Stokes numbers. In addition, momentum transfer through the fluid around one organelle, and between many organelles is discussed. Finally, the Langevin equation, the equation of motion for a suspended organelle, is introduced.

The Viscosity

The concept of viscosity can be understood by means of the two parallel plates experiment (see Fig.2.1). In this experiment a net force is acting on the top plate forcing it to move forward while the bottom plate remains in position. As explained in the figure, a linear velocity profile arises for a *Newtonian fluid* which falls off with the distance, x, away from the moving plate. Assuming no-slip boundary conditions the fluid velocity, V, has a maximum value at the moving plate and is zero at the other one. For this linear velocity profile to arise the flow has to be laminar [57]. In this regime the adjacent fluid layers slide past one another in an orderly fashion i.e. there is no turbulence. I will now introduce the viscous stress, τ, which is the force, F, acting on the plate divided by its area A. In the parallel plates experiment, the viscous stress is a measure for the flux in x-momentum in the y-direction and is given by [57]:

$$\tau = \frac{F}{A} = -\eta \frac{\mathrm{d}V_{\mathrm{x}}(y)}{\mathrm{d}y}. \tag{2.1}$$

This equation states that the shearing force per unit area is proportional to the velocity gradient. The velocity gradient is the driving force for momentum transport by viscous forces. The momentum goes downhill from a region of high to low velocity. Viscous forces are only present when velocity gradients are present. The constant of proportionality is called the viscosity, η, which is the internal resistance of a fluid against flowing. It is fluid dependent and for a *Newtonian fluid*, it is sensitive to the temperature and concentration but not to the velocity gradient. For liquids, the viscosity decreases with increasing temperature. A common deviation from Newtonian behaviour is shear thinning, the tendency for the viscosity to decrease at high velocity gradients [3].

The full expression for the viscous stress in three dimensions is given by *Newton's law of viscosity* [57]:

$$\boldsymbol{\tau} = -\eta \left[\nabla \boldsymbol{V} + (\nabla \boldsymbol{V})^{T}\right] + \left(\frac{2}{3}\eta - \kappa\right) (\nabla \cdot \boldsymbol{V})\, \boldsymbol{\delta}. \tag{2.2}$$

Here, $\boldsymbol{\tau}$, is the viscous stress tensor, $\boldsymbol{V}$, the velocity vector and, κ, the bulk viscosity. The *nabla operator* ∇ is defined as: $\nabla \equiv (\partial/\partial x, \partial/\partial y, \partial/\partial z)$ and δ is the *Kronecker delta* which has the value one for $i = j$ and zero for $i \neq j$. The right hand term can often

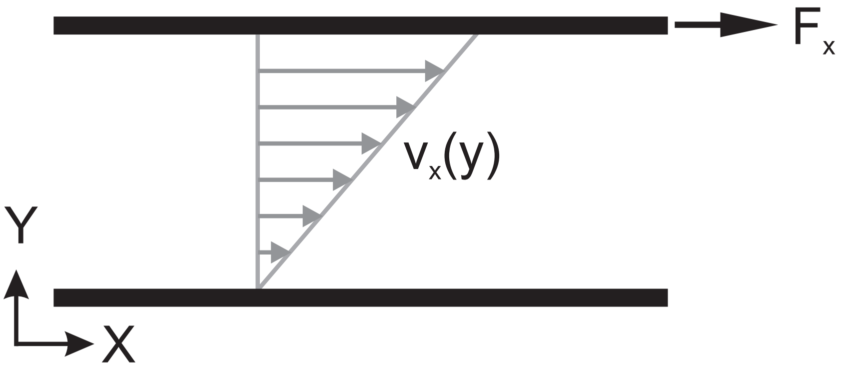

Figure 2.1: *Two parallel plates experiment [3,57] - A force, F_x, acting on the top plate causes it to move forward with velocity, V_x, while the bottom plate remains in position. Momentum is transferred into the fluid in the direction perpendicular to the moving plate. I assume the fluid to be Newtonian and no-slip boundary conditions at the plates. This yields the characteristic linear velocity distribution, where the fluid velocity falls off from a maximum value at the top plate to zero velocity at the bottom one. The constant of proportionality is the viscosity η.*

be ignored as $\kappa = 0$ for ideal gases and $(\nabla \cdot \boldsymbol{V}) = 0$ for incompressible fluids (see next section) [57].

In addition to momentum transfer by the shear forces, there are also hydrostatic pressure forces acting on the fluid. These are given by $p\boldsymbol{\delta}$. The combining of the momentum contributions yields the molecular stress tensor $\boldsymbol{\Pi}$ [57]:

$$\boldsymbol{\Pi} = \boldsymbol{\tau} + p\boldsymbol{\delta} \tag{2.3}$$

This tensor can be interpreted as the flux of all molecular j-momentum in any positive i-direction.

Balance Equations In Fluid Dynamics

Two balance equations, which describe fluids, are important for understanding the theory in this thesis. Firstly, the balance equation of mass can be obtained by considering the change of fluid density, ρ_l, at a given time, t, in space. The equation of continuity is given by [57]:

$$\frac{\partial \rho_l}{\partial t} + \nabla \cdot (\rho_l \boldsymbol{V}) = 0. \tag{2.4}$$

For incompressible fluids, i.e. a fluid of constant density, this can be simplified to [57]:

$$(\nabla \cdot \boldsymbol{V}) = 0. \tag{2.5}$$

Secondly, there is the equation of motion for fluids, which is the fluid's version of *Newton's second law*. The equation describes the rate of momentum increase for a fluid at a given place and time. This momentum increase arises from external forces such as gravity, $\boldsymbol{g}$, and from the gradient of all momentum transfer. The latter consists of the molecular stress tensor, $\mathbf{\Pi}$ (see eq.2.3), and convective momentum, $\rho_l \boldsymbol{V}\boldsymbol{V}$, which is the momentum carried by the fluid. The combination yields the Navier-Stokes equation [57]:

$$\frac{\partial \left(\rho_l \boldsymbol{V}\right)}{\partial t} = -\left[\nabla \cdot \rho_l \boldsymbol{V}\boldsymbol{V}\right] - \nabla p - \left[\nabla \cdot \boldsymbol{\tau}\right] + \rho_l \boldsymbol{g}. \tag{2.6}$$

The Reynolds Number

In equation 2.7, the Navier-Stokes equation is rearranged such that all the terms containing inertia are on the left-hand side of the equation.

$$\rho_l \left(\frac{\partial \boldsymbol{V}}{\partial t} + \boldsymbol{V} \cdot \nabla \boldsymbol{V}\right) = -\nabla p + \eta \nabla^2 \boldsymbol{V} + \rho_l \boldsymbol{g}. \tag{2.7}$$

The term, $\frac{\partial \boldsymbol{V}}{\partial t}$, represents changes in inertia in time, whereas, the non-linear term, $\boldsymbol{V} \cdot \nabla \boldsymbol{V}$, represents the momentum carried by the fluid flow. Inertia is the property of an object to remain at constant velocity unless an external net force is acting upon it. The larger the inertia of an object, the more difficult it is to stop its movement. In contrast, an object of low inertia will instantaneously stop or start when an external force is applied upon it. Inertia in fluid flows is caused by non-linear interactions within the flow field. When inertial effects dominate the flow, the non-linear interactions may give rise to instabilities causing the fluid to become turbulent.

The pressure gradient, ∇p, viscous forces, $\eta \nabla^2 \boldsymbol{V}$, and the influence of gravity, $\rho_l \boldsymbol{g}$ (or other external forces such as centrifugal or electromagnetic forces) are on the right-hand side of the equation. The viscous term includes the fluid viscosity. As explained in the moving plate experiment (Fig. 2.1), the viscosity is a fluid dependent variable involved in momentum transport. Each fluid has a different viscosity depending on how strongly this fluid resists flow under the influence of an external force. For example, air has low viscosity (19×10^{-6} Pas [57]), water is intermediate (0.01 Pas [57]) and cytosol is high (1 Pas [23]). Furthermore, the viscosity is the source of drag on objects moving through a fluid. Inertia and viscosity work against each other. While inertia is trying to keep an object moving, viscosity is trying to stop it [58].

If we introduce a velocity, U, and length, L, time can be represented time as L/U and the gradient, ∇, as $1/L$. Next, it is possible to express inertia and viscosity using these units. Both terms containing inertia can be expressed as $\rho \frac{U^2}{L}$ and the viscosity as $\frac{\eta U}{L^2}$ [58].

If we now take the ratio of the inertial and viscous contributions in the Navier-Stokes equation, we obtain the Reynolds number [57–60]:

$$Re = \frac{\text{inertial forces}}{\text{viscous forces}} = \frac{\rho U L}{\eta}. \tag{2.8}$$

This is a dimensionless number that characterises different flow regimes arising when the fluid medium comes in contact with an interface. Most commonly, this is a solid interface as is the case for flow through a pipe or channel of any arbitrary shape, or flow around a suspended object e.g. a sphere. At low Reynolds numbers, viscous forces are dominant. The flow is laminar and it is characterised by smooth constant fluid motion. High Reynolds numbers occur when inertial forces dominate, which tend to give rise to chaotic fluid behaviour like eddies and vortices. When considering flow around an object, the Reynolds number is an indicator for vortex shedding behind the particle. In table 2.1 examples of Reynolds numbers are given.

Object	**Size** m	**Speed** m/s	**Fluid density** kg/m^3	**Viscosity** Pas	**Reynolds No.**
Ocean liner	100	30	1000	10^{-3}	3×10^{9}
Swimmer	2	1	1000	10^{-3}	2×10^{6}
Bee	10×10^{-3}	0.14	1.3	18×10^{-6}	100
Bacterium	2×10^{-6}	25×10^{-6}	1000	10^{-3}	5×10^{-5}
Melanosome*	5×10^{-7}	8×10^{-7}	1200	1.1	4.4×10^{-10}

Table 2.1: *The flow behaviour of different objects are compared using the Reynolds number, Re. This number is the ratio between inertial forces working on an object in a fluid and the viscous forces acting upon it. It is given by:* $Re=\rho V d/\eta$ *where* η*, is the viscosity,* ρ*, the density,* V*, the velocity and,* d*, the diameter of the object. Reynolds numbers larger than one correspond to a turbulent regime while smaller values refer to laminar flow. This table was reproduced after [3]. *The melanosome, a typical molecular motor cargo, was added to the original table, for references see table 2.2.*

Flow At Low Reynolds Numbers - Why We Need Molecular Transport Motors?

As can be seen in table 2.1, the Reynolds number of a melanosome, a typical organelle, is very small. I will use this typical motor cargo for molecular motors as frame of reference. The properties of this organelle are summarised in table 2.2, where the viscosity of cytosol is 1.1 Pas [23]. When Reynolds numbers are this small, friction forces are significantly larger than inertial forces and the latter can therefore be neglected. Additionally, the gravitational force, $\boldsymbol{F}_{\mathrm{g}}$, is given by [3]:

$$\boldsymbol{F}_{\mathrm{g}} = m\boldsymbol{g}. \tag{2.9}$$

In this equation, m, is the mass of the organelle and, $\boldsymbol{g}$, the gravitational constant. Using this equation we can show that for the melanosome (see table 2.2) the gravitational force is small (0.00077 pN) even in comparison to the stall force of a molecular motor (5-7 pN). Next, we assume that there are no external forces acting on the fluid, that the influence of gravity can be neglected, the fluid is incompressible and the fluid viscosity and density are constants. Thus, the Navier-Stokes equation can be simplified to the *Stokes* or *Creep flow equation* given by [57,59,60]:

$$\eta\nabla^2\boldsymbol{V} - \nabla p = \boldsymbol{0}. \tag{2.10}$$

Unlike the Navier-Stokes equation, this is a linear equation that has no contributions from inertial forces and it is time reversible. The following example illustrates the significance of the absence of inertia. In his book, Howard [3] derives an equation for calculating the coasting distance of an object after the force acting on it has been removed:

$$L_{\mathrm{c}} = V_0\tau. \tag{2.11}$$

In this equation, L_{c}, is the coasting distance, V_0, the velocity at $t = 0$ and, τ, the typical time an object takes to reach its terminal velocity (relaxation time). For an organelle, without an external force acting upon it, the terminal velocity is zero. The relaxation time is defined as [3,63]:

$$\tau = \frac{m}{\gamma} = \frac{2a^2\rho}{9\eta}. \tag{2.12}$$

Moreover, m, is the mass of the object and, γ, is the fluid drag coefficient (See eq.2.19). For the organelle in table 2.2, this means that it reaches a full stop after coasting $1.94{\times}10^{-13}$ m in $1.52{\times}10^{-11}$ s. This shows that in a system without inertia, changes in velocity are instantaneous.

For organelles and molecular motors the time reversibility of the Stokes equation has nontrivial consequences. To illustrate this, Purcell introduced *the Scallop Theorem* [64,65]. The theorem states that symmetrical motion cannot generate a net displacement at low Reynolds numbers. In Purcell's example a scallop quickly closes its shell, generating enough momentum to propel itself. However, upon opening of the shell, independent of the speed of opening, the trajectory is reversed and the scallop is returned to its original position. This is a direct consequence of the symmetrical path followed by the

Property	Symbol	Value	Comment
Motor cargo			
Diameter	d	500×10^{-9} m	[21]
Volume*	V	6.54×10^{-20} m^3	
Density	ρ	1200 kg/m^3	[61]
Mass*	m	7.85×10^{-17} kg	
Viscosity	η	1.1 Pas	[23]
Minimum Motor Force*	F_0	4.15 pN	$F_0 = \gamma V_0$
Velocity	V_0	800 nm/s	[17,62]
Temperature	T	37 °C	
Boltzmann Constant	k_b	1.381×10^{-23} J/K	
Thermal Energy* (T in K)	$k_\mathrm{b}T$	4.2821×10^{-21} J	
Acceleration of gravity	g	9.81 m/s^2	
Reynolds Number*	Re	4.36×10^{-10}	eq. 2.8
Stokes Number*	S_k	4.85×10^{-11}	eq. 2.27
Drag coefficient*	γ	5.18×10^{-6} Ns/m	eq. 2.19
Mobility* (=1/γ)	μ_0	1.93×10^{5} m/Ns	eq. 2.19
Diffusion Coefficient*	D_0	8.26×10^{-16} m^2/s	eq. 2.28
Drag Force Motor*,**	F_d	4.15 pN	eq. 2.18
Gravitational Force*	F_g	0.00077 pN	eq. 2.9
Root Mean Squared Velocity*	v_rms	0.0128 m/s	eq. 2.30
Relaxation Time* (=m/γ)	τ	1.52×10^{-11} s	eq. 2.12
Diffusive Coasting Distance*	L_c	1.94×10^{-13} m	eq. 2.11

Table 2.2: *The above data will be used as a representative model system for an organelle that is transported through a cell. Where available, follow the equation numbers for an explanation in the text. *Calculated values. **Note: in water (η = 0.001 Pas [3]) these forces are a factor 1000 smaller.*

opening and closing of the scallop. The only way to generate net displacement at low Reynolds numbers is by means of asymmetrical motion. For example, this type of motion occurs in a flexible oar on a molecular rowing boat. The oar follows a different paths during the power and recovery strokes thus creating net displacement. In nature, molecular swimmers are powered by the asymmetrical motion of cilia and flagella [65]*. The organelle in table 2.2 does neither have cilia nor flagella, therefore it needs a concentration gradient or an external force to displace through the cell. Molecular motors

---

*A swimmer in a pool filled with molasses that is only allowed to move with the speed of the arms of the clock who after a few weeks has managed to move a few meters, qualifies as a low Re swimmer [64].

that walk in directed fashion along a cytoskeletal track provide the organelle with just such a force.

An Organelle Moving In A Fluid

When an organelle moves through a fluid it encounters fluid friction via the viscosity (see section about the Reynolds number). This causes the organelle to disturb the fluid and set up a flow field around it. We can use streamlines to visualise this flow field. A streamline (ψ = constant) is a curve that is tangent to the instantaneous velocity field around the organelle [59]. If we assume that the organelle is a spherical and solid particle, we can describe the flow field using the following equation [60]:

$$\psi = \frac{1}{4} v r^2 sin^2\theta \left[\left(\frac{a}{r} \right)^3 - 3 \left(\frac{a}{r} \right) \right] . \tag{2.13}$$

This formula yields the following velocity components around the organelle [60]:

$$v_{\mathrm{r}} = -\frac{1}{r^2 sin\theta} \frac{\partial \psi}{\partial r} = -\frac{1}{2} v cos\theta \left(\frac{a}{r} \right)^2 \left(\frac{a}{r} - 3\frac{r}{a} \right) \tag{2.14}$$

and

$$v_\theta = \frac{1}{r sin\theta} \frac{\partial \psi}{\partial r} = -\frac{1}{4} v sin\theta \left(\frac{a}{r} \right) \left[\left(\frac{a}{r} \right)^2 + 3 \right] . \tag{2.15}$$

The streamlines around the organelle that is moving through a fluid are shown schematically in Fig.2.2A. The flow of fluid around an immobile organelle is shown in Fig.2.2B.

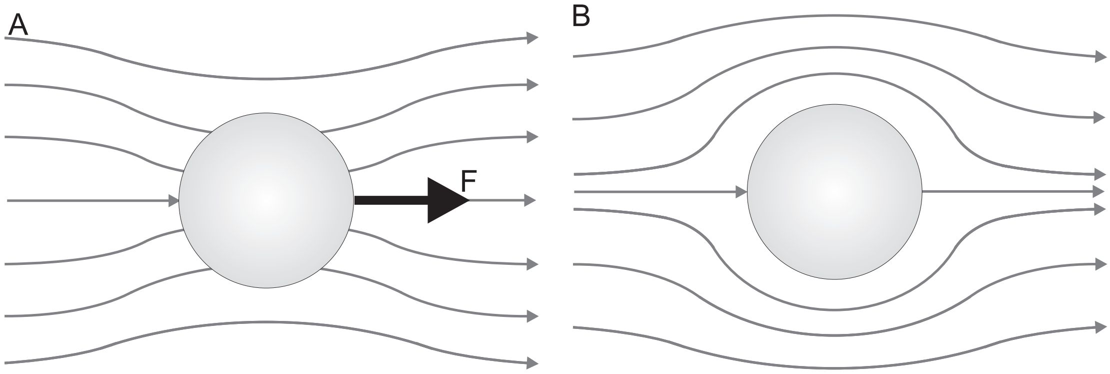

Figure 2.2: *Streamlines around an organelle, which we assume to be a spherical solid object, in a fluid. Figure A shows the streamlines around a moving organelle (active particle). In Figure B, the frame of reference is changed. The fluid is now moving around an immobile organelle [60].*

In the following discussion it is assumed that the organelle is an active particle moving through the fluid driven by an external or internal force. The magnitude of the friction force can be determined by integrating the normal, $\mathbf{\Pi}_{\mathrm{rr}}$, and tangential, $\mathbf{\Pi}_{\mathrm{r}\theta}$, stress terms of the molecular stress tensor, $\mathbf{\Pi}$ (eq.2.3 represented in spherical coordinates), around the surface of the sphere, which yields (see [57,59,60] for details):

$$\boldsymbol{F}_{\mathrm{d}}^{\mathrm{n}} = -2\pi\eta a\boldsymbol{V} \tag{2.16}$$

and

$$\boldsymbol{F}_{\mathrm{d}}^{\mathrm{t}} = -4\pi\eta a\boldsymbol{V}. \tag{2.17}$$

The friction force from the normal stress is called form drag, $\boldsymbol{F}_{\mathrm{d}}^{\mathrm{n}}$, whereas the tangential force gives rise to a viscous (or skin) drag force, $\boldsymbol{F}_{\mathrm{d}}^{\mathrm{t}}$. Note that the ratio of viscous to form drag is 2:1. It is believed that it is this asymmetry that allows the low Re swimmer, introduced in the previous section, to move via asymmetrical motion [64]. The adding of both forces yields *Stokes' law*, which is the total drag force, $\boldsymbol{F}_{\mathrm{d}}$, around the organelle:

$$\boldsymbol{F}_{\mathrm{d}} = \boldsymbol{F}_{\mathrm{d}}^{\mathrm{n}} + \boldsymbol{F}_{\mathrm{d}}^{\mathrm{t}} = -6\pi\eta a\boldsymbol{V}. \tag{2.18}$$

This is a linear relation between the force and the velocity as expected from the linearity of Stokes' equation (eq.2.10). Note the minus sign as this force works against the motion of the organelle. This equation allows us to define the fluid dependent drag coefficient, γ, and self-mobility, μ_0, of the organelle to be [3]:

$$\gamma = \frac{1}{\mu_0} = 6\pi\eta a. \tag{2.19}$$

For the organelle in table 2.2, the drag force is 4.15 pN, which is large as compared to the motor stall force of 5-7 pN. This shows that one molecular motor generates enough force to move an organelle, but that multiple motors working in concert might be favourable.

Many Organelles Moving In A Fluid - Hydrodynamic Interactions

Inside the eukaryotic cell there are many organelles moving through the cytosol. Each of these organelles experiences a negative drag force and, via momentum transfer*, sets up a flow field (Fig.2.2A). Even though these flow fields fall off to zero at infinite distance away from the organelles, they will influence the flow field around nearby organelles and thereby change their trajectories.

---

*See the parallel plates experiment (Fig. 2.1).

An organelle will thus experience a fluid friction force generated by its own motion (see eq.2.18), but also from the surrounding flow field that is set up by other organelles in the system. This flow field, $\acute{\boldsymbol{V}}\left(\boldsymbol{r}\right)$, generated by all organelles in the system, will now be determined (see [59, 60, 63, 66, 67] for more detailed or alternative derivations). Assuming that the flow field changes gradually with position and using the appropriate boundary conditions, the hydrodynamic drag force on an organelle becomes:

$$\boldsymbol{F}^{\mathrm{h}} = -6\pi\eta a\left(\boldsymbol{V} - \acute{\boldsymbol{V}}\left(\boldsymbol{r}\right)\right). \tag{2.20}$$

The problem can be simplified by making the following assumptions: (1) At all organelles we have no-slip boundary conditions, (2) the flow field varies gradually with position and (3) the distances in the system are large with respect to the organelle radii. (4) Only active organelles, i.e. those with a net force acting upon them, will influence the flow field and additionally, (5) we assume that the forces on all organelles are point-like forces acting on a Newtonian liquid. Under the quasi-static approximation, where the velocity and pressure fields satisfy the balance equations below, we can solve the flow field.

$$\nabla \cdot \acute{\boldsymbol{V}} = 0 \tag{2.21}$$

$$\eta\nabla^2\acute{\boldsymbol{V}} - \nabla p = \sum_{\mathrm{j}} \delta\left(\boldsymbol{r} - \boldsymbol{R}_{\mathrm{j}}\right)\boldsymbol{F}_{\mathrm{j}} \tag{2.22}$$

In this equation, $\boldsymbol{R}_{\mathrm{j}}$, is the position of organelle, j, and the summation runs over all organelles excluding organelle, i. The force acting on an organelle, j, is given by $\boldsymbol{F}_{\mathrm{j}}$ and it originates from the centre of the organelle. Moreover, $\delta\left(\boldsymbol{r} - \boldsymbol{R}_{\mathrm{j}}\right)$, is Dirac's delta function. The solution of the flow field is given by:

$$\acute{\boldsymbol{V}} = \sum_{\mathrm{j}} \boldsymbol{\mu}\left(\boldsymbol{r} - \boldsymbol{R}_{\mathrm{j}}\right) \cdot \boldsymbol{F}_{\mathrm{j}}. \tag{2.23}$$

The tensor, $\boldsymbol{\mu}\left(\boldsymbol{r}\right)$, is the *Green-function* of the system and it gives the inter-organelle mobilities, $\boldsymbol{\mu}_{\mathrm{ij}}$. As was the case for the self-mobility of a single organelle, $\boldsymbol{\mu}_{\mathrm{ii}} = \mu_0\hat{\boldsymbol{I}}$, where $\hat{\boldsymbol{I}}$ is an identity matrix, the inter-organelle mobilities are linear functions of the force and velocity. A simple solution of the mobility tensor is given by the *Oseen tensor*[*] that is defined as:

$$\boldsymbol{\mu}_{\mathrm{ij}} = \begin{cases} \mu_0\hat{\boldsymbol{I}} & \mathrm{i} = \mathrm{j} \\ \frac{1}{8\pi\eta r_{\mathrm{ij}}}\left[\hat{\boldsymbol{I}} + \hat{\boldsymbol{r}}_{\mathrm{ij}} \otimes \hat{\boldsymbol{r}}_{\mathrm{ij}}\right] & \mathrm{i} \neq \mathrm{j}. \end{cases} \tag{2.24}$$

---

[*] Some authors call this the Oseen-Burgers tensor [59].

The inter-organelle distance is described by vector $\boldsymbol{r}_{ij} = \boldsymbol{r}_i - \boldsymbol{r}_j$, r_{ij} is its magnitude, $\hat{\boldsymbol{r}}_{ij} = \boldsymbol{r}_{ij}/r_{ij}$ a unit vector and $\hat{\boldsymbol{r}}_{\mathrm{ij}} \otimes \hat{\boldsymbol{r}}_{\mathrm{ij}}$ a dyadic product. By multiplying the numerator and denominator by $6a$, we can express the Oseen tensor as a function of μ_0:

$$\boldsymbol{\mu}_{\mathrm{ij}} = \begin{cases} \mu_0 \hat{\boldsymbol{I}} & \mathrm{i} = \mathrm{j} \\ \frac{3}{4}\mu_0 \frac{a}{r_{\mathrm{ij}}}[\hat{\boldsymbol{I}} + \hat{\boldsymbol{r}}_{\mathrm{ij}} \otimes \hat{\boldsymbol{r}}_{\mathrm{ij}}] & \mathrm{i} \neq \mathrm{j}. \end{cases} \tag{2.25}$$

Note that the hydrodynamic interactions are long-range interactions as they decay as r^{-1}. It is known that the Oseen tensor becomes inaccurate at short distances because it does not correctly represent the flow field at short length scales. Moreover, the forces acting on the active particles are treated as point forces at $r_{\mathrm{ij}} = 0$. A more accurate mobility tensor that includes the organelle size as well as short-range hydrodynamic interactions is given by Stokes [59,68]:

$$\boldsymbol{\mu}_{\mathrm{ij}} = \begin{cases} \mu_0 \hat{\boldsymbol{I}} & \mathrm{i} = \mathrm{j} \\ \frac{3}{4}\mu_0 \frac{a}{r_{\mathrm{ij}}} \left(\hat{\boldsymbol{I}} + \hat{\boldsymbol{r}}_{\mathrm{ij}} \otimes \hat{\boldsymbol{r}}_{\mathrm{ij}}\right) + \frac{1}{4}\mu_0 \left(\frac{a}{r_{\mathrm{ij}}}\right)^3 \left(\hat{\boldsymbol{I}} - 3\hat{\boldsymbol{r}}_{\mathrm{ij}} \otimes \hat{\boldsymbol{r}}_{\mathrm{ij}}\right) & \mathrm{i} \neq \mathrm{j}. \end{cases} \tag{2.26}$$

The term proportional to a/r_{ij} is called the Stokeslet and it describes the viscous response of the fluid to the no-slip condition at the organelle surface. The term proportional to $(a/r_{\mathrm{ij}})^3$ is called the stresslet. This term contributes to irrotational flow, which is unrelated to the viscous force on the organelle and is caused by the finite size of the organelle*. The latter term influences the flow field on short distances as it falls off rapidly with r_{ij}^{-3}, where the Stokeslet's term is long ranged as it decays with r_{ij}^{-1}. At long distances, $r_{\mathrm{ij}}^{-3} \gg a$, Stokes' solution simplifies back to the Oseen tensor [59]†. Alternative tensors exist that correct for the shape and size of the organelles.

An Organelle's Sensitivity To Hydrodynamic Interactions

To determine the sensitivity of an organelle to the flow field in a fluid, *the Stokes number*, S_{k}, is used. This dimensionless number is defined as the ratio between the relaxation time, τ (eq.2.12), of the suspended organelle and the characteristic time in which flow, governed by another organelle, changes. At a large Stokes number the moving organelle is not affected by the surrounding flow field. However, for $S_{\mathrm{k}} \ll 1$, the organelle follows the streamlines closely [59]. The Stokes number is defined below.

---

[*] Note that the Stokeslet and stresslet terms also appear in equations 2.14 and 2.15. These equations describe the velocity around an organelle.

[†] The hydrodynamic interactions tensor of Stokes (eq.2.26) reduces to, $\mu_{\mathrm{ij}} = \mu_0 \hat{\mathbf{I}}$, at the surface of a spherical organelle ($r_{\mathrm{ij}} = a$) [59].

$$S_{\mathrm{k}} = \frac{U\tau}{L} \tag{2.27}$$

Next, it is determined how the flow field, which has been set up by an organelle of size, L, that is moving with velocity, U, affects the motion of the model organelle. If both organelles are assumed to have equal size and velocity, such that $L = a$ and $U = V$, we find: $S_{\mathrm{k}} = 4.85 \times 10^{-11}$. Thus, the organelle in table 2.2 is very sensitive to the flow field coming from the other organelles on which an external force is acting.

Diffusion

As mentioned in chapter 1, the suspended organelles are small (50-2000 nm, see table 1.1), but they are still large with respect to the molecules of the surrounding medium. This means that when the molecules of the cytosol collide with the organelles, their change in momentum transmits an impulsive force on the organelle. These collision forces are called thermal forces as their magnitude depends on the temperature of the fluid. The random motion of the molecules is called diffusion, whereas the resulting diffusive motion of a suspended organelle is referred to as *Brownian Motion* [3]. The magnitude of the diffusion of the molecules in a fluid is given by the (self-)diffusion coefficient, D_0, which is the ratio between the thermal energy of the fluid molecules and the friction factor of the fluid [3]:

$$D_0 = \frac{k_{\mathrm{b}}T}{6\pi\eta a} = \frac{k_{\mathrm{b}}T}{\gamma} = k_{\mathrm{b}}T\mu_0. \tag{2.28}$$

This equation is called the *Stokes-Einstein equation* or *Einstein relation*. The equation states that the value of the diffusion coefficient can be calculated from the response of the system under external force [63]. The diffusion coefficient will increase with rising temperature i.e. larger thermal forces, and is inversely proportional with the viscosity. The latter is the fluid's internal resistance against motion. The organelle in table 2.2 (in cytosol at 37 °C) has a diffusion coefficient of D_0 = 8.26 $\times 10^{-16}$ m^2/s. The mean and variance of the random thermal forces are given by [3]:

$$\begin{aligned} \langle F_{\mathrm{th}} \rangle &= 0 \\ \sigma^2 = \langle F_{\mathrm{th}}^2 \rangle &= \gamma^2 \langle v^2 \rangle. \end{aligned} \tag{2.29}$$

Moreover, the variance depends upon the average velocity of the cytosol molecules that is given by $\langle v \rangle$. The latter can be calculated from the root-mean-square-velocity, v_{rms} [3], using the following equation [3]:

$$v_{\mathrm{rms}} = \sqrt{\langle v^2 \rangle} = \sqrt{\frac{3k_{\mathrm{b}}T}{m}}. \tag{2.30}$$

Using data from table 2.2, this yields $v_{\rm rms}$ = 1.28×10^{-2} m/s and $\langle v^2 \rangle$ = 1.64×10^{-4} m^2/s^2 for the reference organelle. Additionally, the variance of the thermal forces and standard deviation are σ^2 = 4.39×10^{-15} N^2 and σ = 6.63 ×10^{-8} N respectively.

Diffusion Versus Directed Transport

To determine if the external forces working on the model organelle are large enough to overcome diffusion, the shortest time, $t_{\rm d}$, needed to diffuse a given distance, L, is calculated (see results in table 2.3). For one-dimensional diffusion, e.g. organelles bound to the bio-filament in absence of ATP, it is given by [3]:

$$t_{\rm d} = \frac{L^2}{2D_0}. \tag{2.31}$$

ATP is present in abundance in the eukaryotic cell, therefore the bound motor(s) will exert an external force upon the organelle. The resulting motion is a combination of diffusion and directed motion. This combined motion is called biased diffusion. The biased diffusive time, $t_{\rm bd}$, of this movement can be calculated via [3]:

$$t_{\rm bd} = 2\left(\frac{L^2}{2D_0}\right)\left(\frac{k_{\rm b}T}{F_0 L}\right)^2 \left[exp\left(-\frac{F_0 L}{k_{\rm b}T}\right) - 1 + \frac{F_0 L}{k_{\rm b}T}\right]. \tag{2.32}$$

For long time scales (with respect to τ) and distances, this equation approaches a situation where diffusion is absent i.e. the motion becomes ballistic. Table 2.3 shows that in water this occurs at distances from 10^{-3}, whereas is cytosol this happens at 10^{-6} m. The (ballistic) motor time, $t_{\rm b}$, is given by:

$$t_{\rm b} = \frac{L}{V_0}. \tag{2.33}$$

In the above equation, V_0, is the motor velocity. In table 2.3, the diffusive, biased diffusive and ballistic motor times are compared for different length scales. The fluid medium is cytosol and the motor has a velocity V_0 = 800 nm/s (see table 2.2).

The data shows that for length scales shorter than 10^{-8} m, diffusion is the dominant process. At larger distances the speed of the motor is faster than diffusion. Moreover, the biased diffusive motion is sensitive to diffusion up to distances of 10^{-7} m after which it equals the (ballistic) motor velocity. For an organelle to cover large distances, e.g. to cover the full distance of a cell of 1μm, molecular motors are essential for transport as the table shows that motor transport is 10^5 times faster than diffusion.

The Péclet number [57, 59, 65], Pe, is another method to determine if diffusion or directed motion is the dominant process. This dimensionless number is defined as the ratio between the rate of convection versus the rate of diffusion and is given by:

L	t_{b}	t_{d}		t_{bd}		Pe	
m	s	Water s	Cell s	Water s	Cell s	Water	Cell
	1.25	5.51	6.05			8.81	9.69
10^{-9}	$\times 10^{-3}$	$\times 10^{-7}$	$\times 10^{-4}$	5.50×10^{-7}	4.49×10^{-4}	$\times 10^{-4}$	$\times 10^{-1}$
10^{-8}	$\times 10^{-2}$	$\times 10^{-5}$	$\times 10^{-2}$	5.49×10^{-5}	1.12×10^{-2}	$\times 10^{-3}$	$\times 10^{0}$
10^{-7}	$\times 10^{-1}$	$\times 10^{-3}$	$\times 10^{0}$	5.35×10^{-3}	1.24×10^{-1}	$\times 10^{-2}$	$\times 10^{1}$
10^{-6}	$\times 10^{0}$	$\times 10^{-1}$	$\times 10^{2}$	4.19×10^{-1}	1.25×10^{0}	$\times 10^{-1}$	$\times 10^{2}$
10^{-5}	$\times 10^{1}$	$\times 10^{1}$	$\times 10^{4}$	1.11×10^{1}	1.25×10^{1}	$\times 10^{0}$	$\times 10^{3}$
10^{-4}	$\times 10^{2}$	$\times 10^{3}$	$\times 10^{6}$	1.24×10^{2}	1.25×10^{2}	$\times 10^{1}$	$\times 10^{4}$
10^{-3}	$\times 10^{3}$	$\times 10^{5}$	$\times 10^{8}$	1.25×10^{3}	1.25×10^{3}	$\times 10^{2}$	$\times 10^{5}$

Table 2.3: *Typical transport times over different distances, L, for the reference organelle (See table 2.1) moving at 800 nm/s in cytosol and water. See table 2.1 for the cytosol data. For water:* η_{water} *= 0.001 Pas,* F_0 *= 3.8* $\times 10^{-15}$ *N,* γ_{water} *= 4.71*$\times 10^{-9}$ *Ns/m and* $D_{0,water}$ *= 9.08*$\times 10^{-13}$ *m*^{2}*/s. The ballistic time,* t_{b}*, is the time it will take a molecular motor to walk a given distance (eq.2.33). The time needed to travel this distance via diffusion is,* t_{d} *(eq.2.31), and,* t_{bd} *(eq.2.32), is the time for biased diffusion [3]. Finally, the Péclet number,* Pe *(eq.2.34), which is the dimensionless ratio between the rate of transport by convection and diffusion [57, 65] is shown.*

$$Pe = \frac{\text{Rate of convection}}{\text{Rate of diffusion}} = \frac{V_0 L}{D_0} = \frac{F_0 L}{k_{\mathrm{b}} T}. \tag{2.34}$$

Inserting for the motor velocity, $V_0 = \mu_0 F_0$, together with eq.2.28 yields the last term on the right hand side. The latter shows that the Pe number can also be interpreted as a typical length times the ratio of the driving force on the organelle and the thermal energy of the fluid molecules. This makes the Pe number independent of the fluid medium. For small values of Pe, diffusive transport dominates. For Pe values of ≈10 and larger, directed transport is the dominant transport mechanism.

The Pe numbers for different length scales are presented in table 2.3. In cytosol, directed transport dominates over diffusion from length scales of 10^{-8} m. This confirms the results already found using eq.2.32.

Note that comparison with the same organelle moving with equal velocity in water (η_{water} = 0.001 Pas, γ_{water} = 4.71$\times 10^{-9}$ Ns/m and, $D_{0,\mathrm{water}}$ = 9.08$\times 10^{-13}$ m^2/s) yields different results. As the viscosity of water is a factor 1000 smaller than for cytosol, the required motor force to obtain the same velocity is a factor 1000 smaller. This results in Pe numbers a factor 1000 smaller at the same length scales. Moreover, since the diffusion coefficient is a factor 1000 larger in water, the diffusive time also becomes a factor

1000 smaller. Additionally, the larger D_0 makes diffusion influence the biased diffusion up to distances of 10^{-3} m (eq.2.32), a factor 1000 larger than in cytosol.

In experiments, the same motor shows a similar velocity (or smaller) *in vitro* and *in vivo* (see e.g. table 13.1 in [3]). Whereas in water the motor force easily overcomes the friction force, in the cell it will only just overcome this force (see example below eq.2.19). Again this shows that an additional transport mechanism, such as enhanced transport via hydrodynamic interactions, is essential inside the cell.

Table 2.4 shows how the transport parameters, that were introduced in the previous sections, compare with experimental data. These results were obtained *in vivo* using Quantum Dot experiments. Values denoted with an * are calculated values. The viscosity measured in the different cells is a factor 1000 larger than in water. In addition, the Pe number shows that convective transport dominates over diffusion.

Cell type	**Motor**	a	V	T	η	γ	D_0	F_d	Pe
		m	m/s	°C	Pas	kg/s	m^2/s	N	-
		$\times10^{-9}$	$\times10^{-6}$			$\times10^{-6}$	$\times10^{-16}$	$\times10^{-12}$	
HeLa [26]	Myosin-V	30	0.71	20	0.3975*	0.22*	180	0.16*	2*
HeLa [24]	Kinesin-1	15	0.57	20	1.7242*	0.49*	83	0.28*	2*
PC12 [23]	Kinesin-?	230	1.25	37	1.1	4.77*	8.98*	5.96*	640*
PC12 [23]	Dynein	230	1.2	37	1.1	4.77*	8.98*	5.72*	614*
NT2 [25]	-	300	-	-	1.8	10.18*	4.21*	-	-
NT2 [56]	-	-	2.3	-	3.6	2.91*	14.70*	6.7	134*

Table 2.4: *Molecular motor properties measured in vivo in different cells. * Calculated values.*

Langevin Equation

In the previous sections, *the Stokes equation* was introduced that was used to analyse the transport properties of the fluid. The Stokes equation is the equation of motion for fluids in absence of inertia and with constant density and viscosity. From this equation followed the hydrodynamic interaction tensor describing the flow fields around many (active) suspended organelles. As these equations only balance the forces acting on the fluid, we now need an equation describing the motion of the organelle. This equation of motion for a suspension of organelles (or any other object in a fluid) is called *the Langevin equation* [3,57,63,69]. I will discuss this equation by following an organelle i:

$$\begin{aligned} m\frac{d^2\boldsymbol{r}_\mathrm{i}}{dt^2} &= \boldsymbol{F}_\mathrm{friction} + \boldsymbol{F}_\mathrm{conservative} + \boldsymbol{F}_\mathrm{thermal} \\ &= -\gamma\frac{d\boldsymbol{r}_\mathrm{i}}{dt} + \boldsymbol{F}_\mathrm{i} + \gamma\boldsymbol{g}_\mathrm{i}(t). \end{aligned} \tag{2.35}$$

This equation balances all the forces acting on the organelle, which include the fluid friction force, $\boldsymbol{F}_\mathrm{friction}$, conservative forces, $\boldsymbol{F}_\mathrm{conservative}$ (e.g. external, coulomb, and elastic forces) and thermal forces, $\boldsymbol{F}_\mathrm{thermal}$. Additionally, $\boldsymbol{g}_\mathrm{i}(t)$, is a random velocity resulting from thermal forces. The latter is defined as a random variable from a *Gaussian distribution* with zero mean and its variance is proportional to the diffusion coefficient via $\boldsymbol{D}_\mathrm{ii} = D_0\hat{\boldsymbol{I}}$:

$$\begin{aligned} \langle\boldsymbol{g}_\mathrm{i}(t)\rangle &= \boldsymbol{0} \\ \langle\boldsymbol{g}_\mathrm{i}(t)\boldsymbol{g}_\mathrm{i}(t^{'})\rangle &= 2\boldsymbol{D}_\mathrm{ii}\delta(t-t^{'}). \end{aligned} \tag{2.36}$$

The magnitude of the diffusion coefficient is given by the Stokes-Einstein equation (eq.2.28). The Langevin equation is a stochastic differential equation as it contains a random term. For solving it, times larger than the relaxation time are assumed (see eq.2.12). As previously explained, the organelle moves at low Reynolds numbers, i.e. there is no inertia and velocities are instantaneous. Taking the above into account yields the following Langevin equation:

$$\begin{aligned} \frac{d\boldsymbol{r}_\mathrm{i}}{dt} &= \frac{\boldsymbol{F}_\mathrm{i}}{\gamma} + \boldsymbol{g}_\mathrm{i}(t) \\ &= \mu_0\boldsymbol{F}_\mathrm{i} + \boldsymbol{g}_\mathrm{i}(t). \end{aligned} \tag{2.37}$$

The equation describes the average speed of an organelle superimposed on the diffusive motion. Subsequently, the time evolution of the probability distribution, p_i, of the organelle's position can be described using the *Fokker-Planck equation* [3, 63]. This equation is equivalent to the Langevin equation as it describes the same dynamics. It is given by [69]:

$$\frac{\partial p}{\partial t} = D_0\sum_\mathrm{i}\nabla^2_{\boldsymbol{r}_\mathrm{i}}p - \frac{D_0}{k_\mathrm{b}T}\sum_\mathrm{i}\nabla_{\boldsymbol{r}_\mathrm{i}}\cdot\big(\boldsymbol{F}_\mathrm{j}p\big) \tag{2.38}$$

In this equation, $\nabla_{\boldsymbol{r}_\mathrm{i}}$, is the derivative with respect to the organelle position. The solution of the above equation coincides with the *Boltzmann distribution* when it approaches steady-state at $t\to\infty$ [63]:

$$p\left(x_\mathrm{i}\right) \propto \exp\left(-\frac{U_\mathrm{i}}{k_\mathrm{b}T}\right) \tag{2.39}$$

The potential energy of the conservative force is given by U_{i}. The Fokker-Planck equation is now extended for interacting particles as is the case for hydrodynamic interactions between the organelles. The resulting N-body Smoluchowski equation is given by [69,70]:

$$\frac{\partial p}{\partial t} = \sum_{\mathrm{i}} \sum_{\mathrm{j}} \nabla_{\boldsymbol{r}_{\mathrm{i}}} \cdot \boldsymbol{D}_{\mathrm{ij}} \cdot \nabla_{\boldsymbol{r}_{\mathrm{j}}} p - \sum_{\mathrm{i}} \sum_{\mathrm{j}} \nabla_{\boldsymbol{r}_{\mathrm{i}}} \cdot \frac{\boldsymbol{D}_{\mathrm{ij}}}{k_{\mathrm{b}} T} \cdot \boldsymbol{F}_{\mathrm{j}} p \tag{2.40}$$

Again, the steady-state solution approximates the Boltzmann distribution. However, the diffusion coefficient, $\boldsymbol{D}_{\mathrm{ij}}$, is no longer a constant but a 3-dimensional position dependent tensor given by [71]:

$$\boldsymbol{D}_{\mathrm{ij}} = D_0 \delta_{\mathrm{ij}} \hat{\boldsymbol{I}} + (1 - \delta_{\mathrm{ij}}) k_{\mathrm{b}} T \boldsymbol{\mu}_{\mathrm{ij}}. \tag{2.41}$$

The corresponding Langevin Equation is given by [63,69,72]:

$$\frac{d\boldsymbol{r}_{\mathrm{i}}}{dt} = \boldsymbol{\mu}_{\mathrm{ii}} \cdot \boldsymbol{F}_{\mathrm{i}} + \sum_{\mathrm{j,j \neq i}} \boldsymbol{\mu}_{\mathrm{ij}} \cdot \boldsymbol{F}_{\mathrm{j}} + \boldsymbol{g}_{\mathrm{i}}(t) + \nabla_{\boldsymbol{r}_{\mathrm{j}}} \cdot \boldsymbol{D}_{\mathrm{ij}}. \tag{2.42}$$

There exist different mobility tensors that can be chosen for $\boldsymbol{\mu}_{\mathrm{ij}}$. Both the Oseen tensor (eq.2.25) and Rotne-Prager tensor (eq.4.10) have the property that $\nabla_{\boldsymbol{r}_{\mathrm{j}}} \cdot \boldsymbol{D}_{\mathrm{ij}} = \boldsymbol{0}$ [69,72]. This yields:

$$\frac{d\boldsymbol{r}_{\mathrm{i}}}{dt} = \boldsymbol{\mu}_{\mathrm{ii}} \cdot \boldsymbol{F}_{\mathrm{i}} + \sum_{\mathrm{j,j \neq i}} \boldsymbol{\mu}_{\mathrm{ij}} \cdot \boldsymbol{F}_{\mathrm{j}} + \boldsymbol{g}_{\mathrm{i}}(t). \tag{2.43}$$

It is this equation that will be solved using simulations in subsequent chapters. The mean and variance of the random velocity are now given by [63]:

$$\begin{aligned} \langle \boldsymbol{g}_{\mathrm{i}}(t) \rangle &= \boldsymbol{0} \\ \langle \boldsymbol{g}_{\mathrm{i}}(t) \boldsymbol{g}_{\mathrm{j}}(t^{'}) \rangle &= 2\boldsymbol{D}_{\mathrm{ij}} \delta(t - t^{'}). \end{aligned} \tag{2.44}$$

Note that the random velocities are no longer independent of each other as $\boldsymbol{D}_{\mathrm{ij}}$ depends upon the position of the organelles with respect to each other. Consequently, these are correlated random velocities.

Summary

In this chapter I show that the friction forces acting on the reference organelle (see table 2.2) are much larger than the forces of inertia ($Re \ll 1$). The magnitude of these friction forces are enhanced by the high viscosity of the cytosol (η = 1 Pas, see table 2.4), which yields a drag coefficient, γ, a factor 1000 larger than in water. At low Reynolds numbers, in the absence of external forces and gradients, the organelle will show no net displacement. Therefore it needs an external power source. Molecular motors can provide just such a force. An organelle bound to the bio-filament via molecular motor(s) is called an active particle. Any active particle, moving through a fluid, sets up a flow field via momentum transfer into the fluid medium. This flow field will influence the motion of other suspended organelles that are sensitive to this flow field as is shown by the small Stokes number ($S_\mathrm{k} \ll 1$). Moreover, the organelle is small enough to be subject to Brownian motion. Whereas diffusion is the dominant process at very short time and length scales, the Péclet number ($Pe \geq 10$) shows that in cytosol at distances from 10^{-6} m (the size of the organelle) active transport is the dominant transport mechanism. Again this highlights the importance of molecular motors in intracellular transport.

As for organelles in the cell inertia and gravitational forces can be ignored and the density and viscosity are assumed constant throughout the fluid, the Navier-Stokes equation reduces to the Stokes equation. This equation of motion for fluids was used to derive an expression for the hydrodynamic interaction tensor that describes the flow field set up by the actively moving organelles in this fluid. Finally, the hydrodynamic interactions were introduced into the equation of motion for a suspended organelle yielding the Langevin equation that will be used in the simulations of chapters 4 and 6.

Chapter 3

Theoretical Models For Molecular Motor Transport

Introduction

Theoretically, active transport by molecular motors has been studied extensively at different levels. Some authors take a bottom-up approach trying to describe how the molecular motors work internally i.e. elucidating the coupling between conformational changes of the motor to the hydrolysis of ATP [73]. Others used these results to set up *discrete stochastic models* [74] where the configurational changes of a stepping motor are modelled as a series of energy states. Moreover, combination of experimental work with bottom-up research yielded concepts such as the *duty cycle* [75] and *duty ratio* [3,76] that can predict whether a single motor is processive or needs to work in an assembly of motors. In addition, different groups tried to understand the stepping of molecular motors along the cytoskeletal filaments by means of an *inchworm* mechanism [77], *Hand-over-hand* mechanism [78,79] or a combination of both [80]. Finally, the motion of the unbound head of an attached motor was studied. Is the next binding site found by a (stiff) lever mechanism [81] or a diffusive search [80,82–84]?

In this chapter I give a review of the development of theories describing directed molecular motor motion (and their cargoes). These theories use simple physical transport processes that do not include the molecular details or the chemistry involved. These models inspired the computer models presented in this thesis (see chapters 4 and 6).

In order to develop a model, first its desired features should be clear. As in this thesis we are interested in the collective transport of many organelles by molecular motors, a theoretical description should include the following features: (1) Directed motion, (2) thermal fluctuations, (3) description of the dynamics of bound and suspended motor-organelle complexes, and (4) hydrodynamic interactions. As we deal with very low

Reynolds numbers (see chapter 2), asymmetry is the key element to move in a directed way in such an environment.

Feynman-Smoluchowski ratchet

Since molecular motors and their cargoes are small enough to be subject to thermal forces, the first attempted model used only these thermal fluctuations as power source to rectify a net motion. The *Feynman-Smoluchowski ratchet*, which was first studied by Smoluchowski [85, 86] and later discussed by Feynman during his lectures on thermodynamics [87], is based upon this principle (see Fig.3.1A).

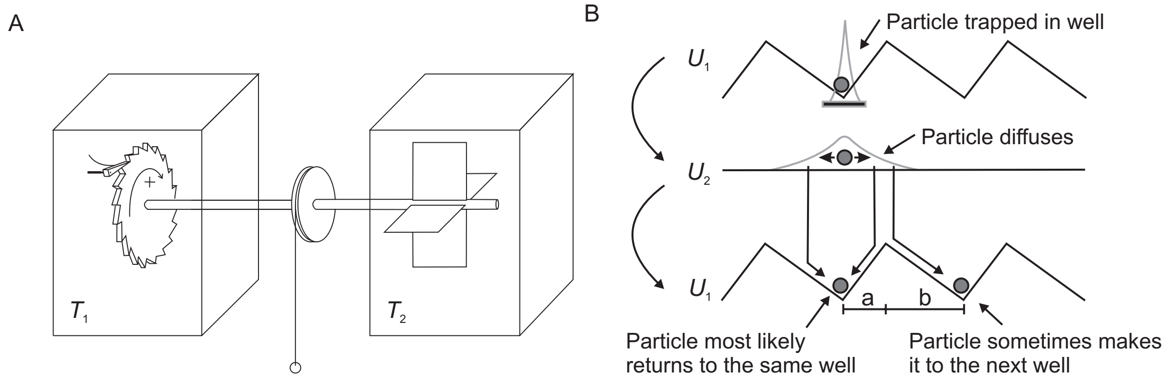

Figure 3.1: *A) Feynman-Smoluchowski ratchet and pawl device - Two heat baths, 1 and 2, are connected by an axis. A weight is suspended from the axis. In one heat bath vanes are mounted on the axis, on the other a ratchet wheel. Asymmetry is introduced by restricting the ratchet wheels' motion to one direction by introduction of a pawl. As the system is built at molecular scale it will be subject to thermal collisions. The molecular bombardments on the vanes makes the axis rotate in one direction only. This results in lifting the weight and thus violating the second law of thermodynamics. To make the system work it is essential that both reservoirs are at different temperatures, thus breaking detailed balance. Reproduced with kind permission from [88]. B) Brownian ratchet mechanism - In the asymmetric periodic potential* U_1 *a particle is diffusing inside a potential well. When the potential is switched off* (U_2) *the particle can diffuse freely. When it diffuses far enough before the potential is switched on again, it can get trapped in the next potential well. The combination of thermal fluctuations, and switching between potential states rectifies the stochastic thermal motion.*

Feynman posed the question whether it is possible to use the thermal fluctuations of molecules to generate directed motion i.e. is it possible to do mechanical work without having to spend energy to obtain it? The experiment consists of two isolated heat baths that are not in contact. The baths are connected by an axis that in one bath is mounted with vanes and in the other with a ratchet wheel. Additionally, a weight is suspended at the centre of the axis between the two heat baths. The whole system is at microscopic scale, thus the system is subject to and will be affected by collisions from the surrounding gas molecules. The vanes are hit at random from different directions causing the axis to rotate freely with equal probability in clockwise and counter-clockwise direction. Next, symmetry is broken by fixing the rotational direction of the ratchet wheel by addition of a pawl. As a consequence, the unidirectional rotational movement of the axis is capable of lifting the suspended weight. This suggests that the system works as a perpetuum mobile, extracting energy out of 'nothing' i.e. violating the second law of thermodynamics*. However, the system does not work since there are also gas molecules in the other heat bath. These molecules will collide with the pawl device and thereby release the ratchet wheel. Feynman showed that as long as both baths are at equal temperature, the probability for the vanes to rotate by molecular collisions is equal to the probability for the pawl to be lifted. Therefore, the system will only work when the baths are at different temperatures i.e. when detailed balance is broken. Thus, energy from an external source is needed to keep the baths at different temperatures.

Brownian ratchet

As demonstrated by Smoluchowski and Feynman, thermal motion alone is not enough to drive a mechanical system. A physical model for rectifying directed motion via molecular motors thus needs an external power source. In a cell this power source is ATP. Without ATP†, molecular motors will diffuse due to thermal fluctuations along the bio-filament [89–91] or through the cell. On average no net displacement will take place. When the external force, generated by hydrolysing ATP, is present, the motors will start walking along the bio-filament (see chapter 2). A simple model to capture thermal fluctuations and directed motion is the *Brownian ratchet* [86,92–94]. In Fig.3.1B the simplest version, *the flashing ratchet* is shown. In this model, a motor-organelle complex, from now on called simply the organelle, is subject to two different potential states. One state is flat, in this state the organelle diffuses freely along its surface. The other potential state is a periodic asymmetric sawtooth. The asymmetric shape is essential, as to generate motion detailed balance needs to be broken. This is analogous to the temperature difference that is required for the Feynman-Smoluchowski ratchet to work. When this potential is activated, the organelle gets trapped in one of the potential wells where it moves by thermal fluctuations. Here it is assumed that the temperature is low enough to prevent barrier crossing due to fluctuations. None of the two potential states individually can generate motion along the bio-filament. However, periodically 'switching' between the two potentials does generate motion. If the sawtooth state is activated,

---

[*] One definition of the second law of thermodynamics states that a process whose only net result is to take heat from a reservoir and convert it to work is impossible [87].

[†] In absence of other external forces and/or gradients.

the motor is trapped in the closest potential well, corresponding to its current position. When the sawtooth potential is switched off, the motor will diffuse freely. Next, the organelle is given enough time to, on average, diffuse a distance larger than the shortest distance (a in Fig.3.1B) between well and barrier, but not enough time to cross the other barrier (b in Fig.3.1B)*. After reactivation of the sawtooth potential, the organelle will either remain in the same potential well or end up in the next. Repetition of this procedure rectifies net motion, and can even oppose an external force [94] such as the viscous friction force of the cytosol. The flashing ratchet model is sensitive to many parameters, including the shape of the potential, the barrier height, the temperature, the motor diffusion coefficient and the switching frequency between the different states.

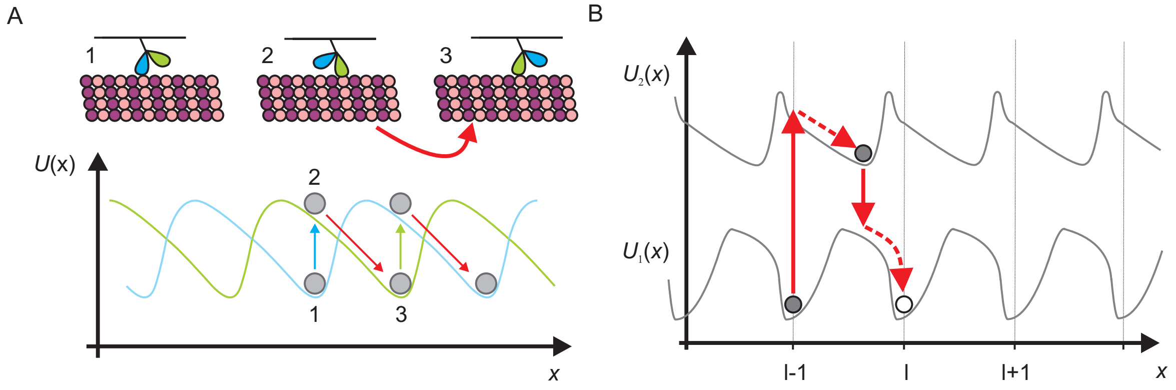

Figure 3.2: *A) A Brownian ratchet model for a two headed kinesin motor. Top - The hand-over-hand motion of a kinesin motor along a microtubule where the two heads are colour coded. Bottom - The two heads of the kinesin motor are modelled using two identical but shifted potentials. Shifting between the potentials is governed by the hydrolysis of ATP. Reproduced after [95] with kind permission from Springer Science and Business Media. B) Two different chemical states of a molecular motor bound to a bio-filament are shown as two different asymmetrical and periodic potentials, $U_1(x)$ and $U_2(x)$. The vertical arrow represents the input of chemical energy (hydrolysis of ATP), making the motor switch potential states. Stochastically switching between potentials yields a biased diffusive motion. The positions of the potential wells are indexed, l_i, along a potential with length x. Reproduced after [74] with kind permission from ANNUAL REVIEWS.*

---

*This time can be estimated using eq.2.31 introduced in chapter 2.

Ratchet Models Of Molecular Motors

Jülicher and co-workers [95] used the Brownian Ratchet to map the motion of the two heads of a processive kinesin motor on two asymmetrical energy landscapes, that are equal in size and shape, but shifted less then a period with respect to each other (see Fig.3.2A). The heads take turns in hydrolysing ATP and step along the microtubule while each head shifts from one energy landscape to another. A different approach is to view the bio-filament bound motor as diffusing on two or more spatially parallel, periodic and asymmetric coarse-grained potentials (see Fig.3.2B) [74]. Each potential corresponds to a different biochemical state of the motor. Driven by chemical energy, the motor switches stochastically from one potential to another and the resulting system evolves according to a set of coupled Fokker-Planck equations. This yields a biased diffusive motion. Finally, Jülicher et al [92] studied many motors moving simultaneously along a two-state Brownian ratchet, which could be used to describe systems where many motors work in concert such as in muscle contraction.

Brownian Ratchets Featuring Hydrodynamic Interactions

In 2003, Curtis and Grier [96] showed, using a toroidal optical trap, that small particles (800 nm polystyrene beads) can move around in a circular fashion. The motion is driven by angular momentum transfer coming from a tilted sinusoidal potential acting on the particles. By means of simulations Reichert and Stark [97] demonstrated that this transport could in a viscous fluid be enhanced by means of hydrodynamic interactions. In particular they noticed that pairs of particles moved faster than single particles. As a follow up, the same group confirmed this result in real experiments [98]. Additionally, they presented experiments with charged particles trapped in a static asymmetric potential. In this system a positive force is acting on the particles, additionally to the sawtooth potential, effectively yielding a tilted potential (Fig.3.3). If a particle 1 is trapped in the well and another particle 2 enters this well from above, the electrostatic repulsion will push particle 1 over the next barrier. Next, the hydrodynamic interactions between the particles makes particle 2 follow particle 1 over the barrier. This procedure is repeated and effectively the two particles move via a ’caterpillar like’ motion. Recently, Polson et al. [99] performed Brownian Dynamics simulations of a flashing ratchet potential where they report that the driven motion of a polymer in a ratchet potential is enhanced by hydrodynamic interactions. Moreover, Fornés [71] presented simulation results of two elastically coupled particles, representing the two heads of a molecular motor, in a flashing ratchet. He showed that not only do the hydrodynamic interactions enhance the transport but additionally can overcome an opposing load. Finally, the group of Stark repeated their experiments with the toroidal trap, but this time every particle was subject to an individual ratchet potential. Again hydrodynamic interactions enhanced the transport [100].

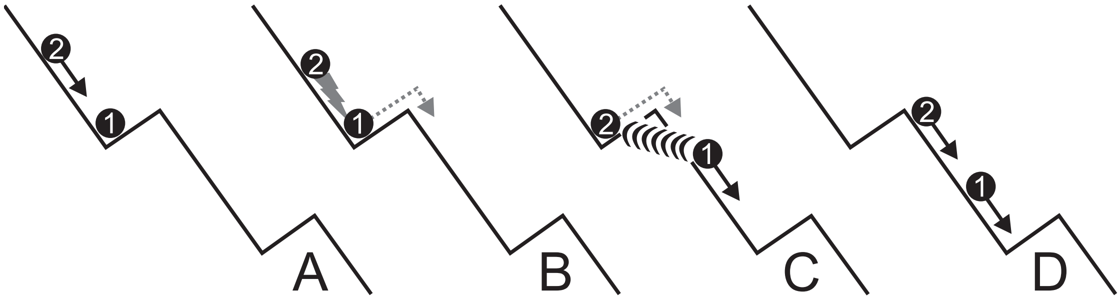

Figure 3.3: *Two charged particles in a tilted asymmetrical potential. (A) Particle 1 is trapped in a potential well, particle 2 enters this well. (B) Due to electrostatic interactions particle 2 pushes particle 1 over the barrier. (C) The hydrodynamic interactions between the particles cause particle 2 to follow over the barrier (D). In the next well this behaviour will be repeated yielding an inchworm type motion. Reproduced after [98] with kind permission from Europhysics letters (https://www.epletters.net)*

(Totally) Asymmetric Simple Exclusion Process With Langmuir Kinetics

The Brownian ratchet gives a good description of how a molecular motor or a motor-cargo complex can move processively along a cytoskeletal filament. However, it does not account for the processivity of molecular motors as, binding to, and detaching from, the bio-filament is not included. Parmeggiani et al. [101, 102] adapted the *Totally Asymmetric Simple Exclusion Process* (TASEP) to capture both the biased diffusion and motor processivity in one model. The basic TASEP is an extension of stochastic lattice gas models and was first introduced in 1968 as a theoretical model for describing the kinetics of biopolymerisation [103]. Whereas the TASEP only allows for forward stepping, there exists also an ASEP (*Asymmetric Simple Exclusion Process*). The latter model captures a biased diffusion that does allow for back stepping. Both TASEP and ASEP are non-equilibrium steady-state models that require a constant gain or loss of energy. The models have many applications, including modelling of car traffic and ant trails (see reviews [104, 105]).

In the adapted TASEP of Parmeggiani et al. (Fig.3.4A), the bio-filament is mapped on a lattice of nodes and molecular motors are entering the filament from the left side with a probability α. The motors 'walk' unidirectionally along the filament from left to right. The model incorporates excluded volume thus the adjacent lattice node has to be vacant before a motor can make its move. Motors that reach the end of the filament can leave the filament with the probability β. As mentioned before, in the TASEP model back stepping is forbidden, even though molecular motors are know to step both forward and backwards (see chapter 1). The motor concentration (number density) in the bulk is determined by the choice of the boundary conditions α and β. If $\beta < \alpha$, then a traffic jam of molecular motors can appear at the end of the filament increasing in length with decreasing β. Parmeggiani et al. combine this TASEP model with Langmuir Kinetics (LK), a model that was originally developed to describe the attachment and detachment of gas molecules on a substrate [106]. In LK, motors can detach from the filament with rate ω_{D} and attach with rate ω_{A}. The filament is submerged in a virtual particle (motor) bath from where, at random positions along the filament, motors can attach. Unlike TASEP, LK is in thermal equilibrium and obeys detailed balance. The ratio between the rates of attachment and detachment is called the binding constant, $K = \omega_{\mathrm{A}}/\omega_{\mathrm{D}}$. The concentration in the bulk of the system can be predicted using the Langmuir equilibrium density defined as: $K/(1+K)$*.

We are interested in the situation where the dynamics of LK and TASEP compete. However, these dynamics are dependent on the system length, N. As a motor typically spends a time $\tau \sim 1/\omega_{\mathrm{D}}$ on the lattice, it will visit a number of sites n in the order of $\tau \sim n$. This means that the fraction of sites visited along the filament is $n/N \sim 1/\omega_{\mathrm{D}}N$. In the thermodynamic limit ($N \to \infty$), this fraction of sites would go to zero i.e. the system would be completely dominated by LK. Thus, to enable competition between both models, it is important that the motors spend enough time on the lattice to interact with each other. For this purpose the total detachment (Ω_{D}) and attachment (Ω_{A}) rates are introduced to make them independent of the filament length via:

$$\Omega_{\mathrm{A}} = \omega_{\mathrm{A}}N \qquad \text{and} \qquad \Omega_{\mathrm{D}} = \omega_{\mathrm{D}}N. \tag{3.1}$$

In Fig.3.4B it is shown that the dynamics of both TASEP and LK can be recovered by the model by tuning the detachment rate. For small values of Ω_{D} (and constant α, β, K and N), the TASEP mechanism dominates the system. Here the detachment and attachment rates are very small such that the motors spend most of their time along the bio-filament. For large Ω_{D} the dynamics are determined completely by the Langmuir kinetics. Motors continuously appear on and disappear from the filament. However, when the TASEP and LK processes compete i.e. when motors spend enough time 'walking' along the filament to interact, different dynamics are found. There is competition between bulk and boundary dynamics resulting in a non-monotonic concentration profile on the filament. For $\Omega_{\mathrm{D}} = 0.1$ in Fig.3.4B regions of low and high motor concentration are shown separated by a steep rise in concentration. At the beginning of the filament TASEP dominates, followed by a domain wall after which the Langmuir dynamics rule. Finally there is a depletion effect at the end of the filament. The width of this domain wall decreases with increasing filament length (see Fig.3.4C)†.

---

[*] Parmeggiani et al. [101, 102] assume a constant motor concentration of unity in the bulk during attachment and detachment.

[†] For constant values of α, β and K.

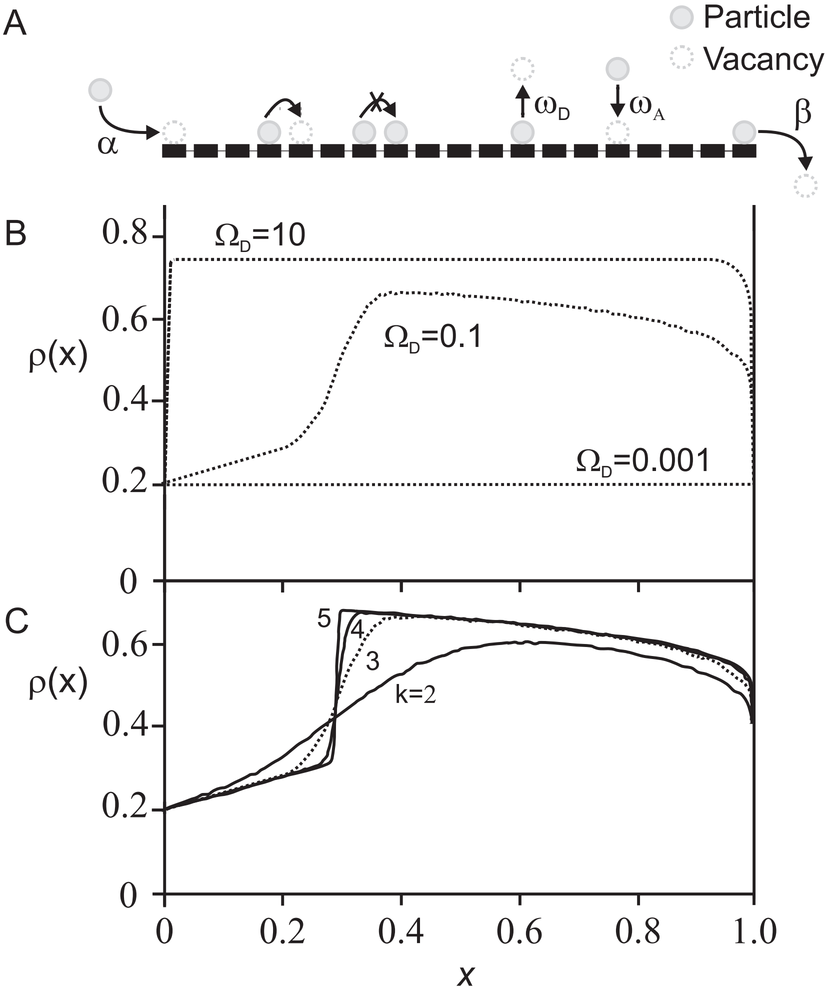

Figure 3.4: *TASEP model with Langmuir Kinetics. A) The different moves on the one-dimensional lattice. Two different mechanisms are shown. First there is the hopping mechanism (TASEP) governed by the difference in ingoing and outgoing rates,* $\alpha = 0.2$ *and* $\beta = 0.6$ *respectively. The second mechanism (Langmuir Kinetics) is bulk attachment and detachment with rates* ω_{A} *and* ω_{D}*. The ratio between these values is* K*, and is fixed to a value of 3. Excluded volume interactions are accounted for. B) Three different curves are shown for different* Ω_{D}*, where* $N = 10^3$ *is the number of binding sites,* i*, the index of a binding site and* $x \equiv i/N$*. For small* Ω_{D} *(and small* Ω_{A}*), the TASEP mechanism dominates the dynamics. For large* Ω_{D} *(and small* Ω_{A}*) the Langmuir kinetics dominate. The intermediate* Ω_{D} *(and intermediate* Ω_{A}*) shows a behaviour that depends on both mechanisms, yielding a low and high density region separated by a domain wall. C) The width of the domain wall in Fig.B decreases with increasing system length (at constant* Ω_{D}*). The system length is given by* $N = 10^{\mathrm{k}}$*. Reprinted figure with permission from [101]. Copyright 2013 by the American Physical Society.*

Extensions Of The TASEP/LK Model

The model of Parmeggiani et al. [101, 102] was extended after experimental work by Mallik et al. [107] showed that dynein motors can walk with steps of 8, 16, 24 or 32 nm along a microtubule depending on the free space available along the filament. To model this hindrance-dependent stepping behaviour of a dynein protein, Kunwar et al. [108] combined the TASEP with the *Aggressive Driving Model* (ADM) that allows for motors to walk between 1 and 4 lattice nodes per time step depending on the number of vacant lattice nodes.

Other authors focus on different types of interaction between the motors and the filamentous track they walk on. Among these applications are the *burned-bridge model*, where part of the filament becomes unavailable after a molecular motor has walked upon it [109–111]. In addition, Klumpp et al. [112] reported an ASEP where the filament consists of active compartments, where processive motion takes place, and diffusive compartments where an unbiased random walk takes place. Moreover, the influence of defects on the bio-filament in the form of road blocks [113] that obstruct the motion, have been studied. Also, the dynamics at junctions of multiple filaments have been reported [114, 115].

Another line of research takes advantage of the stochastic lattice gas models to understand the behaviour of different species of motors on a filament. Chai et al. [116] modelled motors with different stepping rates and detachment probabilities along the same filament. Similarly, motors of opposite polarities sharing the same filament have been studied [117, 118]. The latter could occur on a microtubule where kinesin and dynein motors walk in opposite directions or could apply to actin filaments where plus and minus end myosin motors exist (see chapter 1). In addition, motion of molecular motors via occupancy facilitation has been studied [119]. In the latter model a motor only steps when the next site is vacant and the previous site is occupied. Furthermore, Goldman et al. presented an ASEP of molecular motors with cargoes [120] and followed this work with a model that allows for 'cargo-hopping' from one motor to another. The latter occurs when a cargo carrying motors' path is blocked by another motor [121].

Two Lane Exclusion Processes

The exclusion process models discussed so far did not include interactions between lanes nor were the number of motors conserved in the system. To study this, models have been developed where two lanes of lattice nodes exist parallel to each other. The lanes can be identical in properties or different. Interaction between both lanes takes place via Langmuir kinetics.

Evans et al. [122] introduced a two lane model consisting of a TASEP lane (biased diffusion) and a diffusive lane where motors experience a one-dimensional random walk. A motor can thus detach from a filament, diffuse and rebind to the filament again, thus conserving mass in the system. In the approach of Ebbinghaus et al. [123] the model consists of a TASEP lane and a diffusional lane where no excluded volume is taken into account. Two kinds of motors exist that move in opposite directions. This way, the authors model a microtubule occupied by both kinesin and dynein and study their dynamics. They followed this work [124] for different properties of the diffusive lane and by introducing (temporary) defects along the TASEP lane.

Furthermore, different situations of two parallel TASEP have been studied. Shi et al. [125] studied the dynamics of two TASEP with lane changing via Langmuir kinetics. Additionally, Melbinger et al. [126] (building on a model by Popkov et al. [127]) presented a two lane TASEP without Langmuir kinetics. However, the motion of motors on one TASEP is restricted by the position of motors along the other filament thereby including mutual excluded volume effects. This situation can occur in a cell when cytoskeletal tracks are in close approximation or when multiple tracks along a microtubule are followed by different motors. Finally, the two lane ASEP of Juhász et al. [128] consists of two lanes of opposite polarity permitting lane changes.

Motor Interactions With The Environment

The model presented by Parmeggiani et al. [101,102] and its extensions incorporates the processivity of molecular motors in combination with their directed motion. However, it fails to describe the interaction of the active motors with the environment. In the cell, the molecular motors alternate between periods where they are bound to the cytoskeleton and periods where the diffuse freely through the cell's cytosol [24]. Therefore, a more realistic model should incorporate motor interactions with the environment.

Exclusion Processes With Solution

The first molecular motor model that built upon exclusion processes and incorporated interaction with the surrounding medium was presented by Lipowsky et al. [129,130]. The model consists of a system where both the bio-filament(s) and the solution are mapped upon a lattice with lattice spacing, l, equal to the diameter of the molecular motor with cargo. In the solution, suspended motors or motor-organelle complexes, perform a random walk. In one simulation time step a motor is restricted to a move of ± 1, in all x, y and z-directions with probability p (see Fig.3.5A). The probability depends on the number of dimensions, s, in which the random walk takes place and is given by: $p = 1/2s$. The sum of these probabilities is unity. The diffusion in 'solution' is purely a random walk which is independent of the motor's location in the solution and on the motor concentration. The diffusion constant is chosen to be a constant for each suspended object, therefore, hydrodynamic interactions are neglected in this model. In addition, excluded volume interactions are taken into account by allowing only one motor at a lattice node at given moment in time. Furthermore, the filament is modelled as an ASEP with LK dynamics, allowing for forward and backward steps as well as including the motor processivity. Hence, the bound motors are subject to a biased random walk. The motors are driven along the lattice according to the following probabilities: α (forward), β (backward), γ (detachment) or δ (dwelling) (see Fig.3.5B). As it was the case in solution, the sum of these probabilities is unity. The velocity of the bound motors is imposed by the degree of bias: $V = (\bar{\alpha} - \bar{\beta})l/\tau$ in which $\bar{\alpha} \equiv \alpha/(\alpha + \beta + \gamma)$, $\bar{\beta} \equiv \beta/(\alpha + \beta + \gamma)$ and τ a time constant. As mentioned above, the suspended motors can move to any of the adjacent lattice nodes with equal probability. Therefore, a motor in a lattice node adjacent to the bio-filament can attach to the filament with finite probability provided that the lattice node is not occupied. This move will next be accepted with probability π. A more detailed description of the dynamics on the bio-filament and the detachment and attachment of motors can be found in appendix A.

Lipowsky et al. used this model to study the relevance of the fluid on the motor dynamics in different geometries for both open and closed systems. For example, they studied motor transport in a closed tube in which one filament is present that is positioned in axial direction along the tube wall [129]. The filament is treated as a TASEP with LK, thus bound motors are only allowed to step forwards towards the plus-end ($\beta = 0$) or detach. Motors are not allowed to cross the confining walls that close off the tube. Even at small motor concentrations self-organisation will take place in the system. As can be seen for $N = 40$ in Fig.3.5C, the unidirectional motion of the motors results in a 'traffic jam' or area of high motor concentration at the end of the filament. This bound motor concentration drops off rapidly after the beginning of the jam is reached. Since the bound motors accumulate at the end of the filament, there will be more motors detaching in that region. This results in a motor gradient in solution which yields a flux of motors in opposite direction. The unbound motor flux balances the bound motor flux establishing a stationary non-equilibrium state. Fig.3.5C shows that the length of the traffic jam increase with the number of motors ($N = 150$) in the system, until the filament becomes almost saturated ($N = 250$).

This flexible model was easily adapted to study collective effects in different geometries. For example, the random walks of molecular motors in a system of immobilised bio-filaments in two and three dimensions have been studied in more detail [131], as is transport in systems with different filament arrangements, including uni-axial and aster-like configurations [132,133]. Additionally, the tug-of-war between different types of competing molecular motors attached to a cargo has been considered [134–136]. Moreover, the motor stepping behaviour and in particular the binding and unbinding dynamics with changing motor traffic density [137] has been investigated. In addition, defects in the filaments and the presence of microtubule associated proteins have been

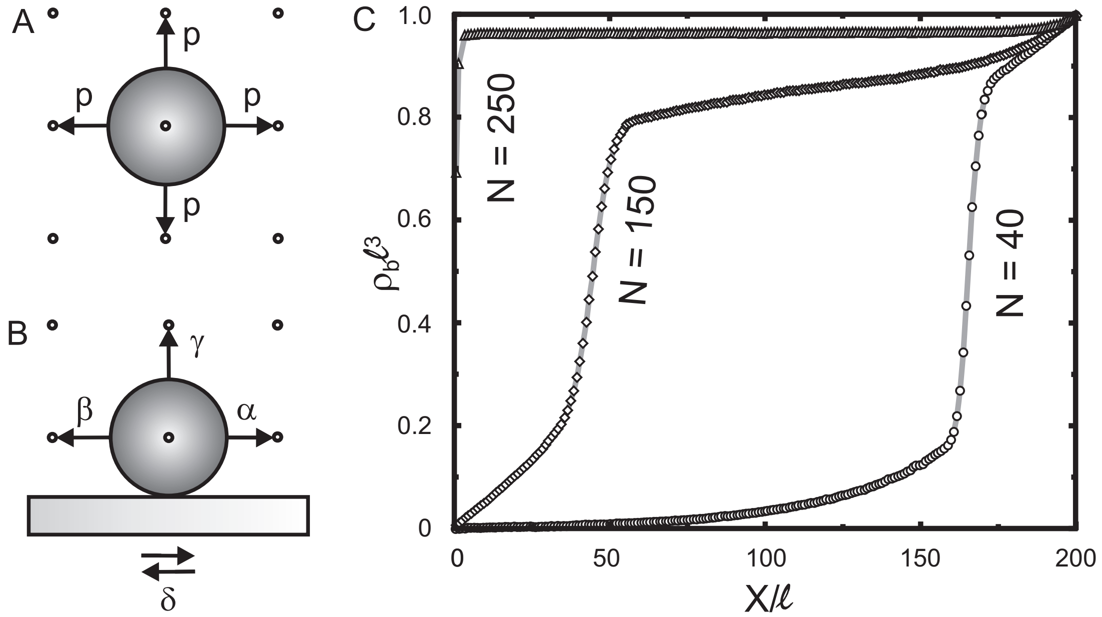

Figure 3.5: *Lipowsky model. A) In solution the motor can diffuse freely with equal probability to any of the four adjacent lattice nodes on a 2d lattice. The model can be adapted to be used in one, two or three dimensions. B) The dynamics of a bound motor protein. The protein moves with the following probabilities: forward (α), backward (β), detachment from the filament (γ) or dwelling (δ). C) Normalised steady-state concentration profile, $\rho_\mathrm{b} l^3$, of molecular motors bound to a single filament in a closed tube. The filament is located at the bottom of the tube. The position on the filament is given by, X, in units of the lattice spacing, l, and the filament diameter $D = l$. The motors move towards the positive end of the filament that is located at $X = 200l$. The tube has length, $L = 200l$, and width, $W = 25l$, N indicates the total number of motors and N_b, the bound motors. The bound density is given by: $\rho_\mathrm{b} = N_\mathrm{b}/D^2L = N_\mathrm{b}/200l^3$. Reprinted figure with permission from [129]. Copyright 2013 by the American Physical Society.*

studied [138]. Similarly, one of these proteins, the tau protein was the topic for another group (Grzeschik et al. [139]). The tau protein may reduce the tubulin affinity of the motors [140, 141]. This could be important for understanding Alzheimer's disease, which is linked to an altered tau metabolism, resulting in neuronal disorders known as tauopathies [142].

Continuum Models

The importance of the interaction of the motors with the surrounding medium has also been studied in an off-lattice or continuum environment. For example, Surrey et al. [143, 144] presented experimental work and simulations of active polymer solutions where solutions of molecular motors (both plus and minus end) and bio-filaments give rise spontaneously to different filament geometries. The shape of these geometries depends upon the motor concentration, motor type and motor processivity. The simulations make use of a set of coupled kinetic equations that describe both the bound and unbound motors respectively.

The influence of a more realistic medium by including hydrodynamic interactions has also been studied in the continuum. Korn et al. [145] studied the binding of a motor-cargo complex to a receptor on the filament. In addition, they studied how the transport of a cargo along a cytoskeletal element is influenced when there are multiple molecular motors present on the cargo [146]. In these simulations hydrodynamic interactions between the cargo and wall (filament) are taken into account. The motor motion is modelled via numerical integration of the Langevin Equation. The simulations show that the mean transport length increases exponentially with the amount of motors attached. This result is in agreement with earlier simulations presented by the same group [134] and with experimental work [147, 148].

Chapter 4

Cell Transport Enhanced By Hydrodynamic Interactions

In the following 3 chapters, the effect of the solvent on the transport of bound and suspended molecular motors with cargoes will be analysed. The simulation models described in this chapter, and those in chapter 6, were developed in close collaboration with Ignacio Pagonabarraga (Departament de Física Fonamental, Universitat de Barcelona, Spain). The experimental work was performed by Agnieszka Esseling-Ozdoba in the group of Anne-Mie Emons (Wageningen University, Laboratory of Plant Cell Biology, the Netherlands). In this chapter results are presented that were obtained via simulation studies using a lattice model. Most of these results have been published [149]. Experimental work done in the group of Prof. Emons is discussed in chapter 5 and in [150]. In chapter 6, results obtained using a subsequently developed continuum model, are presented.

This chapter is an extended version of the original publication: D. Houtman et al., "Hydrodynamic flow caused by active transport along cytoskeletal elements" *EPL*, 2007, 78 [149] and has been reproduced with kind permission from EPL (Europhysics Letters) - IOPscience. In addition, it features a section where the effect of the choice of the mobility tensor is discussed. Moreover, the simulations are repeated for a system with two filaments of opposite polarities. Finally, the motor-cargo transport is studied for the situation where there are gaps in the cytoskeleton.

Introduction

In chapter 2 it was shown by means of *the Stokes number* (eq.2.27) that small suspended organelles and other suspended cytoplasmic objects are sensitive to momentum transport via each other's flow field. Thus, the motion of these organelles will be affected through hydrodynamic interactions. However, this effect alone will not necessarily give rise to enhanced transport inside the cell. In most situations it has a negligible effect as the cell's cytosol is a crowded environment consisting of a multitude of cytoskeletal elements with small mesh size [151]. Moreover, organelles are dragged towards both the plus and minus ends of the individual bio-filaments (see chapter 1) mostly cancelling out the hydrodynamic effects. Therefore, for the momentum transfer via the fluid to have a positive effect on the transport, a number of conditions need to be met. Firstly, many cargoes have to be actively transported simultaneously along the same or along different bio-filaments. This is a key requirement as the hydrodynamic drag is additive. Secondly, the bulk of this transport has to take place in unidirectional fashion as motion in opposite direction will counteract the effect. Thirdly, to maximise the effect, the cytoskeletal elements have to be oriented more or less parallel to each other. Finally, the fluid friction force acting upon an organelle is larger in a viscous fluid, such as cytosol, than in water. Thus, the effect of the additional positive force on the organelle via hydrodynamic interactions is desirable in a viscous fluid. See Fig.1.3 in chapter 1, where it is shown that adding molecular motors (i.e. a positive force) to an organelle has only a small effect on its velocity in water. However, it yields a substantial velocity increase in the cell. Different systems exist that abide to the above. We will limit ourselves to two situations, cytoplasmic streaming in plant cells [30] and axoplasmic streaming in neurons [152]. In cytoplasmic streaming the bound and suspended organelles follow a given trajectory through the entire cell (e.g. see Fig.4.1 for cytoplasmic streaming in *Tradescantia virginiana*). In neurons organelles can be transported from one extreme of the neuron to another[*]. In both systems, the transport takes place on very long length scales with respect to the size of the cargoes (≈500 nm[†]). It is this transport that will be analysed using computer simulations. For the remainder of the chapter, motor-cargo complexes will be referred to as motors, unless specified otherwise.

Expanding The Exclusion Process With a Solution

As discussed in chapter 3, Lipowsky et al. [129, 130] were the first to present an exclusion process that captures the dynamics of molecular motors (with or without cargoes) along a bio-filament as well as the diffusion of the motors in solution. Both the driven motion along the bio-filament and the diffusion in solution are mapped on a lattice. Furthermore, the motor positions are confined to the lattice nodes with spacing, l. The mesh size is proportional to the motor diameter. In addition, excluded volume is taken into account by treating the motors as hard spheres. Thus, allowing for only one motor on a lattice site at a given moment in time.

---

[*] The length of the *recurring laryngeal nerve* of a Giraffe can be up to 5 meter and the nerve cells in a Blue Whale are estimated to be 30 m long [153].

[†] See table 1.1.

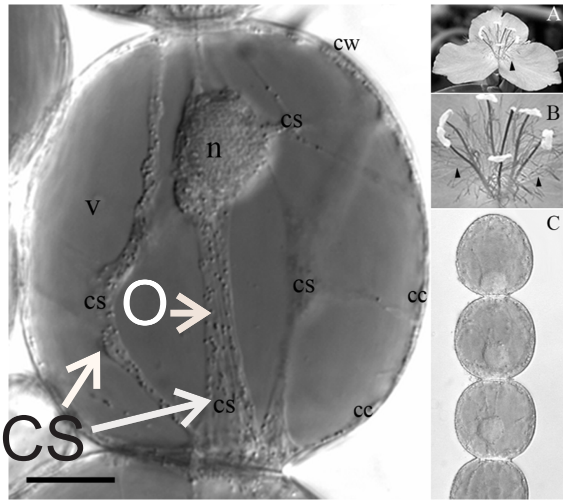

Figure 4.1: *Tradescantia virginiana (spiderwort) stamen hair cell. The cytoplasmic strands (CS) contain organelles (O) (white arrow); n- nucleus, v- vacuole, cc- cortical cytoplasm, cw- cell wall. Bar = 20 μm. Inserts: A. Flower of (T. virginiana), B. Magnification of stamens, arrowheads indicate stamen hairs, C. Single stamen hair.*

During one simulation time step, a motor is allowed to move to an adjacent lattice node in x, y and z-direction or dwell in its position. This yields a maximum displacement, x, per time step of $x = \sqrt{s}l$ where, s, is the number of dimensions in the system. The bio-filament(s) are modelled as a linear array of lattice nodes with properties different from those in solution (see Fig.3.5) accounting for the dynamics of bound and suspended motors. We define the motor concentration in the solution, ϕ_{s}, and on the bio-filament, ϕ_{μ}, as the fraction of lattice nodes occupied by motors. This model will be expanded and adapted in the next sections to analyse the importance of hydrodynamic interactions in intra-cellular transport. A more detailed description of the dynamics of the bound motors and the detaching from and attaching to the bio-filament can be found in appendix A.

Moving Along The Lattice

The dynamics of the ASEP-type bio-filaments and the solution are adapted to model the influence of the fluid on the motor transport. Rather than performing costly simulations where the motors, bio-filaments and the very large number of cytosol molecules are modelled individually, an approximate method is used [69]. This method involves omitting the cytosol molecules and introducing the influence of the solution on the solutes as a combination of random forces and frictional terms. For this purpose the equation of motion for suspended objects, the Langevin equation, will be mapped on the lattice. This equation depends upon the physical parameters of the motors and takes the friction of the cytosol into account. More importantly, via this equation the momentum transfer giving rise to hydrodynamic interactions between the different motors can be studied (see chapter 2). The Langevin equation that describes the motion of an organelle i in a solution of organelles j is given by:

$$\frac{d\boldsymbol{r}_{\mathrm{i}}}{dt} = \boldsymbol{V}_{\mathrm{i}} = \boldsymbol{\mu}_{\mathrm{ii}} \cdot \boldsymbol{F}_{\mathrm{i}} + \sum_{\mathrm{j,j\neq i}} \boldsymbol{\mu}_{\mathrm{ij}} \cdot \boldsymbol{F}_{\mathrm{j}} + \boldsymbol{g}_{\mathrm{i}}(t) = \boldsymbol{V}_{\mathrm{i,0}} + \boldsymbol{V}_{\mathrm{i,d}} + \boldsymbol{V}_{\mathrm{i,r}}. \tag{4.1}$$

In this equation, $\boldsymbol{V}_{\mathrm{i,0}} = \boldsymbol{\mu}_{\mathrm{ii}} \cdot \boldsymbol{F}_{\mathrm{i}} = (V_0, 0, 0)$, is the ballistic self-velocity of the organelle that depends on the organelle's mobility and the molecular motor force acting upon it. The hydrodynamic interactions of organelles j on organelle i are given by: $\boldsymbol{V}_{\mathrm{i,d}} = \sum_{\mathrm{j,j\neq i}} \boldsymbol{\mu}_{\mathrm{ij}} \cdot \boldsymbol{F}_{\mathrm{j}}$. This additive effect depends upon the force on each organelle as well as the position dependent inter-organelle mobilities $\boldsymbol{\mu}_{\mathrm{ij}}$. Note that the forces depend upon the motor's position in the system. The force generated by bound molecular motors through hydrolysing ATP is non-zero $\boldsymbol{F}_{\mathrm{i}} = (F_0, 0, 0)$. However, motors suspended in solution are not attached to a bio-filament and therefore cannot propel themselves, hence the driving force is zero for these organelles $\boldsymbol{F}_{\mathrm{i}} = (0, 0, 0)$. Finally, the random velocities from thermal fluctuations are accounted for via, $\boldsymbol{V}_{\mathrm{i,r}}(t)$, which have the following properties [63]:

$$\begin{aligned} \langle \boldsymbol{V}_{\mathrm{i,r}}(t) \rangle &= \mathbf{0} \\ \langle \boldsymbol{V}_{\mathrm{i,r}}(t) \boldsymbol{V}_{\mathrm{j,r}}(t^{'}) \rangle &= 2\boldsymbol{D}_{\mathrm{ij}} \delta(t - t^{'}). \end{aligned} \tag{4.2}$$

As mentioned in chapter 2, these random velocities are not statistically independent as they rely on the motor positions, via $\boldsymbol{D}_{\mathrm{ij}}$, in the system. In order to calculate the time evolution of the system, the tensor $\boldsymbol{D}_{\mathrm{ij}}$ needs to be calculated at the beginning of each time step. Where, $\boldsymbol{D}_{\mathrm{ij}}$, a set of 3×3 matrices for each pair of motors, represents the diffusive and frictional effects in a dilute system [69]. The generation of correlated random numbers is described in the section on the Ermak and McCammon Algorithm below.

Ermak and McCammon Algorithm

Ermak and McCammon [72] presented an algorithm that uses normal random deviates*, ζ, to generate the correlated random numbers needed for simulating the Langevin equation. The algorithm consists of four steps: Firstly, at the beginning of a simulation time step, a matrix is generated consisting of elements $\boldsymbol{C}_{\mathrm{ij}} = 2\boldsymbol{D}_{\mathrm{ij}}$. Here, the indices, ij, refer either to one motor (for $i = j$) or to a pair of motors ($i \neq j$). Secondly, since $\boldsymbol{C}$ is a square, symmetrical and positive definite matrix [154, 155] a Cholesky Decomposition ($\boldsymbol{C} = \boldsymbol{L}\boldsymbol{L}^{\mathrm{T}}$) [155] can be used where, $\boldsymbol{L}$, is a lower triangular matrix and, $\boldsymbol{L}^{\mathrm{T}}$, its

---

*$\{\zeta_{\mathrm{i}}\}; \langle \zeta_{\mathrm{i}} \rangle = 0; \langle \zeta_{\mathrm{i}} \zeta_{\mathrm{j}} \rangle = 2\delta_{\mathrm{ij}} \Delta t$ [72].

transpose. The elements of the matrix, $\boldsymbol{L}_{\mathrm{ij}}$, are constructed using the following recursive algorithm:

$$\begin{aligned}
\boldsymbol{L}_{\mathrm{ii}} &= \left[\boldsymbol{C}_{\mathrm{ii}} - \sum_{\mathrm{k}=1}^{\mathrm{i}-1} \boldsymbol{L}_{\mathrm{ik}}^{2}\right]^{0.5} \\
\boldsymbol{L}_{\mathrm{ij}} &= \frac{\boldsymbol{C}_{\mathrm{ij}} - \sum_{\mathrm{k}=1}^{\mathrm{j}-1} \boldsymbol{L}_{\mathrm{ik}} \boldsymbol{L}_{\mathrm{jk}}}{\boldsymbol{L}_{\mathrm{jj}}}
\end{aligned} \tag{4.3}$$

Thirdly, a set of uncorrelated random numbers, ζ_{j}, is generated for each motor in each dimension. Finally, the values $\boldsymbol{L}_{\mathrm{ij}}$ are used as weighing factors to yield the correlated random velocities, $\boldsymbol{g}_{\mathrm{i}}(t)$, using:

$$\boldsymbol{g}_{\mathrm{i}}(t) = \boldsymbol{V}_{\mathrm{i,r}} = \sum_{\mathrm{j}=1}^{\mathrm{i}} \boldsymbol{L}_{\mathrm{ij}} \zeta_{\mathrm{j}}. \tag{4.4}$$

In other words this means that motor 1 diffuses freely (not statistically correlated) through the solution. The diffusion of motor 2 however cannot be chosen at random as motor 1 has generated a flow field in solution via momentum transfer. Therefore, its random velocity needs to be correlated to correct for the hydrodynamic interactions via the flow field of motor 1. Subsequently, the diffusive motion of the third motor needs to be correlated to correct for the flow fields set up by the first two motors, etc.

Allowing For Larger Displacements

The Lipowsky model is further extended by allowing for moves of magnitudes $\pm 2l$ additionally to the original $\pm 1l$ and dwell steps in x, y, and z-directions. This increases the maximum displacement per time step to $x = 2\sqrt{s}l$. The calculated velocities are translated into displacements per simulation time step using the following recipe: for small displacements, $\leq 0.25l$, the motors are forced to dwell in their current position; Intermediate displacements, $0.25l < |\Delta x| < 1.5l$, causes the motor to displace one lattice node. Displacements larger then $1.5l$ are restricted to a move of two lattice nodes. Note that excluded volume always has to be accounted for and thus moves of $\pm 2l$ are only permitted if the whole path is free. If the second node is occupied the motor will only displace one node. The displacement recipe is shown in Fig.4.2 below. Note that this description gives rise to spurious lattice effects. The latter is discussed in appendix B.

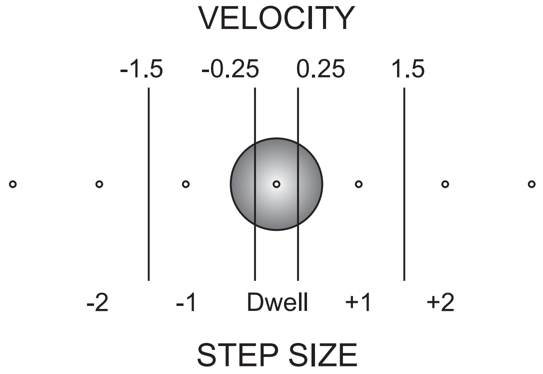

Figure 4.2: *Mapping of calculated motor displacements on the lattice. Small displacements,* $-0.25l < \Delta x < 0.25l$ *will cause the motor to dwell in its current position. Intermediate displacements,* $0.25l \leq |\Delta x| \leq 1.5l$*, will be mapped on the adjacent lattice node. Large steps,* $|\Delta x| \geq 1.5l$ *will be mapped on the second neighbour node.*

Langmuir-type Kinetics

Next, the motor processivity is accounted for by allowing the motors to detach from the bio-filament with a given probability γ_{d}. Motors in solution close to the filament, in turn, can attach to the bio-filament with probability γ_{a}. Motor interchange between the bio-filament and the solution determines the ratio between the solution and filament volume fractions, ϕ_{s} and ϕ_{μ} respectively. Assuming uniform concentrations along the microtubule and in the solution, the mass flux balance that predicts the steady state relationship between solution concentration and bio-filament occupation is given by:

$$\begin{aligned} \text{Particle flux out} &= \text{Particle flux in} \\ \phi_{\mu}\left(1-\phi_{\mathrm{s}}\right)\gamma_{\mathrm{d}} &= p_1\phi_{\mathrm{s}}\left(1-\phi_{\mu}\right)\gamma_{\mathrm{a}} + p_2\phi_{\mathrm{s}}\left(1-\phi_{\mathrm{s}}\right)\left(1-\phi_{\mu}\right)\gamma_{\mathrm{a}} \\ \phi_{\mu} &= \frac{1}{1+\frac{\gamma_{\mathrm{d}}(1-\phi_{\mathrm{s}})}{\gamma_{\mathrm{a}}\phi_{\mathrm{s}}[p_1+p_2(1-\phi_{\mathrm{s}})]}}. \end{aligned} \tag{4.5}$$

Here, p_1, is the probability the motors diffuse towards the bio-filament from a lattice node adjacent to the bio-filament. Moreover, p_2, is the probability to attach from the second neighbouring row of nodes. These probabilities are a direct consequence of the magnitude of the diffusion coefficient. For the simulations in the result sections, we have chosen values of γ_{d} to ensure the required filament and solution concentrations. We have found that using $\gamma_{\mathrm{a}} = \sqrt{2D_0}$, p_1=0.4 and p_2=0.2 for desired values ϕ_{s} and ϕ_{μ} yields the following estimate for γ_{d}:

$$\gamma_{\mathrm{d}} = \sqrt{2D_0}\phi_{\mathrm{s}} \left(\frac{0.4}{(1-\phi_{\mathrm{s}})} + 0.2 \right) \left(\frac{1}{\phi_\mu} - 1 \right). \tag{4.6}$$

Conversion Of Units

We will use the experimental data from the reference system presented in chapter 2 (table 2.2) for the motor-organelle complexes in the simulations. However, these values are very small (e.g. F_0=4.15$\times10^{-12}$ N) and could cause inaccurate results, via round-up errors, due to the computer's finite numerical accuracy. Therefore, similar to the method of reduced units [69,156], the relevant simulation parameters need to be of order one. To translate the experimental data to the simulations it is necessary to fix three simulation parameters from which all other values can be calculated. Using the experimental data for the radius, force and velocity and by fixing these values in the simulation model we obtain the following conversion factors for length L, time T and mass M. The conversion between lattice units and the experimental data is given in table 4.1.

Property	Unit	Experiments	Model	Factor	Calculated
a	m	2.5 $\times10^{-7}$	0.1	L	2.5 $\times10^{-7}$
V_0	m/s	8.0 $\times10^{-7}$	0.4	L/T	8.0 $\times10^{-7}$
F_0	N	4.15 $\times10^{-12}$	1.061	ML/T^2	4.15 $\times10^{-12}$
μ_0	m/Ns	1.93 $\times10^{5}$	0.3769	T/M	1.93 $\times10^{5}$
η	Pas	1.1	1.407	M/LT	1.1
ρ	kg/m^3	1200	7.67 $\times10^{-9}$	M/L^3	1200
D_0	m^2/s	8.26 $\times10^{-16}$	0.3769	L^2/T	1.89 $\times10^{-12}$
$k_{\mathrm{b}}T$	J	4.28 $\times10^{-21}$	1	ML^2/T^2	9.78 $\times10^{-18}$
m	kg	7.85 $\times10^{-17}$	3.21 $\times10^{-11}$	M	7.85 $\times10^{-17}$
τ	s	1.52 $\times10^{-11}$	1.21 $\times10^{-11}$	T	1.51 $\times10^{-11}$

Table 4.1: *Conversion table between lattice units and experimental data (See table 2.2 in chapter 2). The conversion factors are:* L=2.5×10^{-6}, T=1.25, M=2.4446×10^{-6} *and were determined by fixing the radius (a), velocity (V_0) and force (F_0) in the simulation model*. The column 'calculated' is obtained by multiplication of the columns 'model' and 'factor' and it reflects how well the simulation parameters represent the experimental data.*

The table shows that the found conversion factors can be used to retrieve the experimental values from the simulation settings. However, the moves of the motor-organelle complexes in the simulations are mapped on a lattice using the method described in

---

[*] For a=0.2 the conversion factors become: L=1.25×10^{-6}, T=0.625, M=1.2223×10^{-6}.

Fig.4.2. To recover the bound motor velocities in the system, the motor diffusion has to be large enough to span the range of moves described in the mapping algorithm. To ensure this the thermal energy ($k_{\mathrm{b}}T$) had to be increased in the system, thus effectively performing the simulations at a higher temperature. The consequences are a larger diffusion coefficient as can be seen in the column labelled *calculated* of table 4.1. In this thesis we are interested in studying the quantitative effect of hydrodynamic interactions on intra-cellular motor transport. As these interactions depend upon the motor's position, mobility and forces, the larger diffusion coefficient will not modify this behaviour.

Flow Sheet Of Simulation

The simulations are performed according to the flow sheet shown in Fig.4.3. The flow sheet consists of a number of consecutive steps where one step needs to be completed before going to the next. Computer experiments are not that different from real experiments. As Frenkel and Smit [156] point out in their book the basic steps are the same. Firstly, a sample needs to be prepared. This happens in the initialisation step. Here, motors are distributed randomly along the bio-filament and in solution until the desired occupation fractions are reached. Secondly, the system is allowed to reach a steady-state[*] situation during a predetermined number of simulation steps. At the start of each simulation time step, the inter-organelle forces, mobilities, and velocities are calculated after which the motors are displaced along the lattice. The size of the moves is determined via calculation of the different motor velocity components (eq.4.1). The resulting velocity is subsequently mapped on the lattice using the procedure shown in Fig.4.2. Next, the motors are moved one-by-one to their destinations followed by either rejection or acceptance of the new position by taking excluded volume into account. In the case of organelle collisions, the motors will not be moved. The driving force on these motors is subsequently set to zero to ensure proper calculation of the flow field in the next time step. As the drag velocity on a motor is calculated via, $\boldsymbol{V}_{\mathrm{i,d}} = \sum_{\mathrm{j,j\neq i}} \boldsymbol{\mu}_{\mathrm{ij}} \cdot \boldsymbol{F}_{\mathrm{j}}$, at the beginning of each time step this is necessary. After the steady-state is reached, the velocities, occupation fractions and fluxes will be sampled until the end of the simulations is reached.

Hydrodynamic Interactions in Cytoplasmic Streaming

To quantify the momentum transfer between motors via the fluid, a liquid is embedded between two slabs. These slabs are covered by bio-filaments that have a given polarity. Both the solution and the cytoskeletal elements are mapped on a 3d lattice. We now

---

[*] In steady-state the bio-filament and solution concentrations are, on average, constant in time.

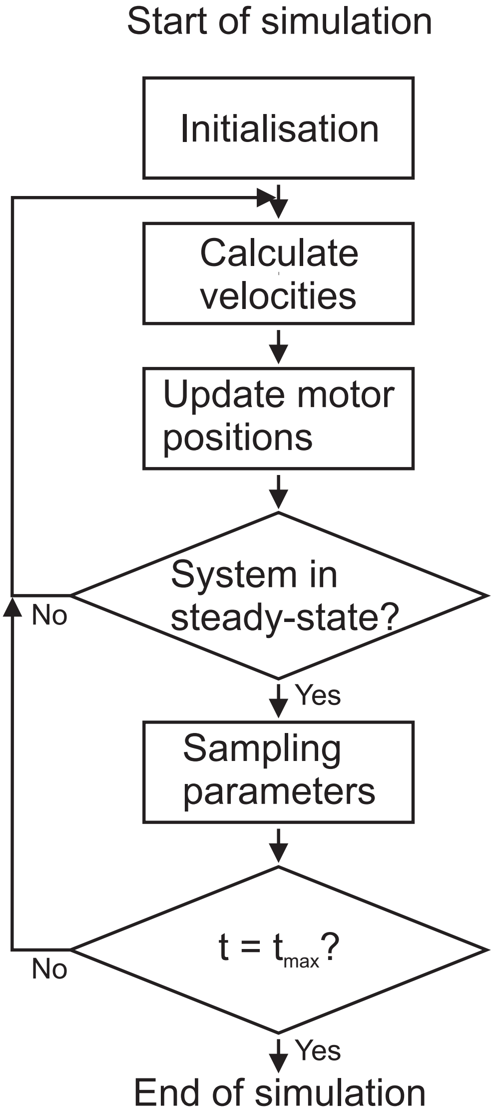

Figure 4.3: *Flow sheet of model. At the initialisation motors are placed in the system. Next, the system is brought in steady-state situation after which velocities, concentrations and fluxes are sampled until the end of the simulation is reached.*

take a 2d cut from our system in the direction perpendicular to the slabs. The resulting 2d system is shown in Fig.4.4.

As a test case we studied cytoplasmic streaming in plant cells (see Fig.4.1). In these cells, cytoplasmic strands are found. These are long, channel-like, structures with a length ranging up to tens of micrometers. In the strands bio-filaments are found that span its entire length or a part of it. The model captures a section of a cytoplasmic

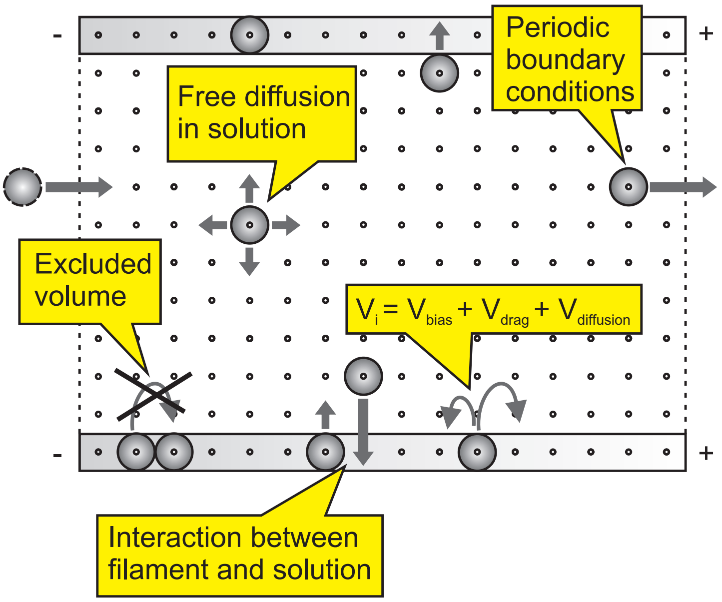

Figure 4.4: *Schematic view of the model system, i.e. a cytoplasmic strand in a plant cell. A solution is embedded between two bio-filaments and mapped on a lattice. Moreover, the bio-filaments have a given polarity which determines the walking direction of the motor-cargo complexes. All possible moves of the motor-cargo complexes are shown. Excluded volume and the processivity of the motors are accounted for. To mimic the dynamics of a infinite system, periodic boundary conditions are used in axial direction.*

strand in which many motors a present along the bio-filament and in solution. To study the dynamics of a large strand periodic boundary conditions (PBC) [69,156] are used in axial direction i.e. in the direction of transport. Using PBC is a computational trick to model an infinitely large system with a minimum of computational expense and was originally developed to minimise boundary effects when modelling bulk-phases. Consequently, the model in Fig.4.4 is treated as a primitive cell in an infinite periodic lattice of identical cells. In each cell the number density of motor-cargo complexes is kept constant. If a particle leaves the system, its periodic image will enter. It is unclear what the effect of PBC is on the long-range hydrodynamic interactions as these interactions fall off with $1/r$, which is typically longer than half the box size [69]*. We will limit the hydrodynamic interactions to the nearest images.

---

[*] In the section on different hydrodynamic interaction tensors we correct for this effect by presenting data for a truncated and shifted tensor.

Effect Of Hydrodynamic Interactions On Transport

We have considered the simplest geometry in which motors move in the two dimensional plane confined between two bio-filaments, although the hydrodynamic interactions correspond to those of a 3d fluid (we presume that the structure of the motors in the transverse direction can be neglected). Such a case can be regarded as a suspension of motors between substrates covered by a parallel set of bio-filaments. Such an idealised example contains the basic dynamic couplings and facilitates the analysis. In order to analyse the interplay between activity, excluded volume and hydrodynamic forces, we fix the solution concentration to a small value, $\phi_{\rm s} = 0.05$ and analyse the collective behaviour of the suspension+bio-filament complex at different degrees of bio-filament's occupation. In units of the lattice spacing, l, and simulation time step, Δt, for motors of unit mass we vary the force exerted by the filament between 1/2 and 2 to control the single motor velocity, which should take values of the order (but smaller than) a lattice spacing. Simulations are run for systems size L, containing around 1000 motors and for a few thousand time steps after thermalisation. Within the Oseen description (eq.2.25) it is known that values of A close to the motor radius may lead to numerical instabilities in configurations where motors are close to each other. To avoid such problems, and making use of the linearity of the system, we keep A/l smaller than $1/5$[*]. For these parameters the motor Péclet number (eq.2.34) is of order one[†]. Nevertheless, the results we will discuss should not be severely affected by this fact, since we focus on mean collective motor velocities.

In Fig.4.5A we show the velocity at which motors move along a filament divided by the measured single motor velocity, $\langle V_0 \rangle$, as a function of the filament occupation, ϕ_μ. In the absence of hydrodynamic interactions (HI) the velocity decreases linearly with increasing occupation fraction due to excluded volume interactions. Note that, due to spurious lattice effects, the measured single motor velocity, $\langle V_0 \rangle$, deviates from the nominal single motor velocity that was given by: V_0=$\mu_0 F_0$. For example, for F_0=1.061 and μ_0=0.3769 the nominal velocity is V_0=0.4 while the measured value is $\langle V_0 \rangle$=0.43. See appendix B for an explanation of this effect. Therefore, all normalisations in this chapter are performed using the measured single motor velocities.

When HI are considered, the drag first increases the overall bound motor velocity. At higher concentrations a second regime is achieved, where hindering due to excluded volume effects causes this velocity to decrease. Nevertheless, for all occupations the motor's velocity is larger than the corresponding one in the absence of HI. A second,

---

[*] Kirby [59] mentions in his book that the isolated sphere relation is accurate as long as particle-particle separations exceed x=10A. For a hydrodynamic radius A=0.1l, the minimum particle separation $x_{\rm min} = l - 2A = 0.8l = 8A$ which suggests that the simulation results are less accurate at high ϕ_μ.

[†] For organelles of typical size $l \sim 1\mu m$ that move along a bio-filament with a velocity $u \sim 1\mu m/s$ and assuming a diffusion coefficient of $10^{-12} m^2/s$ we find a Péclet number of order $Pe \sim 1$.

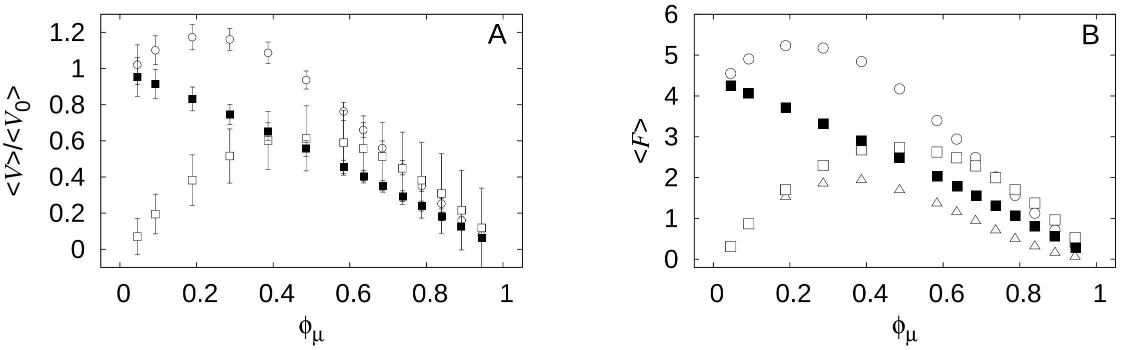

Figure 4.5: *A) The normalised velocity for different degrees of bio-filament occupation,* ϕ_μ*. B) Effective force (in pN) acting on motors for different filament occupations. The open triangles represent the hydrodynamic force acting on the motors. The open circles refer to the bio-filament, the open squares to the solution, the filled squares show data without hydrodynamic interactions. The simulation settings were:* F_0*=1.061,* μ_0*=0.3769,* $\langle V_0 \rangle$*=0.43,* $N_{\mathrm{part}} \approx 1000$*,* $T_{\max}$*=7000 (HI) and 10000 (no HI).*

qualitative, effect of the cooperativity induced by the solvent is displayed in the same figure where we show the average velocity of motors in solution. In the absence of HI motors can only display a net displacement along the bio-filament. However, in the case with HI, there clearly exists a well defined solution velocity which increases with ϕ_μ until it reaches a maximum after which it decreases. Note that with increasing bio-filament concentration the average distance between suspended and bound motors decreases. This results in a larger hydrodynamic coupling i.e. the velocity difference between bound and suspended motors becomes smaller. The position of the maximum depends on the specific parameters considered. There seems to be an optimum bio-filament occupation which is different for both the bio-filament ($\phi_\mu \approx 0.2$) and the solution ($\phi_\mu \approx 0.5$). The position of these maxima seems to be insensitive for all simulation parameters explored (data not shown).

Using table 4.1 the simulation data can be converted into real units. The resulting forces are shown in Fig.4.5B. The largest effective force acting on a bound motor was measured at ϕ_μ=0.2 and equals 5.2 pN, 25% larger than the single motor force needed to move the model organelle through the fluid. This force lies within the stall force of the kinesin motor (5.4±1.0 pN [15]) and shows that the added hydrodynamic force compensates for the drag force acting upon the motors. Moreover, experiments have shown that a positive force exerted upon a bound molecular motor increase its velocity (Kinesin [11]; Myosin-V [55]). The hydrodynamic coupling gives rise to such a force. Interestingly, the maximum hydrodynamic force on bound motors is found to be 1.9 pN at ϕ_μ=0.4. For suspended motors this value can be as large as 2.7 pN (at ϕ_μ=0.5).

At large bio-filament occupations, the average particle separations are small and the Oseen approximation become less accurate*. This in combination with using periodic boundary conditions and spurious lattice effects yields unrealistically large forces.

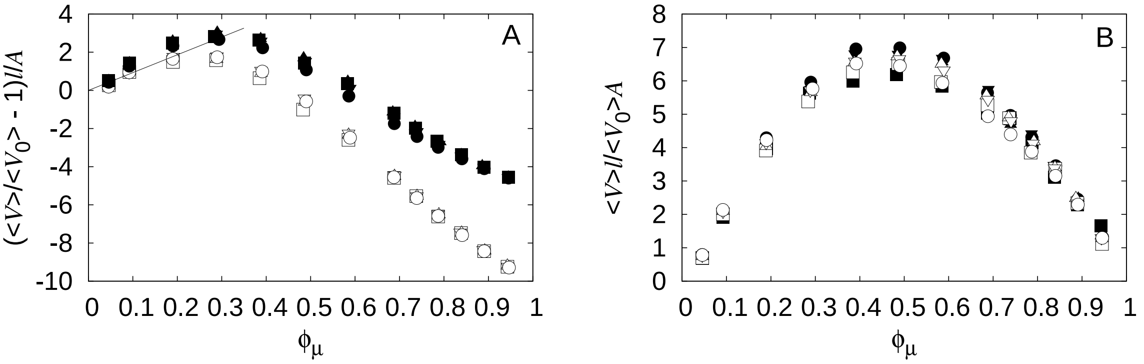

Figure 4.6: *A) Bound motor velocity for different bio-filament occupation, ϕ_μ. $\langle V\rangle$, is the motor velocity, $\langle V_0\rangle$, the measured single motor velocity, a, the hydrodynamic radius and, l, the lattice spacing. The line shows the theoretical expected increase in velocity due to HI (see text and eq.4.8). B) Mean velocity $\langle V\rangle$ in solution for different degrees of filament occupation ϕ_μ, hydrodynamic radius a, and single motor velocity $\langle V_0\rangle$. Open symbols a=0.1l, Filled symbols a=0.2l, μ_0=0.3769, $N_{\rm part}\approx 1000$, $T_{\rm max}$=7000; Squares V_0=0.2, $\langle V_0\rangle$=0.22; Triangles V_0=0.4, $\langle V_0\rangle$=0.43; Inverted triangles V_0=0.6, $\langle V_0\rangle$=0.63; Circles V_0=0.8, $\langle V_0\rangle$=0.83*

In Fig.4.6A, we show the increase of the motors' velocity with respect to their biased velocity. Due to the linearity of the hydrodynamic coupling, in the regime where excluded volume interactions are negligible, the profiles are linear in a. Hence, different systems collapse in a single curve as a function of filament occupation. We can then use eq.4.1 to estimate the initial increase in motors' velocity. By inserting eq.2.25 and by using, $\boldsymbol{V}_0$=$\boldsymbol{\mu}_{\rm jj}\cdot\boldsymbol{F}_{\rm j}$, the equation can be rewritten as:

$$\frac{(\langle\boldsymbol{V}\rangle-\langle\boldsymbol{V}_0\rangle)l}{\langle\boldsymbol{V}_0\rangle a}=\frac{3}{4}\sum\frac{l}{r_{\rm ij}}[\hat{\boldsymbol{I}}+\hat{\boldsymbol{r}}_{\rm ij}\hat{\boldsymbol{r}}_{\rm ij}],\qquad {\rm i}\neq{\rm j}. \tag{4.7}$$

Next, the right hand side can be approximated assuming a continuous and uniform distribution of motors

$$\frac{(\langle\boldsymbol{V}\rangle-\langle\boldsymbol{V}_0\rangle)l}{\langle\boldsymbol{V}_0\rangle a}=\frac{3}{2}l\phi_\mu\ln\frac{L}{2a}\hat{\boldsymbol{r}}_{\rm ij}, \tag{4.8}$$

which agrees quantitatively with the simulation results. For total filament occupation, ϕ_μ=1, motors cannot move along the filament, $\langle V\rangle$=0.

---

[*] See the section 'Different Hydrodynamic Interaction Tensors' below.

In Fig.4.6B we display the mean velocity of unbound motors; these two plots show how the hydrodynamic coupling can be tuned by controlling the motors' size and biased velocity. When using a more realistic choice for the mobility tensor for motors at small separations (Brenner [157], Rotne-Prager [158,159]) this data does not change (see the section on different tensors), indicating that the mechanism described is generic and comes from the algebraic correlations induced by the embedding solvent.

Fig.4.7A shows the concentration of unbound motors across the width, D, of the system. It shows that the interactions between the attached and suspended motors induce a uniform distribution of suspended motors, independently of bio-filament occupation. The hydrodynamic interactions have no effect on the concentration profile between the bio-filaments as the increased concentration near the bio-filament is caused by the Langmuir-type dynamics alone (compare with the black triangles). Also the velocity profile, as displayed in Fig.4.7B, shows that the velocity in solution is modified only in the bio-filaments' neighbourhood, which is more pronounced at higher occupation fractions.

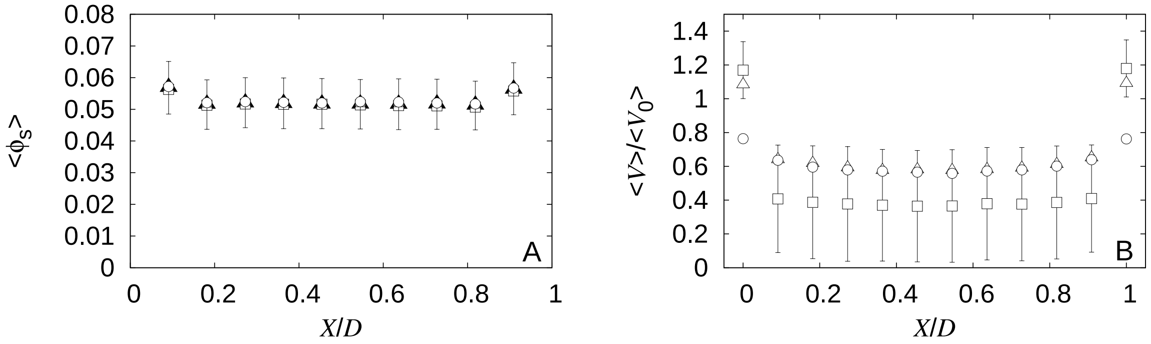

Figure 4.7: *A) Concentration profiles for unbound motors. D is the distance between bio-filaments, and X the distance to the lower bio-filament. Error bars are shown for ϕ_μ=0.2. Closed triangles are for ϕ_μ=0.4 in the absence of hydrodynamic interactions. B) Normalised velocity over the distance, D, between the bio-filaments for a distance, X, from the lower bio-filament for different bio-filament occupation, ϕ_μ. Error bars are shown for ϕ_μ=0.4. For both figures: Open squares ϕ_μ=0.2; open triangles ϕ_μ=0.4; open circles ϕ_μ=0.6. Simulation parameters: F_0=1.061, μ_0=0.3769, $N_{\mathrm{part}}\approx$1000, $T_{\max}$=7000, V_0=0.4 and $\langle V_0\rangle$=0.43.*

Increased Motor Concentration In Solution

The simulations are repeated for a higher motor concentration in solution ($\phi_s=0.1$) for two different values for the biased velocity ($\langle V_0\rangle$=0.43 and $\langle V_0\rangle$=0.63). The normalised velocity for bound motors and suspended motors are presented in Fig.4.8A. The data confirms the robustness of the earlier results both in shape as well as the position of the maxima. However, the velocities are slightly smaller. The latter is a direct result from the increased motor concentration in solution. The larger number of motors increases the probability for detaching motors to collide with motors in solution and thus effectively increasing the motors processivity. This effect is compensated for by choosing the proper detachment probability, γ_{d}, in the simulations (via eq.4.5) and therefore does not lead to large changes in bio-filament concentration.

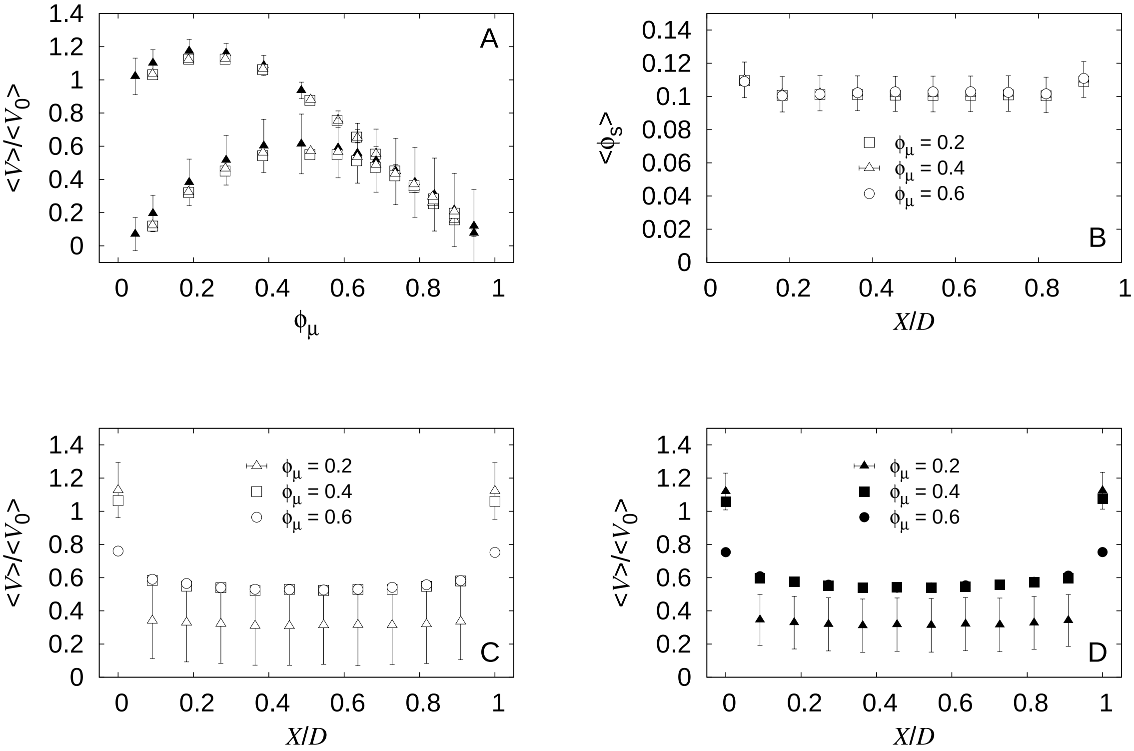

Figure 4.8: *A) The normalised velocity for different degrees of bio-filament occupation, ϕ_μ. Closed triangles: ϕ_{s}=0.05, V_0=0.4 and $\langle V_0\rangle$=0.43. The open symbols represent data for ϕ_{s}=0.1 (open squares V_0=0.4, $\langle V_0\rangle$=0.43, F_0=1.061; open triangles V_0=0.6, $\langle V_0\rangle$=0.63, F_0=1.592). B) Concentration profiles for unbound motors. D is the distance between bio-filaments, and X the distance to the lower bio-filament for ϕ_{s}=0.1, V_0=0.4 and $\langle V_0\rangle$=0.43. C) Normalised velocity over the distance D for V_0=0.4 and $\langle V_0\rangle$=0.43. D) Normalised velocity over the distance D for V_0=0.6 and $\langle V_0\rangle$=0.63. For all figures: μ_0=0.3769; $N_{\mathrm{part}}\approx$1000 (ϕ_{s}=0.05) and $\approx$1200 (ϕ_{s}=0.1); $T_{\max}$=7000*

The motor concentration profile between the bio-filaments is shown in Fig.4.8B (see Fig.4.7A for comparison with ϕ_{s}=0.05). The profile shows that the profile is shifted to the new value of ϕ_{s}=0.1 and $\langle V_0\rangle$=0.43, retaining its overall uniform shape with increased values near the bio-filament due to the interaction of bound and suspended motors.

The solution concentration is not sensitive to the filament occupation. Moreover, the data is robust to the choice of V_0 (data not shown).

The velocity profile for $\langle V_0 \rangle$=0.43 and 0.63 in Fig.4.8C and D respectively. The solution velocities are presented for different bio-filament occupation fractions. The shape of the profile is not modified with increasing suspended motor concentration (compare with Fig.4.7B). Consistently with Fig. 4.8A, the velocity in solution lies below the velocity measured for ϕ_{s}=0.05. Here the error bars are smaller as the statistics are improved with the larger number of suspended motors. These simulations again confirm that hydrodynamic interactions give rise to a non-negligible flow in solution.

Note that the simulations for both values of $\langle V_0 \rangle$ are performed in identical systems for the same number of time steps. However, the error bars for $\langle V_0 \rangle$=0.63 are smaller. This is understood from the calculation of the standard deviation, $\sigma_{\langle V \rangle / \langle V_0 \rangle}$, given by [160]:

$$\sigma_{\frac{\langle V \rangle}{\langle V_0 \rangle}} = \frac{\langle V \rangle}{\langle V_0 \rangle} \sqrt{\left(\frac{\sigma_{\langle V \rangle}}{\langle V \rangle} \right)^2 + \left(\frac{\sigma_{\langle V_0 \rangle}}{\langle V_0 \rangle} \right)^2}. \tag{4.9}$$

In the above equation, $\sigma_{\langle V \rangle}$ is the measured standard deviation for the suspended motors which is $\sim$0.1 for both $\langle V_0 \rangle$ and $\sigma_{\langle V_0 \rangle}$ is the standard deviation for $\langle V_0 \rangle$. The latter is found to be 0.002 (not shown). Insertion of a larger value for $\langle V_0 \rangle$ in eq.4.9 thus improves the statistics.

Different Hydrodynamic Interaction Tensors

In the above sections hydrodynamic interactions were introduced using the Oseen tensor (see eq.2.25), a hydrodynamic interaction tensor that gives a possible solution for the flow field around spherical objects. This tensor has its limitations. Studying the effect of this choice is the topic of this section. Firstly, there is a short discussion on the different tensors, followed by a comparison of the simulation results. Note that for all hydrodynamic interaction tensors holds that $\boldsymbol{\mu}_{\mathrm{ii}}=\mu_0 \hat{\boldsymbol{I}}$, thus only the inter-organelle components $\boldsymbol{\mu}_{\mathrm{ij}}$ will be discussed.

$$\boldsymbol{\mu}_{\mathrm{ij}} = \frac{3}{4} \mu_0 \frac{a}{r_{\mathrm{ij}}} [\hat{\boldsymbol{I}} + \hat{\boldsymbol{r}}_{\mathrm{ij}} \otimes \hat{\boldsymbol{r}}_{\mathrm{ij}}]. \qquad \mathrm{i} \neq \mathrm{j} \tag{2.25}$$

As explained in chapter 2, the Oseen tensor only takes the long-range interactions between suspended objects into account and ignores the short-range interactions. As long as the organelle separation exceeds x=10A, the values are accurate [59] since long-range-interactions dominate at this length scale. At shorter separations a tensor taking short-range interactions into account, such as the Rotne-Prager tensor (see eq.4.10 [158, 159]) given below, would be more accurate.

$$\boldsymbol{\mu}_{\mathrm{ij}} = \frac{3}{4}\mu_0 \frac{a}{r_{\mathrm{ij}}} \left(\hat{\boldsymbol{I}} + \hat{\boldsymbol{r}}_{\mathrm{ij}} \otimes \hat{\boldsymbol{r}}_{\mathrm{ij}}\right) + \frac{1}{2}\mu_0 \left(\frac{a}{r_{\mathrm{ij}}}\right)^3 \left(\hat{\boldsymbol{I}} - 3\hat{\boldsymbol{r}}_{\mathrm{ij}} \otimes \hat{\boldsymbol{r}}_{\mathrm{ij}}\right), \qquad \mathrm{i} \neq \mathrm{j}. \tag{4.10}$$

One known issue of the Oseen tensor is that it has a singularity at r_{ij}=0 i.e. when motors overlap. This could result in unrealistically large velocities induced by one motor on the other. In simulations this can yield spurious effects on on velocity fluctuations [157]. To remove this singularity Brenner [157] introduced the following equation for the particle separation, $\breve{r}_{\mathrm{ij}}$, which can be used in any hydrodynamic interaction tensor:

$$\breve{r}_{\mathrm{ij}} = \sqrt{x_{\mathrm{ij}}^2 + y_{\mathrm{ij}}^2 + z_{\mathrm{ij}}^2 + 1}. \tag{4.11}$$

Finally, Allen and Tildesley [69], mention in their chapter on Brownian Dynamics that because of the long-range character of the hydrodynamic interaction tensors it is not clear if they can be used in combination with periodic boundary conditions. This includes solutions with and without Ewald summations. We will introduce a both truncated and shifted version of the Oseen tensor in which we ignore interactions beyond half the simulation box size, $r_{\mathrm{box}/2}$. The new tensor, $\boldsymbol{\mu}_{\mathrm{ij}}^{\mathrm{TS}}\left(\boldsymbol{r}_{\mathrm{ij}}\right)$ is given by:

$$\boldsymbol{\mu}_{\mathrm{ij}}^{\mathrm{TS}}\left(\boldsymbol{r}_{\mathrm{ij}}\right) = \begin{cases} \boldsymbol{\mu}_{\mathrm{ij}}\left(\boldsymbol{r}\right) - \boldsymbol{\mu}_{\mathrm{ij}}\left(\boldsymbol{r}_{\mathrm{box}/2}\right) & r_{\mathrm{ij}} \leq r_{\mathrm{box}/2}, \\ \boldsymbol{0} & r_{\mathrm{ij}} > r_{\mathrm{box}/2}. \end{cases} \tag{4.12}$$

Fig.4.9A, shows the normalised velocity data for both bound and suspended motors for different hydrodynamic interaction tensors. The data for the Oseen tensor, with or without Brenner extension, and the Rotne-Prager all collapses. This suggests that the hydrodynamic motor radius a was chosen small enough for the data presented in this chapter till now. Moreover, this justifies the choice for the computationally cheapest Oseen tensor as the data does not change by choosing a more advanced version of the tensor. The truncated and shifted potential data deviates from the other tensors as both the bound and suspended motors move at slower velocity. However, even for this tensor, hydrodynamic interactions give rise to a non-negligible flow of motors in solution, again showing the robustness of the phenomenon. The shape of the concentrations profile is independent of the hydrodynamic interactions (Fig.4.9B), thus purely an effect of the Langmuir-type interactions. Fig.4.9C, confirms that the choice of the tensor does not affect the shape of the velocity profile between the bio-filaments. In line with Fig.4.9A, the velocity of suspended motors of the truncated and shifted tensor lies below the other tensors, but still shows a non-negligible effect increase in velocity. Fig.4.9D shows the effective forces acting on bound and suspended motors. Interestingly, using the

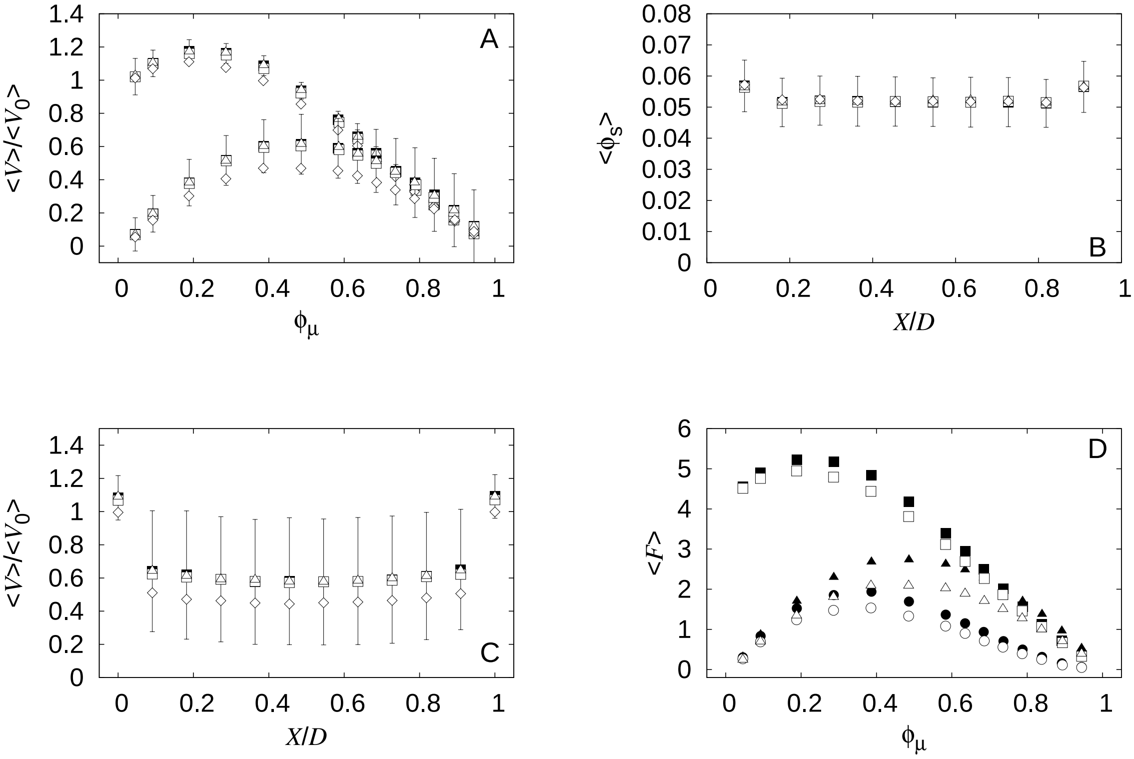

Figure 4.9: *A) The normalised velocity for different degrees of bio-filament occupation, ϕ_μ. Upper series (starting at value one) refers to bound motor velocities, lower series (starting at value zero) to average velocity of suspended motors. B) Concentration profiles for unbound motors. D is the bio-filament separation, and X the distance to the lower bio-filament (ϕ_μ=0.4). C) Normalised velocity over the distance D (ϕ_μ=0.4). For figures A-C: Filled squares - Oseen tensor (eq.2.25); Open squares - Oseen tensor with Brenner modification (eq.4.11); open triangles - Rotne-Prager tensor (eq.4.10); Open diamonds - Truncated and shifted Oseen tensor (eq.4.12). D) Effective force (in pN) acting on motors for different filament occupations. The filled data points - Oseen tensor (see Fig.4.5B), open points - truncated and shifted Oseen tensor. The squares refer to forces acting on the bound motors, the circles show the force from hydrodynamic interactions and the triangles show the data in solution. Simulation settings: F_0=1.061, μ_0=0.3769, V_0=0.4, $\langle V_0\rangle$=0.43, $N_{\mathrm{part}}\approx$1000, ϕ_{s}=0.05 and, T_{max}=7000.*

truncated and shifted tensor improves the force calculation at large bio-filament occupations. Using this tensor raises the maximum physically plausible hydrodynamic force on suspended motors from an occupation of 75% to 85%. This shows that using hydrodynamic interaction tensors with periodic boundary conditions gives rise to an enhanced hydrodynamic coupling, this effect is largest at large bio-filament occupation fractions.

Opposing Filaments

The bio-filaments in cells are not always aligned with matching polarities. In the case of rotational streaming (e.g. *Chara* or *Nitella* [6, 161]), the bio-filaments can be found having opposite polarities at the different cell boundaries. For these cells sigmoidal velocity profiles between the bio-filaments have been reported [6, 161]. To study this type of situation, our model will now be adapted by reversing the polarity of the upper bio-filament as shown in Fig.4.10.

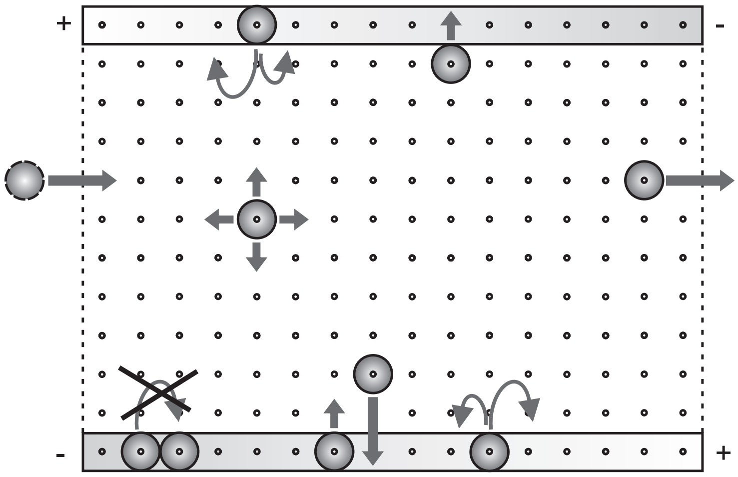

Figure 4.10: *Schematic view of the model system, i.e. a cytoplasmic strand in a plant cell. A solution is embedded between two bio-filaments and mapped on a lattice. Moreover, both bio-filaments have opposite polarities, thus the walking distance of bound motors depends on the bio-filament. Motors on the bottom bio-filament walk to the right and motors at the upper bio-filament move in the opposite direction. All possible moves of the motor-cargo complexes are shown. Excluded volume and the processivity of the motors are accounted for. To mimic the dynamics of a infinite system, periodic boundary conditions are used in axial direction.*

The results in Fig.4.11A show that the absolute values of the normalised velocities on both bio-filaments are equal as expected. Moreover, the opposing microtubules influence each others bound motor velocities via hydrodynamic momentum transfer. This results in motors on one bio-filament slowing down the motors on the opposite one and vice versa. Contrary to the parallel bio-filaments with equal polarity, the bound velocity does not surpass the single motor velocity at any value of ϕ_μ. However, comparison with the theoretical ASEP velocity (line in figure, see eq.A.2 in appendix A) shows that there still is a non-negligible increased motor velocity caused via hydrodynamic interactions. The maximum velocity difference, ΔV=0.06, between the measured and ASEP velocity is found at ϕ_μ=0.4 and corresponds to a hydrodynamic force of 0.6 pN.

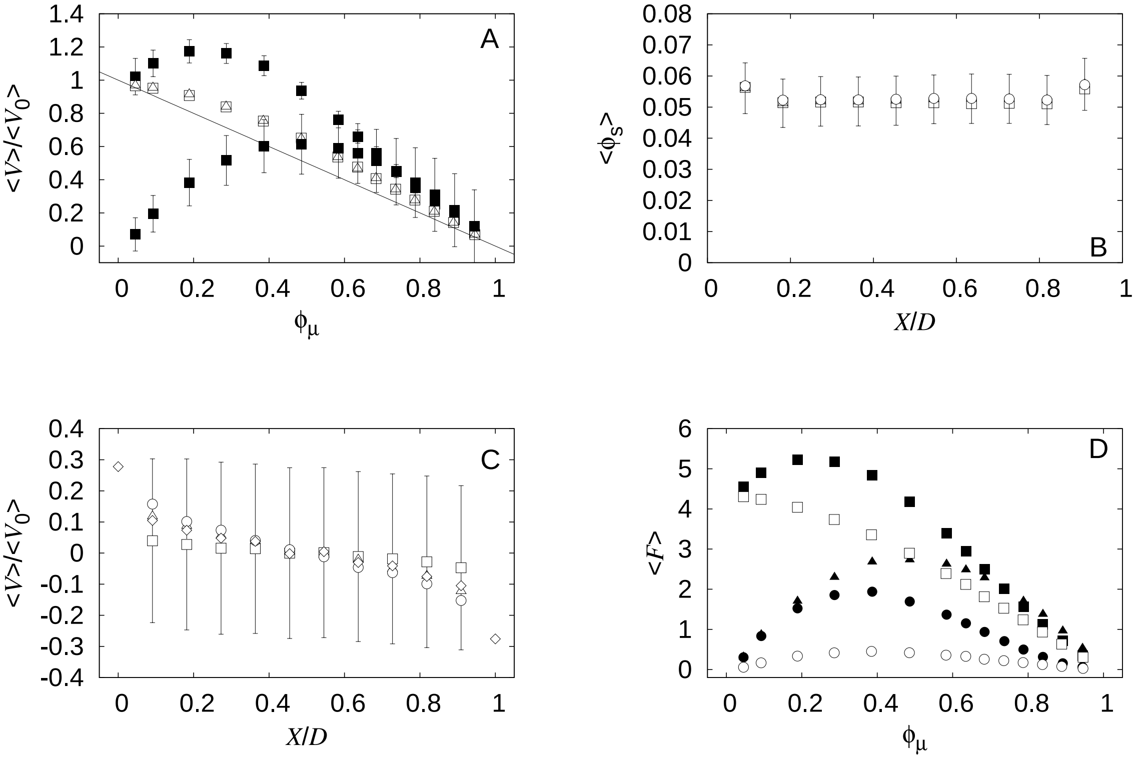

Figure 4.11: *A) The (absolute) normalised velocity for different degrees of bio-filament occupation, ϕ_μ. The closed squares represent the reference system with parallel bio-filaments with equal polarities. The open squares and triangles refer to a system with opposing polarities ($\langle V_{0,\mu1}\rangle$=0.43 and $\langle V_{0,\mu2}\rangle$=-0.43). The line shows the theoretical velocity (ASEP) in the absence of hydrodynamic interactions. B) Concentration profiles for unbound motors. D is the bio-filament separation, and X the distance to the lower bio-filament. C) Normalised velocity profile over the distance D. Figures B-D: Open squares - ϕ_μ=0.2; Open triangles - ϕ_μ=0.4; Open circles - ϕ_μ=0.6; Open diamonds - ϕ_μ=0.8. D) Effective force (in pN) acting on motors for different filament occupations. The open and closed symbols represent data for opposing and parallel bio-filaments respectively. Squares - bound motor-forces; circles - hydrodynamic force on bound motors; triangles - suspended motors. The simulation settings for all figures were: μ_0=0.3769, $F_{0,\mu1}$=1.061, $F_{0,\mu2}$=-1.061, $V_{0,\mu1}$=0.4, $V_{0,\mu2}$=-0.4, $N_{\mathrm{part}}\approx$1000, ϕ_{s}=0.05, and, $T_{\max}$=7000.*

Consistently with earlier findings, the hydrodynamic interactions have no effect on the shape nor the magnitude of the concentration profile between the bio-filaments (Fig.4.11B). The velocity profile shown in Fig.4.11C, presents a new situation. The suspended motors move in the direction corresponding to the polarity of the nearest bio-filament. The closer to the bio-filament the faster the motors. The motor velocity drops with the distance away from the bio-filament until a velocity of zero is reached at the centre of the system. Here the hydrodynamic drag forces are balanced. Further away, the velocity reverses direction creating an inverted mirror image. The shape of the full profile differs from the sigmoidal velocity profiles presented in literature [6, 161]. The aforementioned profiles show a small drop in velocity near the bio-filament followed by a large drop near the centre of the system followed by inversion of the velocity. There are two differences between both measurements. Unlike the data from literature, we present the suspended motor velocity and not the fluid velocity. Moreover, we assumed the cytosol to be a Newtonian fluid which is an approximation. Fig.4.11D shows that the hydrodynamic interactions acting upon bound motors gives rise to a small but relevant hydrodynamic forces.

Crossing Gaps In The Cytoskeletal Tracks

In the introduction of this chapter axoplasmic streaming was mentioned. This is directed transport of organelles and molecules along nerve cell axons [2] and can take place over long distances (e.g. up to several meters in the Giraffe [153]) with respect to the cargo size. For axoplasmic streaming these neurons rely on active motor transport which is more efficient than passive diffusion[*], for transport of organelles. The molecular motors walk along the axonal cytoskeleton that lines the inside of the axon in axial direction. For the stability of the axon as well as for enabling active transport it is important for the cytoskeleton to span the whole length of the axon. However, what happens to the axonal streaming if, due to decease or trauma, the cytoskeletal tracks are interrupted? To study this situation, the following simulation model, shown in Fig.4.12, is used.

In the model, there is a gap in both of the parallel bio-filaments where the motor's cytoskeleton track is missing. Walking motors that reach the end of the track will leave the cytoskeleton with unit probability and diffuse away from the filament. Similar to the original model (see Fig.4.4), the motors can hydrolyse ATP only when attached to the cytoskeleton. Thus, in the gap, there is no net force generated by the motors. Suspended motors along the cell wall or in the bulk can attach to the cytoskeleton with unit probability taking excluded volume into account. The gap is chosen to be large in comparison to the organelle size (20l or 60l wide, where l is the lattice spacing) but short with respect to the length, L, of the system (L=750l). The width of the system is 12l.

As the system makes use of periodic boundary conditions in axial direction, the dynamics of an infinitely large system, with a gap every given number of lattice nodes, is studied. The system was initialised from a uniformly distributed configuration[†] for a period of 100,000 simulation steps in the absence of hydrodynamic interactions. From

---

[*] See table 2.3 in chapter 2.

[†] The final configuration from an earlier simulation with ϕ_s=0.05 and ϕ_μ=0.4 (no gap).

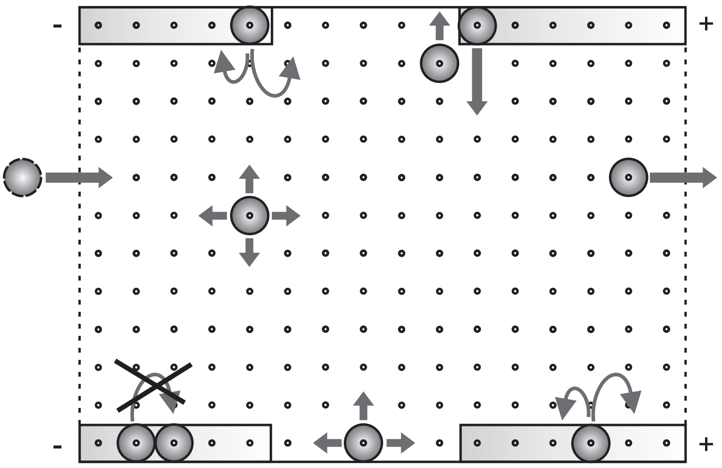

Figure 4.12: *Schematic view of the model system, i.e. an axon of a neuron. A solution is embedded between two bio-filaments and mapped on a lattice. The bio-filaments have a given polarity which determines the walking direction of the motor-cargo complexes. There is a gap in both bio-filaments where the motor-cargo complexes diffuse freely along the cell wall without directional preference. All possible moves of the motor-cargo complexes are shown. Excluded volume and the processivity of the motors are accounted for. To mimic the dynamics of a infinite system, periodic boundary conditions are used in axial direction.*

this starting configuration, simulations were performed for 25,000 time steps, a period long enough for the system to reach a steady-state, with or without hydrodynamic interactions. In the previous sections, the axial velocity and radial concentration profiles did not change in axial direction i.e. in the direction of the active transport. As now there is a gap in the filaments, these values will vary depending on the axial position in the system. To show the local concentrations and velocities, the system has been divided into sections (bins). In each bin, the motor concentration and velocities are measured for each row of lattice nodes i.e. on a bio-filament or in any row parallel to it and subsequently the average values are taken. Since the system is mirrored in the radial direction the statistics are improved by taking the average value (concentration or velocity) over a row of nodes and its mirror image. For example, the average values were taken for the row of lattice nodes directly below the upper filament and the row directly above the lower filament. The bins are chosen such that the spatial resolution can qualitatively show the local dynamics. For this purpose the system has been divided into 10 bins, 8 of equal length to describe the filaments (+solution) and 2 describing the gap.

In Fig.4.13A is shown that, in the absence of hydrodynamic interactions, the gap causes a traffic jam along the filament. This is as expected since motors are actively

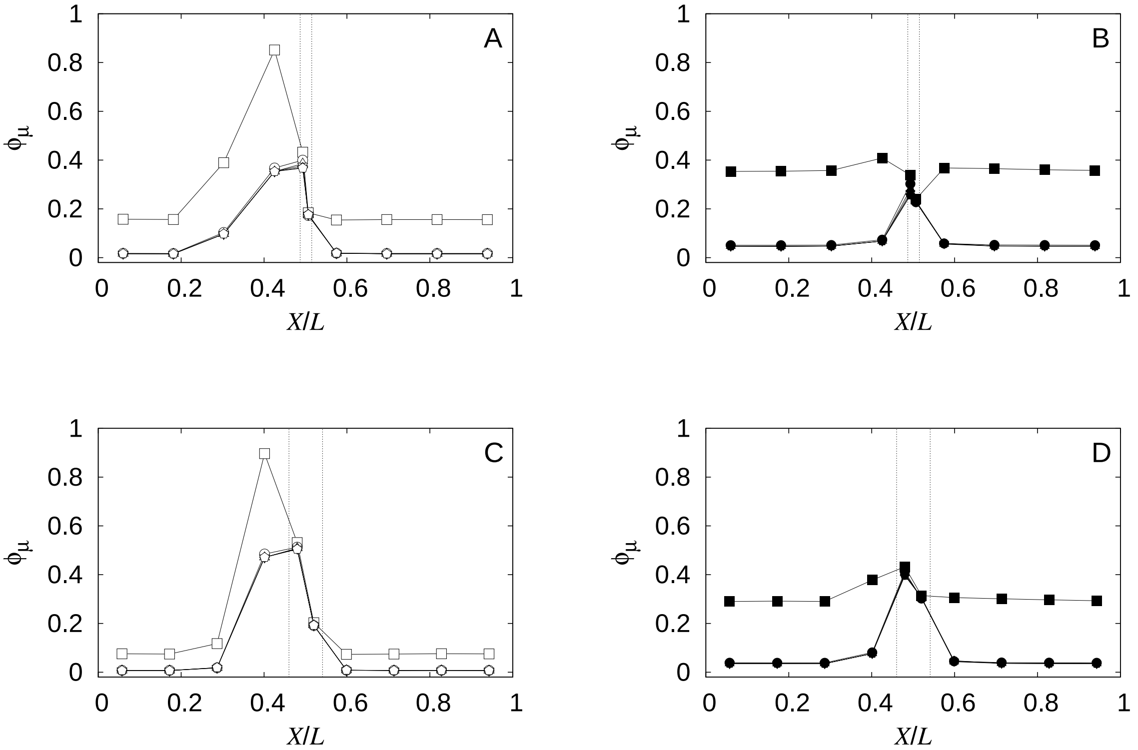

Figure 4.13: *A) and B) Concentration profiles per row of lattice nodes. L is the length of the system, W the width, and X the horizontal coordinate. The system is divided into bins for which the average concentrations are shown. The gap size is 20 lattice nodes. Filled symbols with hydrodynamic interactions (HI), Open symbols no HI; Squares - Filament; Circles - 1st row of lattice nodes neighbouring the biofilament; Triangles - 2nd row; Inverted triangles - 3rd; Diamonds - 4th; Pentagon - 5th i.e. centre row. The vertical lines represent the beginning and end of the gap respectively. C) and D) Idem for a gap of 60 lattice nodes. The simulation settings:* L*=750*l*,* W*=12*l*,* μ_0*=0.3769,* F_0*=1.061,* V_0*=0.4,* $N_{\rm part}\approx$*1000, and,* $T_{\rm max}$*=25,000.*

transported towards the gap and can leave only by diffusion, a much slower process*. In addition, the motor concentration in solution strongly increases, before and at the begin of, the gap after which the concentration decreases again. At a sufficient distance from the gap (before or after) the system reaches a constant filament and solution concentration as observed in the absence of the gap (See e.g. Fig.4.7A). The latter steady-state is reached by the Langmuir Kinetics in the system (see eq.4.5 and 4.6). In-

---

*Similarly, the combination of active transport towards a wall and diffusion away from it causes a traffic jam and motor accumulation in solution (Fig.3.5C).

creasing the size of the gap further increases the accumulation of organelles at the gap (Fig.4.13C) and thereby further depletes the motor concentration in the rest of the system. When hydrodynamic interactions are included (Fig.4.13B) a small concentration increase is observed in the gap, albeit much smaller than without hydrodynamic interactions. The momentum transfer, via the fluid, helps the motors to cross the gap, thus preventing a large local organelle accumulation. In addition, the traffic jam around the gap is much smaller. Most importantly, the organelle transport is not impaired, as the average motor concentration over the whole system is close to that observed in a reference system without a gap (see Fig.4.7A, ϕ_s=0.05 and ϕ_μ=0.4). Increasing the gap size (Fig.4.13D) enhances the organelle accumulation around the gap but does not impair organelle transport.

The normalised velocity profile in the absence of hydrodynamic interactions (see Fig.4.14A) clearly shows the effect of the traffic jam before the gap. Here the velocity decreases when the bound organelle concentration near the gap increases. In solution, the average velocity is zero as there are no external forces acting upon the organelles. However, in the gap, there is a small positive motor velocity. This is a result from the net motor flux that compensates for the concentration gradient. When the gap is increased (Fig.4.14C), the average bound organelle velocity increases. This can be understood from the larger accumulation of organelles at the gap, that effectively yields a smaller bound organelle concentration (Fig.4.13C). When hydrodynamic effects are included, the bound motor-organelle velocity is larger than for a single motor. Moreover, in solution the organelles move at a non-negligible velocity. The found velocities are in line with the reference system without gap (Fig.4.5). In the gap the velocity of all organelles decreases but stays significant. The velocity of the motors at the cell wall drops down to a velocity slightly above the one measured in the bulk. Increasing the size of the gap (Fig.4.14D) shows a slightly higher velocity at the filament and a smaller value in solution.

Discussion

We have shown that long range collective hydrodynamic interactions lead to a substantial increase in the effective velocity of motors attached to a filament. Moreover, their motion leads also to a net transport of the nearby unbound particles. This mechanism is not captured by models that consider only the activity and steric interactions of motors attached to bio-filaments. Such an additional transport mechanism may be numerically as relevant as the mass transport obtained by direct motion of attached motors.

The additive hydrodynamic force, as induced by the processivity of the filament, might not be large compared with the driving force which generates the motion of the attached motors but the cumulative effect can give rise to a net significant mass trans-

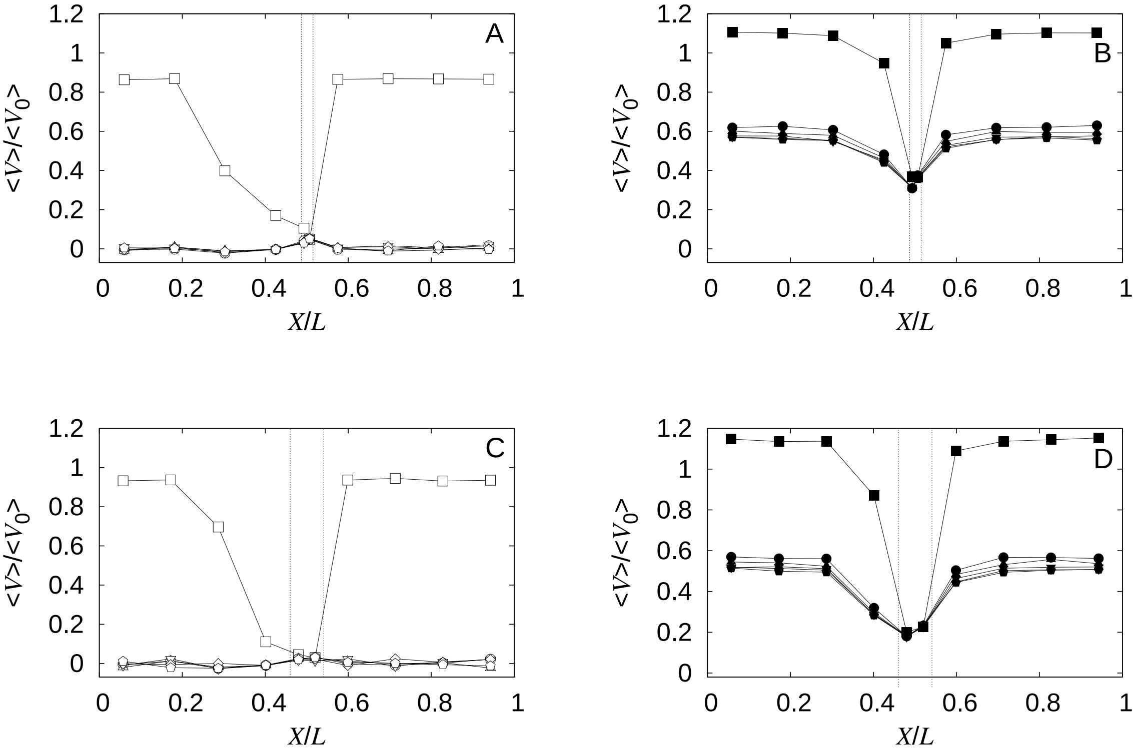

Figure 4.14: *A) and B) The normalised velocity per row of lattice nodes. L is the length of the system, W the width, and X the horizontal coordinate. The system is divided into bins for which the average velocities are shown. The gap size is 20 lattice nodes. Filled symbols with hydrodynamic interactions (HI), Open symbols no HI; Squares - Filament; Circles - 1st row of lattice nodes neighbouring the bio-filament; Triangles - 2nd row; Inverted triangles - 3rd; Diamonds - 4th; Pentagon - 5th i.e. centre row. The vertical lines represent the beginning and end of the gap respectively. C) and D) Idem for a gap of 60 lattice nodes. The simulation settings:* L=750l, W=12l, μ_0=0.3769, F_0=1.061, V_0=0.4, $N_{\text{part}}\approx$1000, *and,* $T_{\max}$=25,000.

port of the system. Obviously, such a constructive mechanism will be more prominent the more ordered the environment. However, the mechanism is maintained even when bio-filaments of opposite polarities are present. Moreover, when there are gaps in the cytoskeletal tracks, the hydrodynamic interactions help organelles cross the gap and, in addition, maintain a homogeneous organelle concentration in the system.

In this sense, such a mechanism can be envisioned to be more important in situations as found in neurons or in cytoplasmic strands in plant cells. The outcome of our simulations suggests that this mechanism is indeed a plausible explanation for how cytoplasmic and axoplasmic streaming really takes place.

Chapter 5

Hydrodynamic Flow in the Cytoplasm of Plant Cells

In this thesis we test our hypothesis for explaining how transport takes place in cells by means of computer simulations. Our simulations show that the momentum transfer via hydrodynamic interactions between the active bound organelles and the suspended objects gives rise to a non-negligible flow in solution. In order to test these results in a real biological system Agnieszka Esseling-Ozdoba performed experiments in the group of Anne Mie C. Emons (Department of Plant sciences) at Wageningen Universiteit. This work was a close collaboration between both our groups and was published [150, 162]. The text below is an adapted version of the publication. Copyright 2013 Wiley. Used with permission from Esseling-Ozdoba et al., Hydrodynamic flow in the cytoplasm of plant cells, *Journal of Microscopy, Blackwell Publishing Ltd*, 2008, 231, 274-283 [150]. The original section on materials and methods can be found in appendix C.

Introduction

The cytoplasm of eukaryotic cells consists of all cell material between the nucleus and the plasma membrane and contains membrane-bounded structures, organelles, which are embedded in the cytosol consisting of water, salts and organic molecules, including sugars, proteins, and many enzymes that catalyse reactions. The cytoskeleton of microtubules and actin filaments in the cytosol structures the cell by localising and transporting the organelles bound to these tubules and filaments. The plasma membrane, enveloping the cytoplasm physically, separates the cell content from the extracellular environment, which in plant cells is the cell wall. The latter consists of cellulose micro-fibrils embedded in a matrix of polysaccharides, glycoproteins and phenolics. The largest organelle in the plant cell is the vacuole [163–165], which functions as waste managing factory and also to maintain the hydrostatic pressure in the cell. Cytoplasmic strands of cytoplasm (also called transvacuolar strands) that are bounded by the vacuolar membrane traverse the central vacuole in mature plant cells. They connect the peripheral cytoplasm to the cytoplasm that surrounds the cell nucleus [164, 166]. In Fig.5.1-Left, a stamen hair cell of *Tradescantia virginiana* is shown and the main components of the cell are highlighted.

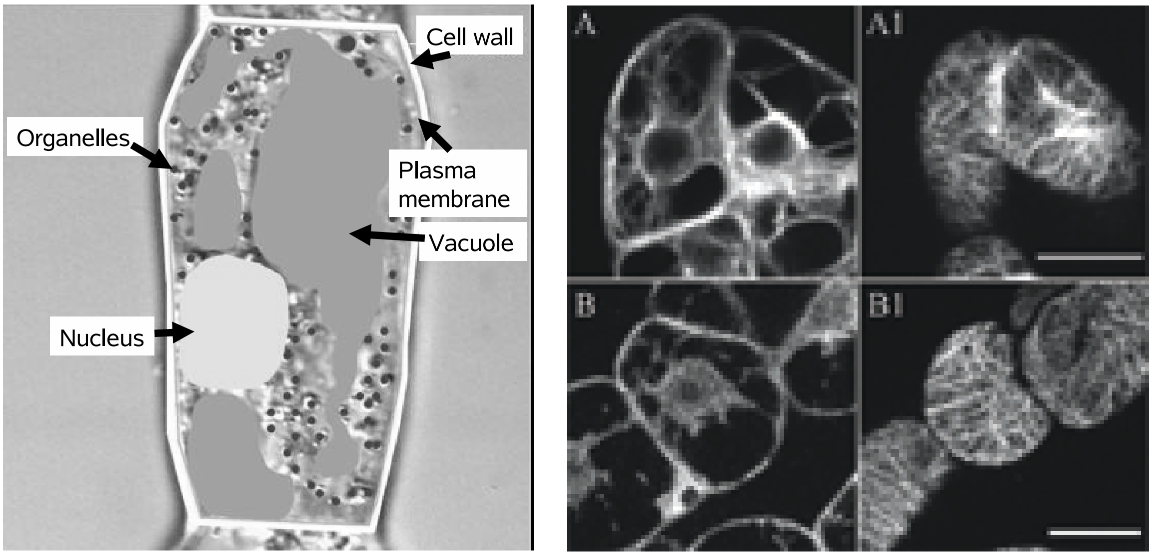

Figure 5.1: *Left - Cytoplasmic streaming in Tradescantia virginiana. Right - Confocal laser scanning microscope (CLSM) images of young tobacco BY-2 suspension cells transformed with GFP:FABD (fimbrin actin-binding domain) to visualise actin filaments (A and A1) and GFP:TUA6 (α-tubulin) (B and B1) to visualise microtubules. Actin filaments (A) but not microtubules (B) are present in the cytoplasmic strands. Both microtubules and actin filaments are present in the cell cortex (Figures A1 and B1). The fluorescence in cytoplasmic strands in B is possibly free GFP- tubulin, bar =* $20\ \mu\mathrm{m}$.

Under a differential interference contrast (DIC) microscope, the rapid transport of organelles in the cytoplasmic strands can be observed. This rapid transport is called cytoplasmic streaming (e.g. pollen tubes: [167]; root hairs: [168]; review: [169]). The organelle movement is driven by the molecular myosin motors that walk along actin filaments [5, 170–173]. In interphase plant cells, microtubules are not present in the cytoplasmic strands (this chapter) but radiate only from the nucleus during the transitions from interphase into mitosis [163, 174, 175], and just after cytokinesis [176]. In cytoplasmic strands, actin filaments are mainly present in bundles [169, 177–179] and can be considered to be cellular highways, on which organelle-associated myosin motors move their cargo [5, 48, 170, 171, 180]. The energy necessary for the movement of the myosin motors is generated by hydrolysis of ATP. In vitro, the maximum measured speed of the higher plant myosin XI is $7\ \mu\mathrm{m/s}$ [30]. Organelle movement in different plant cells can reach various velocities, see table 5.1.

The bulk of soluble molecules such as metabolites do not move with motor proteins in the cytoplasm. In a system in which particles, organelles here, move actively in-

Cell type	**Plant**	**Speed** μm/s	**Reference**
Pollen tubes	*Nicotiana tabacum*, Arabidopsis	± 2	[181,182]
Root hairs	*Medicago truncatula*	8-14*	[168]
	Equisetum hyemale	3.5-7*	[177]
Hypocotyl	Arabidopsis	4.8	[183]
Stamen hairs	*Tradescantia virginiana*	1.4-5*	**

Table 5.1: *Motor velocities in different plant cells. *Organelle velocity dependent on the developmental stage of the cell. **Own observations, unpublished.*

side an aqueous environment with suspended molecules, it is expected that the actively moving particles induce a flow in the surrounding medium, dragging along other particles and molecules. For this intra-cellular movement the term hydrodynamic flow may be used. In general, the term hydrodynamic flow is used when a fluid stream exerts a drag force on any obstacle placed in its wake, and the same force arises if the obstacle moves and the fluid is stationary [184].

A recent simulation study [149] showed that active transport of organelles gives rise to a hydrodynamic flow in the cytosol, which may be important for the fast distribution of proteins and nutrients in large cells. Here we show for the first time that actively transported organelles produce hydrodynamic flow in plant cells, which significantly contributes to the movement of the molecules in the cytosol. We show that in the cytoplasm of tobacco BY-2 suspension cells, constitutively expressing cytoplasmic GFP, free GFP molecules move faster in cells with active organelle transport than in cells where this transport has been inhibited. Furthermore, we show that the direction of the GFP movement is the same as that of the organelle movement. We conclude that hydrodynamic flow is a faster way than diffusion in distributing molecules inside plant cells.

Results

Choice of inhibitors of organelle movement

Our aim was to study whether actively moving organelles influence the movement of molecules in the cytosol. The cells of choice were tobacco BY-2 suspension cells expressing cytoplasmic GFP. In the cytoplasmic strands of those cells, actin filaments are present (Fig.5.1A), but microtubules are not (Fig.5.1B) showing that actin filaments are the highways for organelle movement in plant cells. Actin depolymerising agents stop streaming while microtubule depolymerising drugs do not influence organelle movement (data not shown). For this study we used Fluorescence Recovery After Photobleaching (FRAP). In such experiments a cytoplasmic area is photobleached and the time of re-appearance of the bleached fluorescence molecule is measured. FRAP was measured in $2.2\ \mu\mathrm{m}\times 2.2\ \mu\mathrm{m}$ areas of cytoplasmic strands. Fig.5.2A shows the recovery of GFP fluorescence in a bleached area of a cytoplasmic strand of a young BY-2 tobacco suspension cell.

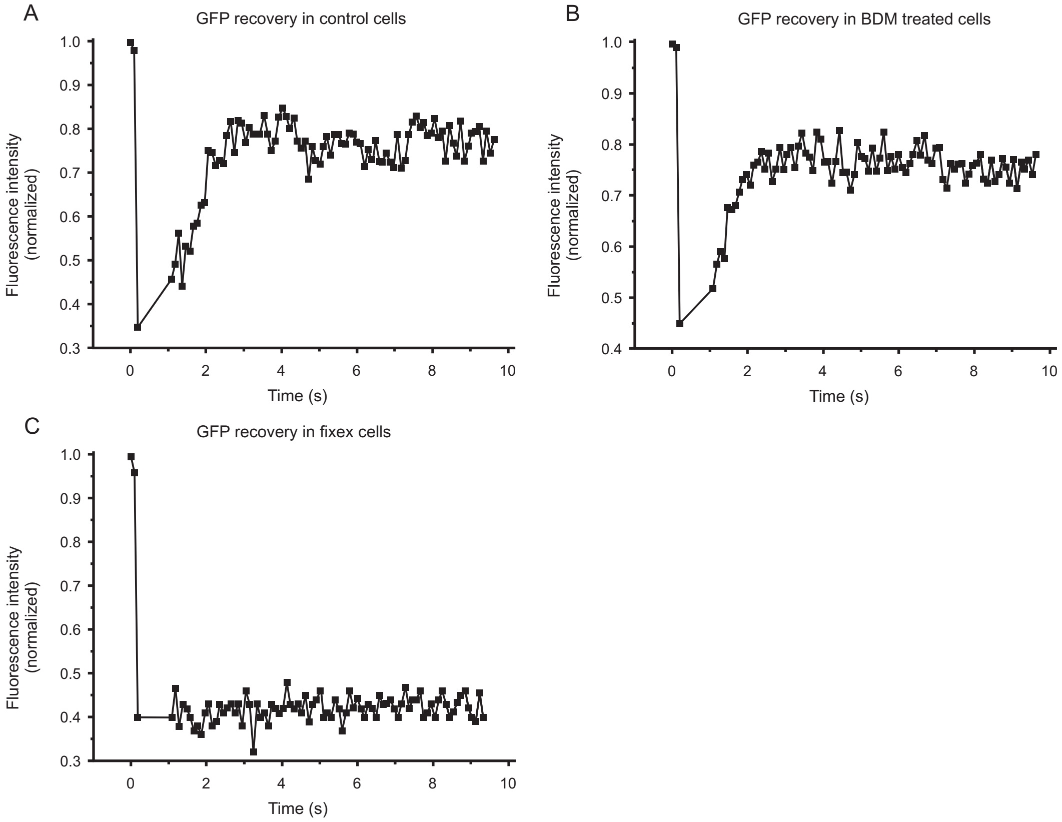

Figure 5.2: *Recovery of GFP fluorescence after photobleaching in untreated control-cells (A), cells treated 50 mM BDM (B) and fixative: 2% paraformaldehyde (PA) and 0.2% glutaraldehyde (GA) (C). In cells treated with BDM fluorescence recovery of GFP was observed. In cells treated with fixatives no fluorescence recovery was observed. The recovery was measured in young BY-2 suspension cells.*

We used 2,3 butanedione monoxime (BDM) as an inhibitor of active organelle transport in the cytoplasm of BY-2 suspension cells expressing cytoplasmic GFP. Our purpose was to inhibit organelle movement, but not the Brownian movement of GFP. BDM is a general myosin ATPase inhibitor [185–187]. BDM at a concentration of 50 mM stopped organelle transport, but recovery of GFP occurred (Fig.5.2B), similarly like in the control cells (Fig.5.2A). The recovery of GFP ceases in cells chemically fixed with 2% paraformaldehyde (PA) and 0.2% glutaraldehyde (GA). In those cells no GFP recovery occurred during a typical FRAP experiment (Fig.5.2C).

Free GFP molecules move faster in cells with active transport than in those treated with BDM

To test whether the moving organelles induce hydrodynamic flow in the cytoplasm, we used cells with active transport and compared the GFP recovery after photobleaching in control cells with cells in which this movement is inhibited with BDM. With this, we test if hydrodynamic flow is produced by moving organelles and to what extent this contributes to the movement of molecules in the cytoplasm. If our hypothesis is correct, then the recovery of GFP molecules in the cytoplasm of control cells should be faster than in the cells in which this movement is inhibited. Instead of using young small cells that hardly have visible organelle movement (Fig.5.3A) and consequently hardly any hydrodynamic flow, we used large elongated cells (Fig.5.3B) from 10-day-old subcultures of tobacco BY-2 suspension cells, expressing cytoplasmic GFP. Like in young cells from 3 to 4-day-old subcultures (Fig.5.1A), actin filaments but not microtubules are present in the cytoplasmic strands (Fig.5.4) and are responsible for active movement of organelles, since treatment with the actin depolymerising drug latrunculin stops cytoplasmic streaming (data not shown; [172, 188, 189]). In comparison with young small cells, 10-day-old cells have visible, vigorous cytoplasmic streaming ($0.78 \pm 0.17\ \mu\mathrm{m/s}$). We measured the half time of GFP recovery after photobleaching in a cytoplasmic strand region of $2.2\ \mu\mathrm{m} \times 2.2\ \mu\mathrm{m}$. GFP recovers faster (within 0.31 ± 0.07 s) in untreated cells with active organelle transport, than in cells treated with 50 mM BDM (within 0.48 ± 0.12 s) (Fig.5.5). This shows that actively transported organelles contribute significantly to the movement of GFP in the cytoplasm of BY-2 cells. In theory, one would expect to see movement of the bleached area, since omnidirectional diffusion will be superimposed on the hydrodynamic flow, resulting in a distorted diffusion pattern. However, the speed of recovery, combined with the theoretical unevenness of the speed distribution of flow, being faster nearer the actin filament bundles than further away from them, is such that this cannot be observed. From our experiments we conclude that organelle movement causes a hydrodynamic flow that contributes significantly to the movement of free GFP in the cytoplasm.

Hydrodynamic flow is higher in cells in which the velocity of organelle movement is faster

If motor-driven organelle movement causes the hydrodynamic flow of cytoplasmic molecules, then the speed of GFP movement in the cytoplasm should positively relate to the speed of organelle movement. To show this, we measured the GFP recovery after photobleaching in cells with different velocities of organelle movement (Fig.5.6). In cells in which organelles moved with an average velocity of $0.21 \pm 0.02\ \mu\mathrm{m/s}$, the recovery of GFP fluorescence took 0.73 ± 0.19 s, which was slower than in cells hav-

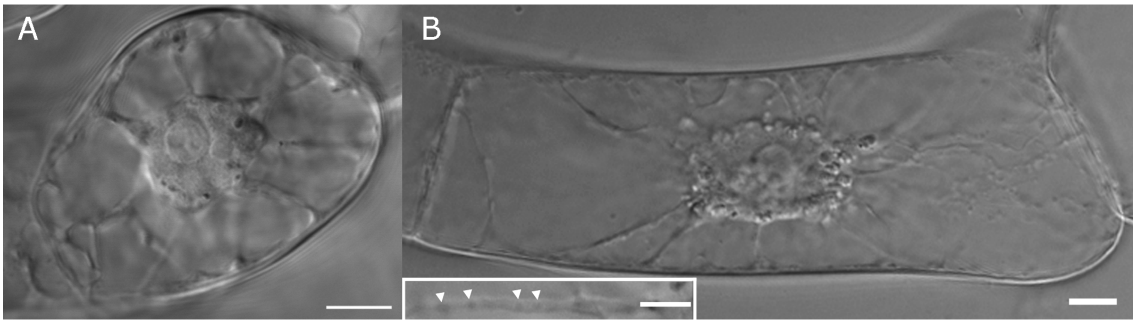

Figure 5.3: *BY-2 cells from a suspension culture: A. Typical cell from a 3 to 4-day-old culture, B. Typical cell from a 10-day-old culture. The cells in a 10-day-old culture show vigorous cytoplasmic streaming with easily visible moving organelles. Insert in B shows a cytoplasmic strand with organelles indicated by arrowheads. Bars in A and B correspond to 10* μm *and in the insert to 5* μm.

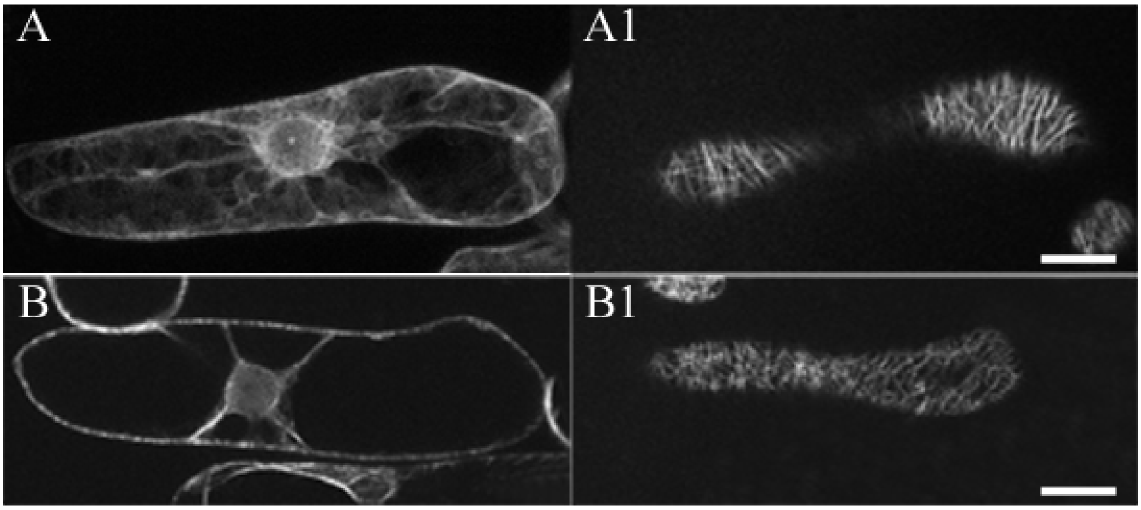

Figure 5.4: *CLSM images of 10-day old tobacco BY-2 suspension cells labelled with GFP:FABD (fimbrin actin-binding domain) to visualise actin filaments (A) and GFP:TUA6 (α-tubulin) to visualise microtubules (B). Actin filaments (A) but not microtubules (B) are present in the cytoplasmic strands; fluorescence in the cytoplasmic strands in B is due to free GFP-tubulin. Bar = 10* μm. *A1 and B1 are images of cell cortex.*

ing faster organelle movement of 0.75 ± 0.10 μm/s. In those cells, GFP recovery was 0.14 ± 0.04 s. This shows that the fluorescence recovery of GFP increases with the increasing velocity of organelles in the cytoplasm, and confirms that organelle transport induced hydrodynamic flow occurs in plant cells.

With FRAP we measured that GFP recovery, in a 10-day-old BY-2 cell, in an area of $2.2\ \mu\text{m}\times 2.2\ \mu\text{m}$, is on average 0.31 s without BDM and on average 0.48 s with BDM (Fig.5.5). If we consider the half time of GFP recovery as a time that GFP moves trough

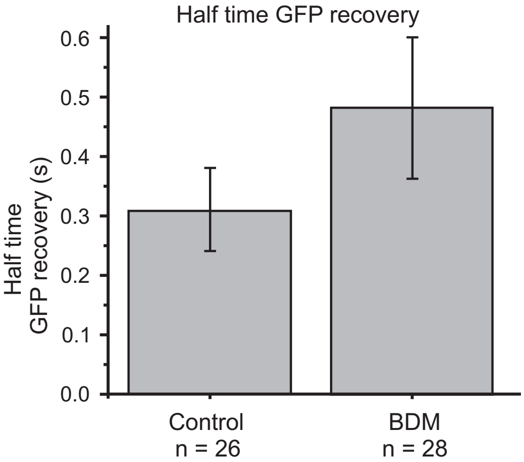

Figure 5.5: *Recovery of cytoplasmic GFP after photobleaching in control BY-2 cells and cells treated with 50 mM BDM. GFP recovered faster in control cells with active organelle transport than in cells in which this transport was inhibited with the myosin inhibitor BDM. This shows that organelle movement causes movement of GFP in the cytoplasm. For FRAP experiments, we used large elongated cells from a 10-day-old culture. Half time of GFP recovery after photobleaching is shown in a region of* $2.2\ \mu\mathrm{m}\times2.2\ \mu\mathrm{m}$*, data shown with SD.*

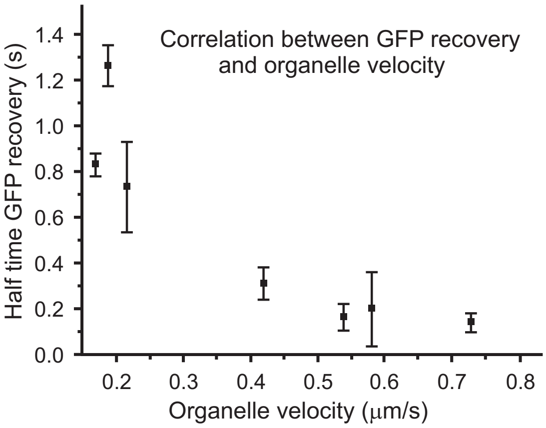

Figure 5.6: *Correlation between GFP fluorescence recovery after photobleaching and the velocity of organelles in the cytoplasm of BY-2 suspension cells. GFP recovery after photobleaching is faster in cells with faster organelle movement. Half time of GFP recovery is shown, measured in regions of* $2.2\mu\mathrm{m}\times2.2\ \mu\mathrm{m}$*, data presented from 8-10 measurements and shown with SD.*

a distance of $2.2\ \mu\mathrm{m}$, then we could calculate that GFP needs 16.9 s without BDM (with speeding up by organelles) and 26.2 s with BDM (without speeding up by organelles) to travel a distance of $120\ \mu\mathrm{m}$, which is on average a length of 10-day-old BY-2 cells. For this calculation, we also considered only one cytoplasmic strand that connects two ends of a cell. In young BY-2 cells, GFP recovery did not differ in cells treated or not treated with BDM. Without BDM, half time of GFP-recovery was on average 0.51 s and with BDM 0.56 s. Therefore we exclude that the difference in GFP mobility between BDM-treated and control 10-day-old cells was caused by a change in cytoplasmic viscosity. Taking into consideration that the length of young cells is $40\ \mu\text{m}$, GFP needs 11.8 s without BDM and 12.7 s with BDM to travel from one side of the cell to the other. We conclude that in large cells organelle movement is faster than in a small cells and that it is responsible for an efficient distribution of GFP molecules.

Direction of GFP movement in a cytoplasmic strand is the same as that of moving organelles

If moving organelles cause hydrodynamic flow of molecules, then the direction of flow should be the same as that of the organelle transport. To check this, GFP was photobleached in a region of $2.2\ \mu\text{m}\times 2.2\ \mu\text{m}$ and its fluorescence recovery was followed in time. After photobleaching we checked the direction in which organelles move in the strand. We observed that after photobleaching GFP moves in the direction of the moving organelles (N = 4) (Fig.5.7). This confirms that hydrodynamic flow occurs in plant cells with moving organelles, which drag molecules, in this case GFP, in their wake, as theoretically predicted [149].

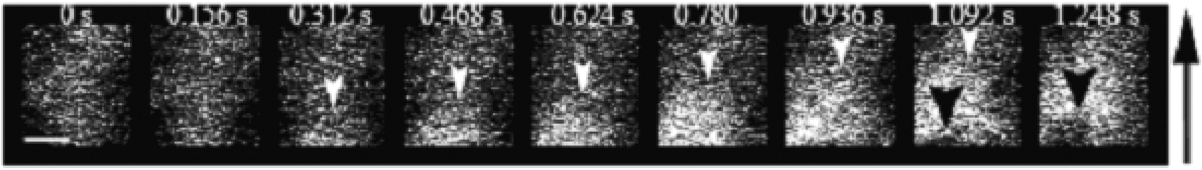

Figure 5.7: *After photobleaching, cytoplasmic GFP (white arrowheads) moved in the same direction (black arrow) as organelles (black arrowheads). GFP is visible as fluorescent speckles and an organelle as a black spot of about 1 m. For this experiment we used 10-day-old elongated cells with an average organelle velocity of 0.78* $\mu\text{m/s}$ ($\pm$ 0.17)*; time is indicated in seconds after photobleaching; bar = 1* μm.

Synthetic lipid and stealth vesicles move in cytoplasmic strands

To test if hydrodynamic flow could contribute to the movement of larger structures such as vesicles we injected synthetic lipid vesicles of size of 80 nm in diameter into *Tradescantia virginiana* stamen hair cells and observed if they moved inside the cytoplasm. The vesicles were made only of phospholipids without any proteins and their membrane contained 98% of 1,2-Dioleoyl-sn-Glycero-3-[Phospho-rac-(1-glycerol)] (DOPG) and 2% of fluorescent phosphocholine Bodipy FC12-HPC. Injected vesicles distributed in the cytoplasm of the whole cell within 10-15 min after the injection (Fig.5.8A). This result would suggest that these vesicles moved by hydrodynamic flow produced by moving organelles in the cytoplasm. We could not exclude that vesicles were coated with cytoplasmic motor proteins upon the injection and moved along the actin cytoskeleton. Therefore we injected so called stealth vesicles to which proteins cannot be attached. Stealth vesicles are phospholipid vesicles with addition of PEG (polyethylene glycol) phospholipids. The presence of PEG phospholipids prevents the attachment of proteins to the surface of vesicles. Stealth vesicles are often used in drugs therapy to prevent the attachment of proteins and lysis of vesicles that carry the drugs [190]. The concentration of PEG phospholipids used in those studies was 5-10%. The concentrations of PEG phospholipids that we used to make stealth vesicles varied from 2% up to 30% in combination with DOPG. All injected stealth vesicles distributed in the cytoplasm (Fig.5.8B) similar to DOPG vesicles without PEG and moved in the cytoplasm but slower (0.8 ± 0.13 μm/s than 1-2 microns organelles (1.4 ± 0.25 μm/s, Fig.5.8C). The fast distribution of stealth vesicles and their movement in the cytoplasm could be an indication that structures larger than molecules and possibly organelles move by hydrodynamic flow in the cytoplasm of plant cells.

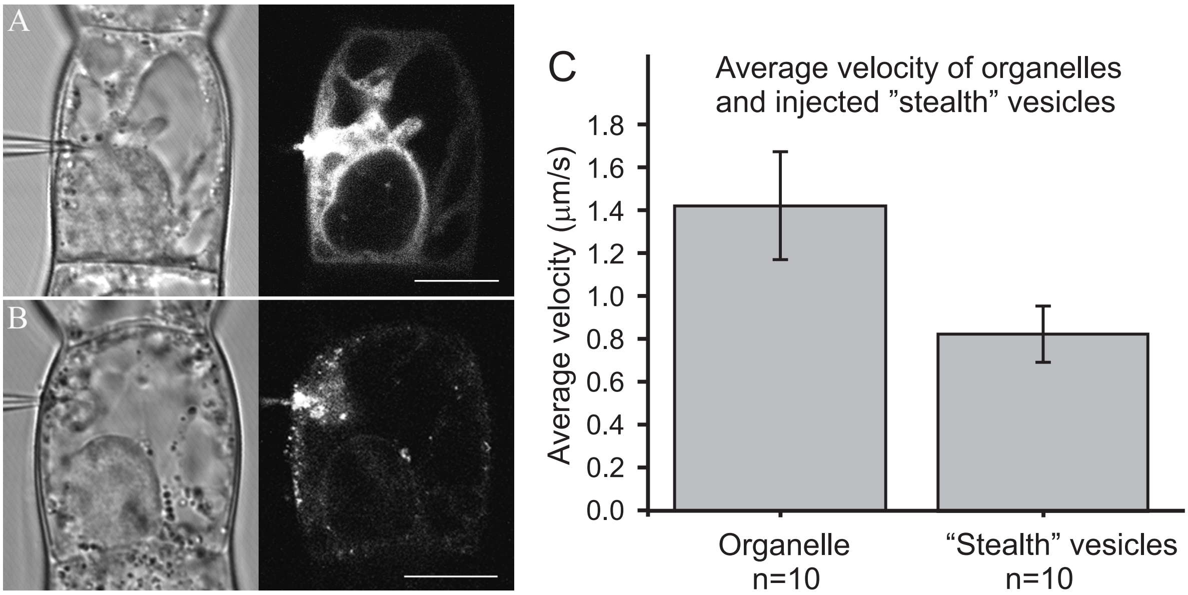

Figure 5.8: *Synthetic lipid (DOPG) vesicles (A) and stealth vesicles (B) of 80 nm in diameter distribute in the cytoplasm of T. virginiana stamen hair cells after injection. Stealth vesicles moved slower than cell organelles of 1-2* μm *in diameter (C). Stealth vesicles were made of 15 % of PEG phospholipids, 83 % of DOPG and 2% of Bodipy FC12-HPC. Images were taken 15 minutes after injection, bar = 10* μm.

Discussion

Transport in cytoplasmic strands

A major characteristic of mature plant cells is that they have large vacuoles that expand considerably during cell elongation and together become one central vacuole that takes up most of the cell volume. The vacuole confines the cytoplasm to a thin layer in the periphery of the cell and an area around the nucleus. The cytoplasm of these two regions is connected to each other by a few thin tunnels of cytoplasm: the cytoplasmic strands, also called transvacuolar strands [165, 166]. These cytoplasmic strands are essential transport routes for the distribution of organelles and metabolites [169,172]. The mechanism of this transport is organelle movement, caused by an ATP-driven movement of myosin motors attached to the organelles along the actin cytoskeleton [5, 169, 191]. Unbound structures move via diffusion, a passive process of molecule distribution. We raised the question whether what we see as cytoplasmic streaming includes a passive component of organelle drag induced by the actively moving organelles. Our experimental work indeed is in agreement with our theoretical considerations that the active transport induces hydrodynamic flow in the cytoplasm that surrounds the organelles, speeding up the transport of otherwise only diffusing molecules.

Difference between young and mature cells in organelle transport

The velocities of cytoplasmic streaming vary between different cell types, the developmental stage of the cell and the species. This is interesting, because these cells have similar myosins that belong to plant specific subfamilies of Myosin VIII and XI. Myosins XI are more abundantly expressed in plant cells than Myosin VIII. Myosin XI has been shown to be present on peroxisomes [192] and fragments of the tail may localise to Golgi and mitochondria [193]. Myosin VIII appears to be restricted to the plasma membrane and plasmodesmata [194]. This makes Myosin XI the candidate motor molecule involved in organelle transport [1]. We observed differences in velocities of organelle movement through cytoplasmic strands between small elongating and large fully elongated cells of a tobacco BY-2 suspension culture. This phenomenon is not specific for cells from this suspension culture. Also in other fully elongated plant cells, of for instance *T. virginiana* stamen hairs, the velocity of organelle movement increases during cell elongation and is maximal in fully elongated large mature cells (own observation, unpublished). The most obvious visible difference between these cells, besides their difference in size, is the larger volume that is taken up by the vacuole in the fully elongated cells. Molecules move faster for longer distances through thinner tubes. Differences in speed of cytoplasmic streaming have been observed within different parts of one and the same cell, namely, in root hairs and pollen tubes, that grow at the cell tip that contains only vesicles, which show little movement [168]. In the sub-apical cytoplasmic dense region of these growing hairs the net speed of organelles is low up to 2 μm/s (*Equisetum hyemale* [177], *Vicia sativa* [178], *Medicago truncatula* [168]). In the shank of tip growing root hairs where the central vacuole is present, the net speed of organelles is 8-14 μm/s (*Equisetum hyemale* [177], *Vicia sativa* [178], *Medicago truncatula* [168]). In these cells, these differences can be linked to the configuration of the actin cytoskeleton, which consists of thick bundles in the hair tube but of thin bundles in the subapex (*Equisetum hyemale* [177], *Vicia sativa* [178], *Arabidopsis thaliana* [195]; *Eucalyptus globulus* [196]). In the sub-apex, organelles often stop for a short time and jump for a short distance from one place to the other [168]. Also the possible differences in the configuration of the actin cytoskeleton between the elongating and fully elongated BY-2 suspension cells are expected to be the underlying mechanism of the measured differences in velocities of organelle movement. If indeed the myosin type is the same in both cell structures, it cannot be the step size that determines organelle velocity, but the number of steps made per time unit.

Need for hydrodynamic flow in large cells

Molecules in the cytosol that are not attached to the cytoskeleton do not posses an active driving force for transport. They move by Brownian motion only. If a concentration gradient is produced for instance by the consumption of molecules at one side of the cell, such as the high rate of sugar use at the cell cortex to produce the cell wall, directional movement governed by Brownian motion is the result. Here we show that movement of molecules in a cell, and maybe also ribosomes, vesicles and small organelles, is faster than mere diffusion, and that the cause for this speeding up is the active transport of organelles along bundles of actin filaments, as theoretically predicted [149]. If the velocity of organelles in the cytosol of tobacco BY-2 suspension cells is three times faster, the GFP molecules move also three times faster (Fig.5.6). Why would this be useful for cells? Signalling and other proteins have to find a partner to bind to for their activity, and these activities have to be carried out at the right sites in the cell. If all of these molecules had to be produced at the site where needed, this would require precise targeting of ribosomes, including the free ribosomes and polysomes not attached to the endoplasmic reticulum. Now we show that random molecule movement inside the cytoplasm, can be speeded up by myosin-driven organelle movement along the actin cytoskeleton, increasing the chance for finding a partner. In the cells that have fast cytoplasmic streaming, hydrodynamic coupling between actively transported organelles and the surrounding solvent causes molecules to spread faster, with the result that those molecules will reach their target with greater efficiency.

The mature BY-2 suspension cells that we studied have velocities of cytoplasmic streaming 10-15 times lower than for instance some of the root hairs studied, or than mature *Tradescantia* stamen hair cells. We expect that in those cells also organelles, or at least vesicles, could be dragged along with the actively moved motor-driven organelles. Also lipid droplets injected into hyphal extensions of *Neurospora crassa* moved without motor proteins [197]. The movement of fluorescent stealth vesicles injected into *T. virginiana* stamen hair cells in the cytoplasmic strands indicates that these vesicles and possibly organelles can also move by hydrodynamic flow in the cytoplasm of plant cells.

Chapter 6

Hydrodynamic Interactions In A Continuum Model

Introduction

In chapter 4 it was shown by means of computer simulations, that momentum transfer via the fluid medium can give rise to a non-negligible flow of suspended organelles. The simulations were performed using an extended exclusion model that included Langmuir Kinetics and hydrodynamic interactions. In stead of simulating all the molecules that make up the surrounding fluid, the influence of the solution on the solutes was introduced as a combination of random forces and frictional terms [69]. The organelle velocities were calculated using a Langevin equation (eq.4.1) that included the hydrodynamic organelle-organelle interactions and the resulting velocity was translated into a trial move using the algorithm described in Fig.4.2. Taking hard-core excluded volume interactions into account, this trial move was subsequently, accepted, partially accepted or rejected. In the latter case the motor-organelle complex simply dwells in its current position. In spite of its simplicity, the lattice model sufficed to show the effect of hydrodynamic interactions in the system. Moreover, the model could be easily modified to study different systems and conditions. However, performing the simulations on a lattice had a few disadvantages. These include:

- Excluded volume effects affect lattice velocities (see appendix A).
- Spurious effects affect the measured motor velocities (see Appendix B).
- Spatial and temporal resolution of the simulations are large with respect to the organelle size (see table 4.1).
- The magnitude of thermal energy and the diffusion coefficient in the simulation model are larger than in experiments. (see the discussion below table 4.1).

The consequences of the above points are understood and discussed. To rule out that the directed suspended organelle transport in solution is not a lattice artefact, a simulation model is developed in which the motor positions are no longer mapped on a lattice. In stead, the motor displacements will be directly calculated using the Langevin equation. The continuum model and the obtained results are described in the sections below. Note, in this chapter, motor-cargo complexes will be referred to as motors or organelles, unless specified otherwise.

Finally, at the end of this chapter the results obtained using the both simulation models will be compared to each other and to experimental data. This includes a discussion of the magnitude of the observed velocities, forces and the implications for the underlying bio-mechanical system.

The Simulation Model

The system that is modelled is similar to the one that is shown in Fig.4.4 in chapter 4. The difference is that the motor positions are not mapped on a lattice but move through a continuum. As was the case with the lattice model, the motors alternate between periods of diffusive and directed transport depending on their position in the system. In addition, the motors have a finite processivity and the filament occupation fraction of motors is determined by Langmuir Kinetics. Moreover, the system makes use of Periodic Boundary Conditions in axial direction to simulate the dynamics of an infinite system. However, for the simulations to be performed on a continuum environment, a number of changes need to be made with respect to the lattice model. These changes are described in this section.

Solving The Langevin Equation

Since the motors will now be moving in a continuum (without the mapping algorithm) the spatial and temporal resolution of the simulations must be improved. To allow for small displacements and time steps the Langevin Equation (eq.4.1) is integrated from time t to $t + \Delta t$ and discretized with respect to time. This yields [63]:

$$\boldsymbol{r}_{\mathrm{i}}\left(t+\Delta t\right)=\boldsymbol{r}_{\mathrm{i}}\left(t\right)+\boldsymbol{\mu}_{\mathrm{ii}}\cdot\boldsymbol{F}_{\mathrm{i}}\Delta t+\sum_{\mathrm{j,j\neq i}}\boldsymbol{\mu}_{\mathrm{ij}}\cdot\boldsymbol{F}_{\mathrm{j}}\Delta t+\Delta\boldsymbol{G}_{\mathrm{i}}(t). \tag{6.1}$$

The mean and variance of the random displacement are given by [63]:

$$\begin{aligned}\langle\Delta\boldsymbol{G}_{\mathrm{i}}(t)\rangle&=\boldsymbol{0}\\ \langle\Delta\boldsymbol{G}_{\mathrm{i}}(t)\Delta\boldsymbol{G}_{\mathrm{j}}(t^{'})\rangle&=2\boldsymbol{D}_{\mathrm{ij}}\delta_{\mathrm{t,t'}}\Delta t.\end{aligned} \tag{6.2}$$

As described in chapters 2 and 4, the organelle mobilities, $\boldsymbol{\mu}_{\mathrm{ij}}=\boldsymbol{D}_{\mathrm{ij}}/k_{\mathrm{b}}T$, depend on the positions of all the organelles in the system and are calculated using the Oseen tensor (eq.2.25). The correlated thermal displacements are determined using the Ermak and McCammon algorithm [72] described in chapter 4 (see eq.4.4)[*]. The theoretical single motor velocity is given by $\boldsymbol{V}_0 = (V_0, 0, 0)$ for a filament bound to the cytoskeleton and $\boldsymbol{V}_0 = (0, 0, 0)$ for bound motors. For bound motors $\boldsymbol{V}_0$ can be calculated via $\boldsymbol{V}_0 = \boldsymbol{\mu}_{\mathrm{ii}} \cdot \boldsymbol{F}_0$ where $\boldsymbol{F}_0 = (F_0, 0, 0)$. For suspended organelles $\boldsymbol{F}_0 = (0, 0, 0)$.

Yukawa Potential

In the lattice model the motor-organelle complexes were treated as hard spheres. This was enforced by only allowing one motor on a lattice node at a given moment in time. In addition, the lattice spacing was larger than the motor diameter. Thus, there was no overlap possible between motors in adjacent lattice nodes. In a continuum model the displacements of the motors are no longer limited to fixed positions. To avoid overlap, the motors will be treated as hard spheres surrounded by a soft repulsive potential, $V(\boldsymbol{r}_{\mathrm{ij}})$. In the simulations the *Yukawa potential* is used, which has the following form:

$$V(\boldsymbol{r}_{\mathrm{ij}}) = W \frac{e^{-\frac{r_{\mathrm{ij}}}{r_{\mathrm{c}}}}}{r_{\mathrm{ij}}}. \tag{6.3}$$

In this equation, W, is a pre-factor that determines the strength of the repulsion. The distance between two organelles is, r_{ij}, and the cut-off range of the potential is given by, r_{c}. The potential gives rise to a conservative repulsive force[†]:

$$\boldsymbol{F}(\boldsymbol{r}_{\mathrm{ij}}) = W \frac{e^{-\frac{r_{\mathrm{ij}}}{r_{\mathrm{c}}}}}{r_{\mathrm{ij}}} \left[\frac{1}{r_{\mathrm{ij}}} + \frac{1}{r_{\mathrm{c}}}\right] \hat{\boldsymbol{r}}_{\mathrm{ij}}. \tag{6.4}$$

Next, the force is truncated and shifted [156], $\boldsymbol{F}^{\mathrm{T-S}}(\boldsymbol{r}_{\mathrm{ij}})$, by subtracting the force, $\boldsymbol{F}_{\mathrm{c}}$, which is the force at the cut-off distance, $r_{\mathrm{ij}}=R_{\mathrm{c}}=r_{\mathrm{c}}$. The resulting force decreases with increasing organelle distance and reduces to zero at R_{c}. In this equation, $\hat{\boldsymbol{r}}_{\mathrm{ij}}=\boldsymbol{r}_{\mathrm{ij}}/r_{\mathrm{ij}}$, is a unit vector along the vector $\boldsymbol{r}_{\mathrm{ij}}$ that points from organelles i to j. The force is given by:

$$\boldsymbol{F}^{\mathrm{T-S}}(\boldsymbol{r}_{\mathrm{ij}}) = \boldsymbol{F}(\boldsymbol{r}_{\mathrm{ij}}) - \boldsymbol{F}_{\mathrm{c}} = \hat{\boldsymbol{r}}_{\mathrm{ij}} \begin{cases} W \frac{e^{-\frac{r_{\mathrm{ij}}}{r_{\mathrm{c}}}}}{r_{\mathrm{ij}}} \left[\frac{1}{r_{\mathrm{ij}}} + \frac{1}{r_{\mathrm{c}}}\right] - \frac{2We^{-1}}{r_{\mathrm{c}}^2} & r_{\mathrm{ij}} \leq R_{\mathrm{c}} \\ 0 & r_{\mathrm{ij}} > R_{\mathrm{c}}. \end{cases} \tag{6.5}$$

---

[*] In the section 'Ermak and McCammon Algorithm'

[†] For a conservative force holds: $\boldsymbol{F}(\boldsymbol{r}_{\mathrm{ij}}) = -\nabla V(\boldsymbol{r}_{\mathrm{ij}})$.

Note that, $\boldsymbol{F}^{\mathrm{T-S}}(\boldsymbol{r}_{\mathrm{ij}}) = -\boldsymbol{F}^{\mathrm{T-S}}(\boldsymbol{r}_{\mathrm{ji}})$. The repulsive forces need to be calculated for each pair of organelles for the organelle configuration at the start of a simulation time step. Finally, the repulsive forces are introduced in the Langevin equation (eq.6.1) via:

$$\boldsymbol{F}_{\mathrm{i}} = \boldsymbol{F}_0 + \sum_{\mathrm{j,j\neq i}} \boldsymbol{F}^{\mathrm{T-S}}(\boldsymbol{r}_{\mathrm{ij}}) \,. \tag{6.6}$$

Conversion Of Units

The conversion between simulation units and the experimental data can be found in table 6.1*. Analogous to table 4.1, the conversion factors for length L, time T, and mass M, are found by fixing the radius, velocity and force in the simulation model. Note that, unlike in the lattice model, all the simulation settings can be converted back into experimental values.

Property	Unit	Experiments	Model	Factor	Calculated
a	m	2.5×10^{-7}	0.25	L	2.5×10^{-7}
V_0	m/s	8×10^{-7}	0.4	L/T	8.0×10^{-7}
F_0	N	4.15×10^{-12}	1.0	ML/T^2	4.15×10^{-12}
μ_0	m/Ns	1.93×10^{5}	0.4	T/M	1.93×10^{5}
η	Pas	1.1	0.53	M/LT	1.1
ρ	kg/m^3	1200	1.16×10^{-9}	M/L^3	1200
D_0	m^2/s	8.26×10^{-16}	4.13	L^2/T	8.26×10^{-16}
$k_{\mathrm{b}}T$	J	4.28×10^{-21}	1.03×10^{-3}	ML^2/T^2	4.28×10^{-21}
m	kg	7.85×10^{-17}	7.57×10^{-11}	M	7.85×10^{-17}
τ	s	1.52×10^{-11}	3.03×10^{-11}	T	1.52×10^{-11}

Table 6.1: *Conversion table from experimental data (see table 2.2 in chapter 2) to simulation parameters. The conversion factors are:* L=1.0×10^{-6}, T=5.0×10^{-1}, M=1.0375×10^{-6} *and were determined by fixing the radius (a), and the single motor velocity (V_0) and force (F_0) in the simulation model. The column 'calculated' is obtained by multiplication of the columns 'model' and 'factor' and it reflects how well the simulation parameters represent the experimental data.*

Results

To compare both types of models, the same geometry is used in the simulations. This means that motors move in a two dimensional plane that is confined between two fil-

---

*See the explanation in chapter 4 with table 4.1

aments (see Fig.4.4) while the hydrodynamic interactions between the organelles are treated as in a three dimensional fluid. In the continuum a different definition will be used for the concentration. For the lattice model the concentration was defined as the fraction of lattice nodes that are occupied along the filament or in solution (ϕ_μ and ϕ_s). In this chapter, the concentration is defined as the fraction of space that the motors occupy and will be denoted by: ϕ'_μ or ϕ'_s. The following equation can be used to switch from one definition to the other:

$$\phi' = \frac{\langle N_\mathrm{p} \rangle d}{L} = \phi d. \tag{6.7}$$

In the above equation, d, is the organelle diameter and, $\langle N_\mathrm{p} \rangle$, the average number of organelles in the system. In the section below, the results obtained with the continuum model will be discussed. Subsequently, in the next section, these results will be compared to the lattice model.

Continuum Model

In Fig.6.1A, the normalised motor velocity is shown for both bound and suspended organelles. The data shows that, in the absence of hydrodynamic interactions, the velocity is not affected by excluded volume effects. For all tested filament concentrations the measured velocities, on average, were equal to the single motor velocity V_0. In addition, there is no directed organelle motion in solution. Inclusion of the momentum transfer via the fluid shows a linear increase of the organelle velocity with increasing bound organelle concentration. The latter is in agreement with the Langevin equation that predicts a linear relation between the force (from the bound organelles) and the velocity. Additionally, the suspended organelle velocity (shown for the centre-line of the system) increases linearly with increasing filament occupation albeit at a different (less steep) slope. Figure 6.1B demonstrates that the angle of the slope depends on the organelle's radial distance from the filament, the closer to the filament, the more the slope approaches that for bound organelles and the higher the measured velocity. The latter observation was expected since the hydrodynamic interactions are introduced via the Oseen tensor (eq.2.25). This tensor states that the momentum transfer via the fluid is long range and falls off with the inverse of the distance from the organelle*.

The forces that are acting on the bound and suspended organelles are deduced from the mobility and velocity via F_i=V_i/μ_0. The normalised forces are shown in Fig.6.1C. As expected, the forces increase with increasing bound organelle concentration when hydrodynamic interactions are considered and remain constant in the absence of the momentum transfer via the fluid. The hydrodynamic contribution to the force on the

---

*See the section 'Many Organelles Moving In A Fluid - Hydrodynamic Interactions' in chapter 2.

bound motors (filled circles) is always larger than the force acting upon the suspended organelles.

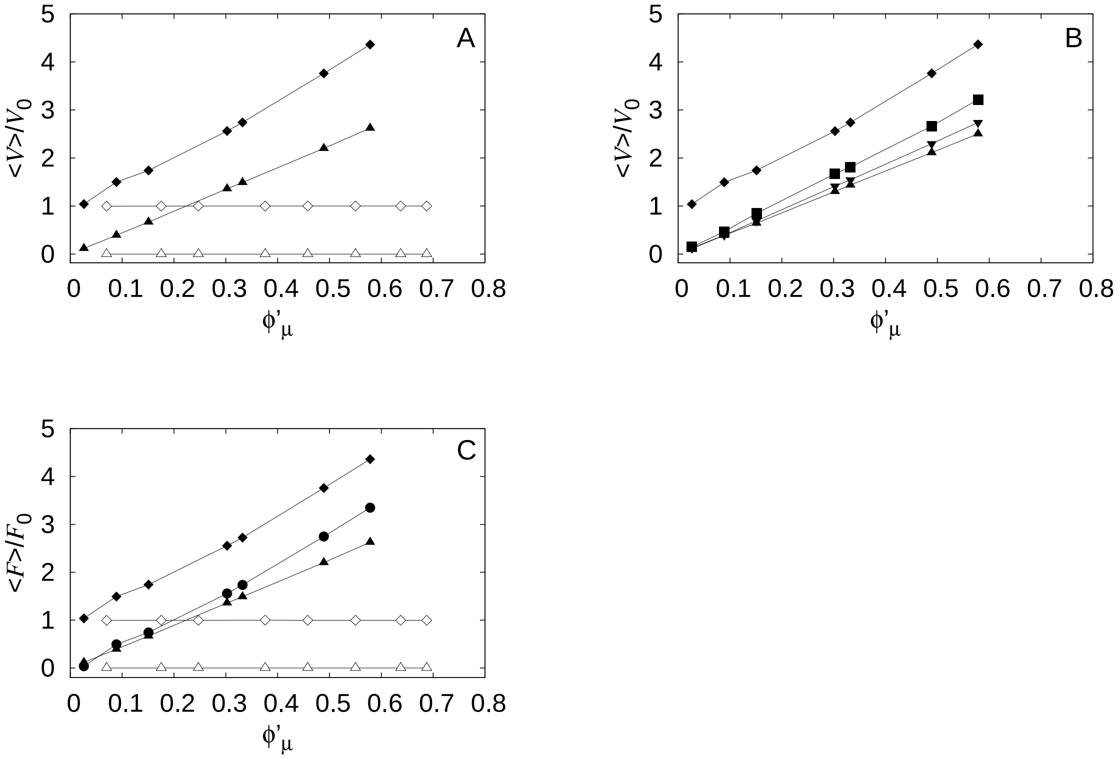

Figure 6.1: *A) The average normalised axial organelle velocity for different degrees of filament occupation, ϕ'_μ, measured along the filament and in solution. B) The average axial normalised organelle velocity at different radial positions in the system. Diamonds - filament (f); squares $f+2a$; inverted triangles $f+6a$; triangles $f+10a$ i.e. centre-line of system where, $a=0.25$, is the organelle radius in simulation units. C) Effective normalised force acting on motors for different filament occupations with $F_0=4.15$ pN (see table 6.1). The filled circles represent the hydrodynamic force acting on the bound organelles. For all figures: filled symbols - with hydrodynamic interactions (HI); open symbols - without HI; diamonds - filament; triangles - solution at centreline of system. See the column 'Model' in table 6.1 for the simulation settings. The simulations were performed for 150×10^6 simulation time steps with $dt=0.0001$. The Yukawa constants: $W=0.05$ and $r_c=0.25$ (all in simulation units).*

The organelle concentration profile that arises from the exchange of organelles between the filament and solution is presented in Fig.6.2A. The figure shows the axial concentration of organelles across the width, L, of the system. In the absence of hydrodynamic interactions (open symbols), the binding and detachment of organelles gives rise to a concentration drop near the filament. This drop is followed by an increase of organelles in the centre of the system. This profile is robust as the data for different filament occupation fraction collapses (not shown). Including the hydrodynamic coupling to the simulations does not change the shape of the concentration profile. However, it does result in a smaller filament occupation and a larger organelle accumulation at the centre of the system (for identical simulation settings). To investigate if the profile's shape is a result of using the repulsive Yukawa potential (eq.6.5) to prevent organelle overlap, the simulations were repeated for a smaller value of the repulsion parameter W=0.005 (in simulation units). Changing this parameter did not have any effect on the obtained concentration profile (not shown). Modifying the cut-off length, R_c, for the force in (eq.6.5) to a value of 3 or 6 times the organelle radius, while keeping r_c constant for the potential, did not have any significant effect on the profile either (not shown). Additionally, as the Yukawa potential has only a short-range effect (r_c=0.25, in simulation units), one would expect the repulsion effect to be more pronounced at higher filament occupation fractions. However, the figure does not show any dependency on the filament concentration.

As expected, the normalised velocity profile (Fig.6.2B) shows that, in the absence of the hydrodynamic coupling, the single motor velocity is recovered along the filament and on average there is no net velocity in solution. Including the hydrodynamic interactions (filled symbols) again shows that the velocity increases for both bound and suspended organelles with increasing filament occupation. In line with the results from 6.1B, the velocity decreases with increasing distance from the filaments, and thus is smallest in the centre of the system.

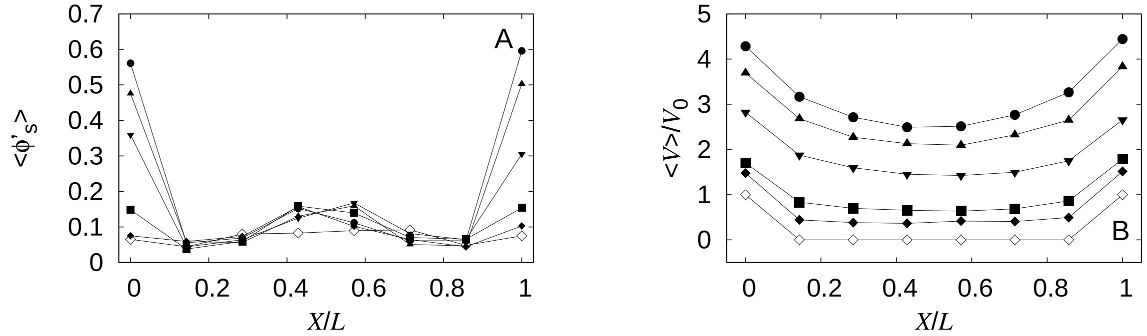

Figure 6.2: *A) Axial concentration profiles for organelles bound to the filament and in solution for different filament occupation fractions. L is the distance between filaments, and X the distance to the lower filament. B) Normalised axial organelle velocity at different distances from the filament. For all figures: filled symbols - with hydrodynamic interactions (HI); open symbols - no HI (with* ϕ'_μ=0.07*); diamonds* ϕ'_μ=0.09*; squares* ϕ'_μ=0.15*; inverted triangles* ϕ'_μ=0.33*; triangles* ϕ'_μ=0.49*; Circles* ϕ'_μ=0.58*. See the column 'Model' in table 6.1 for the simulation settings. The simulations were performed for* 150×10^6 *simulation time steps with dt*=0.0001*. The Yukawa constants:* W=0.05 *and* r_c=0.25 *(all in simulation units).*

Comparing The Models

Next, the results that were obtained using the lattice model (chapter 4) are compared to those of the continuum model. The discussion is limited to the data for simulations that include hydrodynamic interactions. To be able to compare both models, all the data is converted into real units using the conversion tables 4.1 and 6.1. The definition for the organelle concentration that was introduced in this chapter will be used i.e. ϕ'_μ or ϕ'_s (see eq.6.7). Most of the results that were presented in chapter 4 are for a organelle radius of a=$0.1l$ (in lattice units, where l=2.5×10^{-7}m is the lattice spacing). In this section additional data for a=$0.2l$ is shown.

Figure 6.3A, compares the bound organelle velocity for different degrees of filament occupation. For the lattice model, both series overlap at low filament occupation fractions. At higher values the series start to deviate due to excluded volume interactions. The series for a=$0.1l$ is the first to decrease its velocity with increasing filament occupation fraction. This is as expected, as the smaller size organelles take up less volume for the same lattice filament occupation fraction at identical lattice spacing l. In contrast, the data from the continuum model shows a linear increase in velocity with increasing filament occupation as this model does not experience the excluded volume effects imposed by the lattice. The slope is similar to the initial slope of the lattice model. The velocities obtained at small concentration fractions are slightly larger for the lattice model. This can be attributed to spurious effects (see the discussion in Appendix B).

The velocity for the suspended organelles is shown in Fig.6.3B. Again the data obtained using the lattice model collapses at small filament occupation fractions. In addition, the data shows that the organelle velocity decreases when excluded volume effects decrease the bound motor velocity. The data from the continuum model shows a continuous linear increase of the velocity albeit at a smaller slope than for the lattice model. The forces acting on both the bound and suspended organelles are deduced from the mobility and velocity via $F_\mathrm{i} = V_\mathrm{i}/\mu_0$ and are shown in Fig.6.3C. As there is a linear relation between the force and velocity at low Reynolds numbers this figure shows similar trends to Fig.6.3A and B. Note that for the lattice model, the forces acting on suspended organelles are larger than those on the bound motors at higher filament occupations. Indeed, comparing the additional hydrodynamic force, via momentum transfer, that acts upon the bound organelles (Fig.6.3D) to the force acting upon the suspended (filled circles in Fig.6.3C) organelles confirms this.

The axial concentration and velocity profiles for different radial distances from the filament are shown for ϕ'_μ≈0.08 and 0.15. For radius a=$0.1l$ this approximately corresponds to respectively ϕ_μ≈0.39 and 0.79 and for a=$0.2l$ to ϕ_μ≈0.19 and 0.39. A comparison of the axial concentration profile at the filament and in the solution is shown in Fig.6.4A. The lattice model results (open symbols) show that the data for the identical ϕ'_s collapses and that there is a flat profile in solution (with a small concentration increase

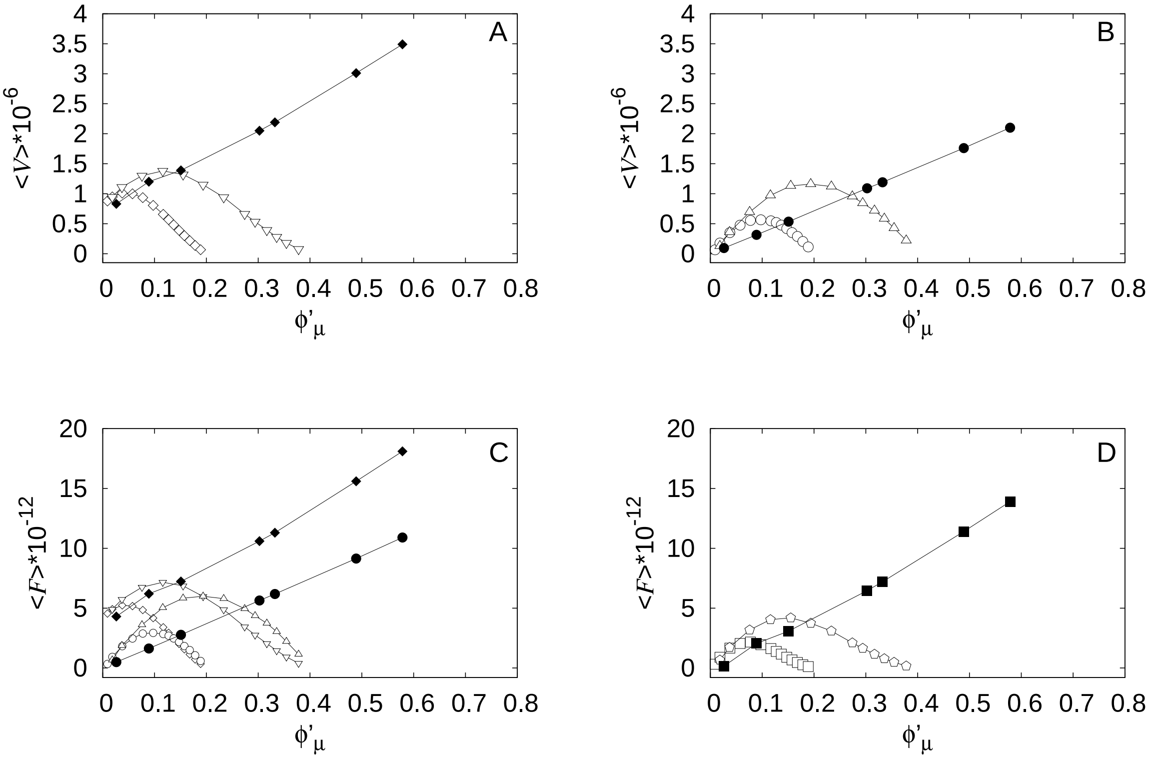

Figure 6.3: *A) Comparison of the average bound motor velocity* $\langle V\rangle$ *in m/s at different filament occupation fractions* ϕ'_{μ}. *B) The average axial velocity of suspended organelles in the centre of the system. C) Motor force in N for bound and suspended organelles. D) Hydrodynamic force in N for bound and suspended motors. For all figures: lattice model (open symbols); continuum model (filled symbols). Open symbols: diamonds (*a=0.1l*) and inverted triangles (*a=0.2l*) - bound organelles; circles (*a=0.1l*) and triangles (*a=0.2l*) - suspended organelles; open squares (*a=0.1l*) and open pentagons (*a=0.2l*) - hydrodynamic force;* l=2.5 $\times$ 10^{-7}*m is the lattice spacing. Filled symbols: diamonds and squares - bound organelles; circles - suspended organelles. Experimental data:* a=2.5 $\times$ 10^{-7} *m,* V_0=0.8 $\times$ 10^{-6} *m/s,* F_0=4.15$\times$$10^{-12}$ *N,* η=1.1 *Pas,* T=37 °C, μ_0 = 1.93$\times$$10^5$ *m/Ns,* Re=4.36$\times$$10^{-10}$, D_0=8.26$\times$$10^{-16}$ *m^2/s (see tabel 2.2). Conversion of units via tables 4.1, 6.1 and eq.6.7.*

near the filaments). However, the continuum model shows a drop in concentration near the filament followed by an accumulation of organelles in the solution. This effect gets stronger when including the hydrodynamic interactions. Note that the statistics of the continuum model data are poorer than for the lattice model. In the simulations both the N^2 Oseen mobility tensor (eq.2.25) and the Ermak and McCammon algorithm (eq.4.4) have to be calculated for each simulation step. As the continuum model uses smaller simulation time steps, these matrices need to be evaluated more frequently for this model. Thus, to run the continuum simulations for a similar total time as was used for the lattice model, the number of organelles had to be decreased by shortening the length of the system. The normalised velocity profiles (Fig.6.4B) show that profiles are similar in shape for all series. The one exception is for the lattice model at $\phi'_\mu \approx 0.15$ (a=$0.1l$) where the velocity in solution is larger than along the filament. This is caused by spurious lattice effects and is discussed in detail in appendix B. The velocities profile drops slightly with increasing distance from the filament. This decrease with the distance is larger for the continuum model.

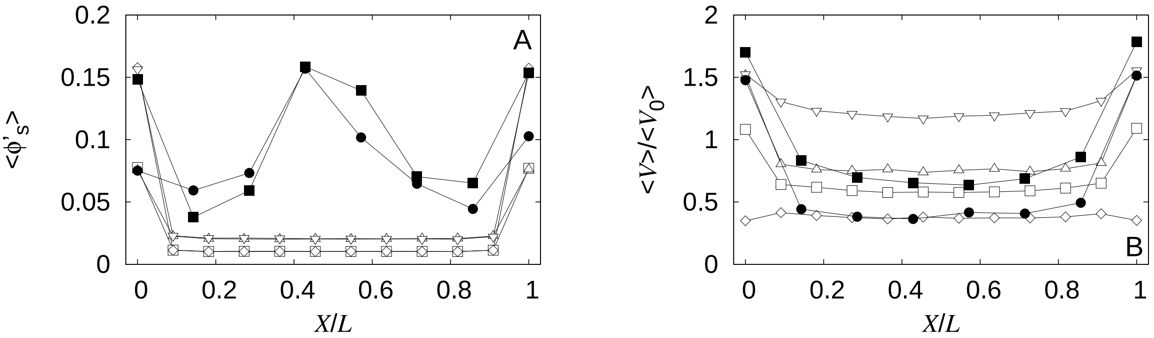

Figure 6.4: *A) Axial concentration profiles for organelles bound to the filament and in solution for different filament occupation fractions. B) Normalised axial organelle velocity at different distances from the filament.* $\phi'_\mu \approx 0.08$*: lattice - open squares (*a=$0.1l$*), open triangles (*a=$0.2l$*); continuum - filled circles.* $\phi'_\mu \approx 0.15$*: lattice - open diamonds (*a=$0.1l$*), open inverted triangles (*a=$0.2l$*); continuum - filled squares. For both figures: L is the distance between bio-filaments, and X the distance to the lower bio-filament and* l=$2.5 \times 10^{-7}m$ *is the lattice spacing. Experimental data:* a=2.5×10^{-7} *m,* V_0=0.8×10^{-6} *m/s,* F_0=4.15×10^{-12} *N,* η=1.1 *Pas,* T=37 °C, $\mu_0 = 1.93 \times 10^5$ *m/Ns,* Re=4.36×10^{-10}, D_0=8.26×10^{-16} m^2*/s (see table 2.2). Conversion of units via tables 4.1, 6.1 and eq.6.7.*

Discussion

The goal of this chapter is to validate the results that were obtained using an extended exclusion model (chapter 4) by using a continuum simulation model. As explained in the introduction, the lattice model is sensitive to excluded volume effects, spurious lattice dynamics and has a coarse spatial and temporal resolution. All these factors may influence the outcome of the simulations. The continuum model that was introduced in this chapter does not have these sensitivities and is used to validate the results. Both models show that momentum transfer via the fluid indeed has a positive effect, resulting in higher bound and suspended organelle velocities. This effect, that was also confirmed experimentally (see chapter 5), thus cannot be neglected.

However, there still are some concerns. The results from the continuum model show that the measured velocities (and drag forces) increase linearly with the organelle concentration. This does not take any physical limitations of the molecular motors into account. Actual motor velocities depend on the speed at which a motor physically can step i.e. on the speed of the conformational changes (crossbridge cycle) that take place inside the motor protein during the hydrolysis of ATP. In the text below the simulation results are discussed and compared to experimental data.

The single motor parameters that are used in the simulations (see tables 4.1, and 6.1) are chosen in the velocity and force range of both kinesin and myosin motors. I introduce the motor-organelle complexes into the simulations without specifying the type of molecular motor. This allows for subsequent analysis from the perspective of either motor type. The used single motor parameters are based on a combination of experimental data as summarised in table 2.2. In this table a representative model system for a molecular motor cargo is introduced. I chose a cargo size of 500 nm that could e.g. represent the size of a melanosome [21], which is a typical organelle (see table 1.1). The velocity for kinesin motors carrying a cargo of similar size was found to be ≈800 nm/s [17, 62]. This velocity was chosen as the single motor velocity in the simulations as it also falls within the velocity range of myosin motors (table 6.2). The cytosol viscosity that was measured *in vivo* for different cells is summarised in table 2.4. I chose to use the viscosity from the publication of Hill et all. [23] where it is given as 1.1 Pas for kinesin motors carrying cargoes of 250-500 nm in a PC12 cell. Finally, using the velocity, viscosity and organelle size, the accompanying mobility (eq.2.19) and motor force are calculated (eq.2.19) together with other parameters (see chapter 2). The results are summarised in table 2.2.

Velocities

In table 6.2, the simulation results are discussed from the perspective of both kinesin and myosin motors. The table shows the maximum velocities that were measured in the simulations and compares these to some of the fastest molecular motors that have been reported in literature. The velocities found in the simulations are large with respect to the single motor velocity but still fall within the range of the fastest motors that are reported in literature.

Forces

The forces needed to move the organelles at the largest velocities in the simulations exceed the single motor stall forces reported in literature (kinesin: 4.2 pN [33]; 5.4 pN [15], 5.7 pN [10]; myosin: 3 pN [199]; 3-4 pN [203]; 5-6 pN [204]). However, Hunt et al. [33] presented experimental data that shows that the stall force increases with

Velocity $\mu m/s$	**Force**[a] pN	**Steps**[b] s^{-1}	**ATPase**[c] s^{-1}head^{-1}	**Comment**	**Reference**
Experimental Data For Molecular Motors					
0.4 - 0.8	2.1 - 4.2	50 - 100	25 - 50	Kinesin	[17]
0.77 - 0.88	4.0 - 4.6	96.3 - 110	48.1 - 55	*Drosophila* Kinesin	[62]
2 - 3.5	10.1 - 18.2	250.0 - 437.5	125.0 - 218.8	DdUnc104[d]	[198]
0.3	1.56	8.1	4.1	Myosin-V	[199]
0.6	3.13	16.3	8.2	Myosin-Va[e]	[200]
7	0.6	189.2	94.6	Myosin-XI	[30]
30 - 62	13	810.8 - 1621.6	405.4 - 810.8	Myosin	[201]
1.6 - 3.6	3.5 - 39	-	-	Muscle Myosin[f]	[202]
Simulations					
Single Motor					
0.8	4.15	100	50	Kinesin	Table 2.2
0.8	4.15	21.6	10.8	Myosin	Table 2.2
Kinesin					
1.4	7.17	172.7	86.4	Lattice model	Fig.6.3A
3.5	18.11	436.4	218.2	Continuum model	Fig.6.3A
Myosin					
1.4	7.17	37.3	18.7	Lattice model	Fig.6.3A
3.5	18.11	94.4	47.2	Continuum model	Fig.6.3A

Table 6.2: *Comparison of simulation results to the fastest molecular motors described in literature. It is assumed that one ATP is consumed per step. Calculated values:* [a]$F{=}v/\mu_0$ *with* $\mu_0{=}1.93 \times 10^5$ *m/Ns;* [b]steps$=v/$step size. *The step sizes of kinesin and myosin are respectively 8 and 37 nm;* [c]*ATPase is the rate of hydrolysis per head per second. For a dimeric motor:* ATPase=steps/2; [d] *A dimeric kinesin motor of the UNC104/KIF1a motor subfamily observed in Dictiostellium;* [e] *Measured in vivo in a COS-7 cell, in vitro velocity, 0.58* $\mu m/s$*;* [f]*An estimated 4-40 myosin heads are attached.*

increasing motor density where motors share the load. For example, the largest stall force reported in this article for kinesin motors is 16 pN. The latter force is similar to the force found for the largest measured velocity in the simulations. This suggests that for the results to be plausible multiple molecular motors need to be attached to the same organelle that cooperate and share a load. The latter can be described by the following equation [134], where, N, is the number of motors:

$$V_\mathrm{i} = N\mu_0 F_\mathrm{i}. \tag{6.8}$$

That multiple motors can be attached to a cargo was confirmed experimentally by Ashkin et al. [28] and Hirokawa [29] who used electron microscopy imaging on fixed cells to show that some vesicles were attached to the microtubules by 2-3 kinesin motors. In addition, *in vivo* experiments, using quantum dots as positional markers for molecular motors, show that the velocity of organelles are constrained to quantised values suggesting that each peak represents a different number of motors pulling a vesicle through a viscous solution [25,31,41,42].

From single motor force-velocity experiments it is known that the motor processivity decreases when there is either a positive or negative force exerted upon the motors (kinesin [11]; myosin-V [55]). However, when multiple motors are collectively carrying a cargo, the cargo's processivity is increased [147]. A theoretical study by Klumpp et al. [134] suggests that the distance, x, that a cargo can travel before detachment can be predicted by: $x{=}5^{N-1}/N$. These arguments suggest that, in the presence of external forces, it would be beneficial for motors to collectively carry cargoes through the cell.

ATPase and Duty Ratio

Joe Howard mentions in his book [3][*] that the free energy derived from the hydrolysis of ATP under typical cellular conditions is 100 pN·nm=25 $\mathrm{k_b}$T ([ATP]$\sim$10 mM; [ADP]$\sim$10 μM; [$\mathrm{P_i}$]$\sim$1mM). This means that under these conditions the thermodynamic force, i.e. the maximum force that a single, fully reversible kinesin motor, could theoretically work against is 12 pN ($=$100 pN·nm/8 nm) and 2.7 pN for myosin. These forces are smaller than the forces at high velocities in our simulations and smaller than for the fast motors in literature (see table 6.2). This suggests that either the physiological conditions in the cells are very different and/or that motors are sharing the load. A typical stall force for a kinesin motor is 5-6 pN, which means that the kinesin does 40-48 pN·nm of work and that the efficiency of this motor is about 40-48%.

The ATPase rates found for the maximum velocities of the simulations are large compared to those of a single motor. For example, for a single hypothetical myosin motor moving at 0.8 $\mu m/s$ the ATPase rate is 10.8 $\mathrm{s^{-1}head^{-1}}$ (see table 6.2). However, the ATPase rate at the maximum velocities that was measured in the simulations are 2 (lattice model) - 5 (Continuum model) times larger. Interestingly, the ATPase rates for myosin in experiments can be much larger than this value e.g. 94.6 $\mathrm{s^{-1}head^{-1}}$ for Myosin-XI [30]. In addition, Sugi et al. [205] found an ATPase rate of 425 $\mathrm{s^{-1}head^{-1}}$ in the internodal cells of *Chara corallina*. The authors argue that this is a large value with respect to the single motor ATPase and mention that a mechanically coupled interaction between the heads of multiple myosin molecules attached to the same bead would be advantageous.

The duty ratio[†], r, is the ratio between the time a motor head spends attached, τ_{on},

---

[*] On pages 230-231 and 254.

[†] See appendix D for a more detailed explanation of the duty ratio.

and the total time of the crossbridge cycle of a motor, $\tau_{\rm tot}$, and is given by [3,76]:

$$r = \frac{\tau_{\rm on}}{\tau_{\rm tot}} = \frac{\delta \ {\rm ATPase}}{V}. \tag{6.9}$$

In this equation, δ, is the step size of the motor, ATPase, its ATPase rate and, V, the velocity. For a single processive molecular motor the duty ratio has to be at least 0.5. A smaller value means that there are moments that neither of the two motor heads is attached to the cytoskeleton and that thus the motor would detach from the filament. For non-processive motors, such as muscle myosin, this value is much smaller than 0.5. The cooperativity hypothesis suggests that even though the duty ratio of the individual motors is 0.5 or larger, the effective duty ratio could be smaller than 0.5. For example, if we assume that the fastest experimental kinesin velocity in table 6.2 is the result of a group of motors that collaborate[*], then the duty ratio becomes 0.11. Using another definition of the duty ratio, $r{=}1/N_{\rm min}$, that relates it to the minimum number of molecular motor heads, $N_{\rm min}$, needed for continuous processive movement, suggests that at least 9 motor heads or 5 two-headed kinesin motors are needed. That 5 motors can be attached to a cargo and collaborate is supported by the *in vivo* experiments by Sthridelman et al. [25]. Their experiments suggest that the cargoes in NT2 cells are carried by 1-5 molecular motors.

Conclusion

In this thesis we try to explain the physical phenomena of cytoplasmic and axoplasmic streaming where many organelles are carried simultaneously through a viscous medium. The above discussion of velocities, forces and ATPase showed that the maximum values that were found in the simulations are large with respect to the single motor values. However, experiments reported in literature reported values that were similar or, in the case of myosin, much larger. From this can firstly be concluded that the observed velocities lie within the physical limits of the motors.

Secondly, for the motors to generate the forces needed to move at these velocities two mechanisms need to be considered: (1) hydrodynamic interactions between the molecular motors via the surrounding medium and (2) cooperation between motors that are attached to the same cargo. We have shown both by means of simulations (chapters 4 and 6) and experiments (chapter 5) of an ordered system, that the momentum transfer through the surrounding medium affects both the motion of the bound and suspended motors. The momentum transfer via the fluid can be seen as an additional positive force that pushes the organelles forward.

---

[*] For each motor: ATPase=50 s^{-1}head^{-1}, $V{=}3.5\mu m/s$, $\delta{=}0.8$

There is physical evidence that multiple molecular motors can be attached to an organelle at the same time [28, 29] but there is no consensus in literature if, and how, these motors collaborate. There are experiments that suggest that a set of identical motors attached to the same cargo can work together [25, 31, 41, 42] or that motors of different properties are present at the same time [43, 206]. In addition, organelles that change direction on their cytoskeletal track have been reported where motors with opposite directionality are present and a protein complex called dynactin is suspected to regulate the switching between both motors [207]. A tug-of-war between motors has been reported to be unlikely as impairment of one of the two motors does not increase the transport in the opposite direction [208]. Cooperation between motors on a cargo could help motors overcome the large friction forces in the cytosol by load sharing, increase the processivity and explain the large ATPase needed for fast organelle transport. However, motor cooperation alone cannot explain the observed directed transport of suspended organelles. Thus, hydrodynamic interactions are necessary to reach the velocities that are observed in phenomena such as cytoplasmic or axoplasmic streaming motor while motor cooperation may be needed. More research is necessary to answer this question.

Chapter 7

Outlook

Introduction

This chapter serves to provide the reader with a potential extension of the work presented in previous chapters. In this thesis a plausible explanation was given for the biological phenomena cytoplasmic and axoplasmic streaming. The results presented in chapters 4, 5 and 6 suggest that the actively transported organelles set up a non-negligible flow in the surrounding medium capable of displacing suspended objects in an otherwise quiescent fluid. So far only translational hydrodynamic interactions in planar geometries have been studied. It can be expected that the same mechanism yields alternative types of flow in different geometries. Indeed, in chapter 3[*] experiments [96, 98] and simulations [97] were discussed of particles moving on a Brownian ratchet in a toroidal trap. These studies showed that hydrodynamic interactions between the particles make these particles move faster along their rotational trajectory thus setting up a rotational flow field. Moreover, Goldstein et al. [209] showed that a complex flow field appears in cytoplasmic streaming of algal species such as *Chara* and *Nitella*. Here motors carry cargoes along actin filaments that are attached to the cylindrical cell wall. The filaments are arranged in two spiralling bands of opposite polarity[†], thereby allowing for simultaneous transport in opposite directions. The arising flow field consists of two components: Firstly, a component parallel to the spiral, and secondly, flow perpendicular to the spiral in radial direction. The combination of both gives rise to rotational flow and allows for fluid mixing.

In the review of Shimmen on cytoplasmic streaming [6] reference was made to experiments by Kuroda and Shimmen. These authors prepared a cytoplasmic drop in which chloroplasts were rotating in absence of external forces. Shimmen mentions that the rotational motion is thought to be driven by the same mechanism as cytoplasmic

---

[*] See section 'Brownian Ratchets Featuring Hydrodynamic Interactions'.

[†] Similar to the red and white bands of a barber pole.

streaming. Without knowledge of the details of the biological system or the physics that drive the chloroplasts, I would like to suggest answering a related question: is it possible for molecular motors, that are carrying cargoes while walking along the surface of a spherical object, to transfer enough momentum through the fluid for this object to start rotating? To study this effect the theory of translational hydrodynamic interactions that was discussed in chapter 2 has to be expanded with rotational interactions.

In the sections below the theory on hydrodynamic interactions is expanded by introducing rotational hydrodynamic interactions. Moreover, a model is proposed that could be used for testing the hypothesis that molecular motors can make an object rotate via hydrodynamic interactions. This work is accessible to both simulations and experiments. Finally, possible applications for microfluidic devices are discussed.

Rotational Hydrodynamic Interactions

In chapter 2 the Langevin Equation was introduced for interacting organelles (eq.2.43). This equation includes the hydrodynamic interactions between the organelles. The latter is included to account for the momentum that is transferred into the cytosol by the actively transported organelles. It is possible, by means of a hydrodynamic interaction tensor, to solve the flow field that arises from this transport. For example, assuming that the active organelles are treated as point particles, the arising flow field (eq.2.23) can be solved using the Oseen tensor (eq.2.25), that only includes long-range interactions. In addition, a description for the flow field that includes the size of the organelles, short and long range interactions is found using the Rotne-Prager tensor (eq.4.10). In the theory in chapter 2 only translational motion has been considered and rotational motion has been neglected. However, if an organelle is under influence of an external torque, $\boldsymbol{T}$, it will rotate with constant angular velocity, $\boldsymbol{\omega}$, and subsequently, via molecular momentum transfer, set up a flow field. The magnitude of this rotational flow field, $\acute{\boldsymbol{V}}^{\mathrm{r}}$, is given by [66,155]:

$$\acute{\boldsymbol{V}}^{\mathrm{r}} = \left(\frac{a}{r}\right)^3 \boldsymbol{\omega} \times \boldsymbol{r}. \tag{7.1}$$

The required torque for an organelle i to overcome the fluid friction and maintain rotation is given by the equation below [57]:

$$\boldsymbol{T}_{\mathrm{i}} = 8\pi\eta a^3 \boldsymbol{\omega}_{\mathrm{i}} = \frac{1}{\mu_0^{\mathrm{r}}} \boldsymbol{\omega}_{\mathrm{i}}. \tag{7.2}$$

In this equation, the constant of proportionality is the rotational self-mobility μ_0^{r}. The solution of the flow fields governed by momentum transport in both translational (superscript t) and rotational (superscript r) directions can be expressed as a combination of forces, torques and a mobility tensor. Ignoring thermal fluctuations, the following equations for the translational and rotational velocities, can be written for the interactions between an organelle i and all other organelles j [154,155]:

$$\boldsymbol{V}_{\mathrm{i}} = \boldsymbol{\mu}^{\mathrm{tt}}_{\mathrm{ii}} \cdot \boldsymbol{F}_{\mathrm{i}} + \sum_{\mathrm{j,j \neq i}} \boldsymbol{\mu}^{\mathrm{tt}}_{\mathrm{ij}} \cdot \boldsymbol{F}_{\mathrm{j}} + \boldsymbol{\mu}^{\mathrm{tr}}_{\mathrm{ii}} \cdot \boldsymbol{T}_{\mathrm{i}} + \sum_{\mathrm{j,j \neq i}} \boldsymbol{\mu}^{\mathrm{tr}}_{\mathrm{ij}} \cdot \boldsymbol{T}_{\mathrm{j}} \tag{7.3}$$

and

$$\boldsymbol{\omega}_{\mathrm{i}} = \boldsymbol{\mu}^{\mathrm{rt}}_{\mathrm{ii}} \cdot \boldsymbol{F}_{\mathrm{i}} + \sum_{\mathrm{j,j \neq i}} \boldsymbol{\mu}^{\mathrm{rt}}_{\mathrm{ij}} \cdot \boldsymbol{F}_{\mathrm{j}} + \boldsymbol{\mu}^{\mathrm{rr}}_{\mathrm{ii}} \cdot \boldsymbol{T}_{\mathrm{i}} + \sum_{\mathrm{j,j \neq i}} \boldsymbol{\mu}^{\mathrm{rr}}_{\mathrm{ij}} \cdot \boldsymbol{T}_{\mathrm{j}}. \tag{7.4}$$

Note that the mobility tensor consists of translational (superscript tt), rotational (rr), and combined components (tr and rt). It is possible to write these equations more concisely via introduction of a velocity, $\boldsymbol{v} = [\boldsymbol{V}_1, \ldots, \boldsymbol{V}_{\mathrm{N}}, \boldsymbol{\omega}_1, \ldots, \boldsymbol{\omega}_{\mathrm{N}}]$, and a force vector $\boldsymbol{f} = [\boldsymbol{F}_1, \ldots, \boldsymbol{F}_{\mathrm{N}}, \boldsymbol{T}_1, \ldots, \boldsymbol{T}_{\mathrm{N}}]$. This yields [155]:

$$\boldsymbol{v} = \boldsymbol{M} \cdot \boldsymbol{f}. \tag{7.5}$$

In this equation, the generalised mobility matrix, $\boldsymbol{M}$, is introduced that consists of sets of 3×3 Cartesian mobility tensors. It is defined as [155]:

$$\boldsymbol{M} = \begin{bmatrix} \boldsymbol{\mu}^{\mathrm{tt}} & \boldsymbol{\mu}^{\mathrm{tr}} \\ \boldsymbol{\mu}^{\mathrm{rt}} & \boldsymbol{\mu}^{\mathrm{rr}} \end{bmatrix} = \begin{bmatrix} \boldsymbol{\mu}^{\mathrm{tt}}_{11} & \cdots & \boldsymbol{\mu}^{\mathrm{tt}}_{1\mathrm{N}} & \boldsymbol{\mu}^{\mathrm{tr}}_{11} & \cdots & \boldsymbol{\mu}^{\mathrm{tr}}_{1\mathrm{N}} \\ \vdots & \ddots & \vdots & \vdots & \ddots & \vdots \\ \boldsymbol{\mu}^{\mathrm{tt}}_{\mathrm{N}1} & \cdots & \boldsymbol{\mu}^{\mathrm{tt}}_{\mathrm{NN}} & \boldsymbol{\mu}^{\mathrm{tr}}_{\mathrm{N}1} & \cdots & \boldsymbol{\mu}^{\mathrm{tr}}_{\mathrm{NN}} \\ \\ \boldsymbol{\mu}^{\mathrm{rt}}_{11} & \cdots & \boldsymbol{\mu}^{\mathrm{rt}}_{1\mathrm{N}} & \boldsymbol{\mu}^{\mathrm{rr}}_{11} & \cdots & \boldsymbol{\mu}^{\mathrm{rr}}_{1\mathrm{N}} \\ \vdots & \ddots & \vdots & \vdots & \ddots & \vdots \\ \boldsymbol{\mu}^{\mathrm{rt}}_{\mathrm{N}1} & \cdots & \boldsymbol{\mu}^{\mathrm{rt}}_{\mathrm{NN}} & \boldsymbol{\mu}^{\mathrm{rr}}_{\mathrm{N}1} & \cdots & \boldsymbol{\mu}^{\mathrm{rr}}_{\mathrm{NN}} \end{bmatrix} \tag{7.6}$$

This matrix is square, symmetrical and positive definite[*] [154,155], thus $\boldsymbol{M} = \boldsymbol{M}^T$. Moreover, the generalised Einstein relation holds, in which, $\boldsymbol{D}$, is the diffusivity matrix:

$$\boldsymbol{D} = k_{\mathrm{b}} T \boldsymbol{M}. \tag{7.7}$$

Analogous to eq.2.41, the diffusivity matrix is a 3-dimensional position dependent tensor. The elements of the generalised mobility matrix (eq.7.6) can be solved using the Rotne-Prager approximation[†]. The latter yields a solution for the different mobility tensors that is accurate up to $(a/r_{\mathrm{ij}})^3$ and the components of this matrix are given as [155][‡]:

---

[*] A positive definite matrix requires that the following inequalities hold: $\boldsymbol{\mu}^{\mathrm{tt}} > 0$, $\boldsymbol{\mu}^{\mathrm{rr}} > 0$ and $\det \boldsymbol{M} = \boldsymbol{\mu}^{\mathrm{tt}} \boldsymbol{\mu}^{\mathrm{rr}} - (\boldsymbol{\mu}^{\mathrm{rt}})^2 > 0$ [154].

[†] This approximation includes the Rotne-Prager tensor given by eq.4.10.

[‡] An alternative method for calculating the elements can be found in [210,211].

$$
\begin{aligned}
\boldsymbol{\mu}_{\mathrm{ij}}^{\mathrm{tt}} &= \begin{cases} \hat{\mathbf{I}}\mu_0^{\mathrm{t}} & \\ \frac{3}{4}\mu_0^{\mathrm{t}}\frac{a}{r_{\mathrm{ij}}}\left(\hat{\mathbf{I}}+\hat{\boldsymbol{r}}_{\mathrm{ij}}\hat{\boldsymbol{r}}_{\mathrm{ij}}\right)+\frac{1}{2}\mu_0^{\mathrm{t}}\left(\frac{a}{r_{\mathrm{ij}}}\right)^3\left(\hat{\mathbf{I}}-3\hat{\boldsymbol{r}}_{\mathrm{ij}}\hat{\boldsymbol{r}}_{\mathrm{ij}}\right) & \mathrm{i}\neq\mathrm{j} \end{cases} \\
\boldsymbol{\mu}_{\mathrm{ij}}^{\mathrm{rr}} &= \begin{cases} \hat{\mathbf{I}}\mu_0^{\mathrm{r}} & \\ -\frac{1}{2}\mu_0^{\mathrm{r}}\left(\frac{a}{r_{\mathrm{ij}}}\right)^3\left(\hat{\mathbf{I}}-3\hat{\boldsymbol{r}}_{\mathrm{ij}}\hat{\boldsymbol{r}}_{\mathrm{ij}}\right) & \mathrm{i}\neq\mathrm{j} \end{cases} \\
\boldsymbol{\mu}_{\mathrm{ij}}^{\mathrm{tr}} = \boldsymbol{\mu}_{\mathrm{ij}}^{\mathrm{rt}} &= \begin{cases} \mathbf{0} & \\ \mu_0^{\mathrm{r}}a\left(\frac{a}{r_{\mathrm{ij}}}\right)^2\hat{\boldsymbol{r}}_{\mathrm{ij}}\times & \mathrm{i}\neq\mathrm{j} \end{cases}
\end{aligned}
\tag{7.8}
$$

Adding thermal noise to eq.7.5, yields the following Langevin equation for the system [146, 212](compare with eq.2.42):

$$
\boldsymbol{v} = \frac{\mathrm{d}\boldsymbol{X}}{\mathrm{d}t} = \boldsymbol{M}\cdot\boldsymbol{f} + k_{\mathrm{b}}T(\nabla\cdot\boldsymbol{M}) + \boldsymbol{g}(t). \tag{7.9}
$$

In this Equation, $\boldsymbol{X}$, refers to the position of the organelle. As the elements of the mobility matrix, $\boldsymbol{M}$, are position dependent, thermal fluctuations can result in additional drift terms. This is compensated for by including the drift term $k_{\mathrm{b}}T(\nabla\cdot\boldsymbol{M})$ [146, 212]. The mean and variance of the thermal fluctuations acting upon the organelles are given by [145, 146]:

$$
\begin{aligned}
\langle\boldsymbol{g}(t)\rangle &= \mathbf{0} \\
\langle\boldsymbol{g}(t)\boldsymbol{g}(t^{'})\rangle &= 2k_{\mathrm{b}}T\boldsymbol{M}\delta(t-t^{'}).
\end{aligned}
\tag{7.10}
$$

The thermal forces exhibit a correlated diffusion as the generalised mobility matrix depends upon the organelle positions in the system. The Ermak and McCammon algorithm [72], (see chapter 4), can be used to generate the correlated thermal fluctuations. Next, the Langevin equation is integrated from time t to $t+\Delta t$ and discretized with respect to time to yield the following equation that can be solved using computer simulations [146]:

$$
\Delta\boldsymbol{X}_{\mathrm{t}} = (\boldsymbol{M}\cdot\boldsymbol{f})\Delta t + k_{\mathrm{b}}T(\nabla\cdot\boldsymbol{M})\Delta t + \boldsymbol{g}(\Delta t). \tag{7.11}
$$

In the above equation $\boldsymbol{g}(\Delta t)$ has identical statistical properties to $\boldsymbol{g}(t)$ (see eq.7.10) [146]. The spurious drift term, $k_{\mathrm{b}}T(\nabla\cdot\boldsymbol{M})$, vanishes since at Rotne-Prager level only two-body interactions are taken into account i.e. $(\nabla\cdot\boldsymbol{M}) = 0$ [155]. This simplifies the equation to:

$$
\Delta\boldsymbol{X}_{\mathrm{t}} = (\boldsymbol{M}\cdot\boldsymbol{f})\Delta t + \boldsymbol{g}(\Delta t). \tag{7.12}
$$

This Langevin equation can be used to calculate the trajectories of interacting organelles taking both translational and rotational hydrodynamic interactions into account.

The Model

The stochastic Langevin equation (eq.7.12) can subsequently be used to solve the model shown in Fig.7.1. In this system a hollow or solid bead is suspended in an otherwise quiescent fluid with a viscosity similar to cytosol (≈1 Pas). The latter is important to maximise the hydrodynamic coupling between the organelles and between the organelles and the bead. The organelles and the bead are subject to thermal fluctuations but other external forces such as gravity can be neglected (see chapter 2). The molecular motors with cargoes walk along the cytoskeleton in unidirectional direction. On each organelle acts a net driving force, but it is assumed that the organelles do not rotate i.e. the external torque on each organelle is zero. Thus, the velocity of any organelle, i, in the Langevin equation (eq.7.12) depends on the force acting upon it, the hydrodynamic coupling via the forces acting upon all other organelles, j, plus momentum transfer from the torque on the bead. The bead has no net external force or torque acting upon it, its rotation is purely driven by the momentum transferred via the fluid. However, as mentioned above, when it rotates it will influence the velocities of the organelles.

Using computer simulations the following questions can be answered:

- Is this a plausible mechanism to make the bead rotate?
- What minimum motor density (required energy) is necessary to make the bead rotate?
- Is there a relation to be found between the organelle size, mass, and the motor density?

Experiments

The predictions from the computer simulations can subsequently be tested in an experimental set-up. For this purpose a bead of a convenient material for experiments can be etched with parallel tracks that span all the way around the sphere. Next, these tracks can be lined with cytoskeletal elements using one of the techniques described in literature for microfluidic devices [213–216]. The motor-cargo complexes can be added to the system in the form of bead assays i.e. as micrometer scale beads coated with molecular motors [3]. Previous chapters showed that the hydrodynamic coupling is strongest

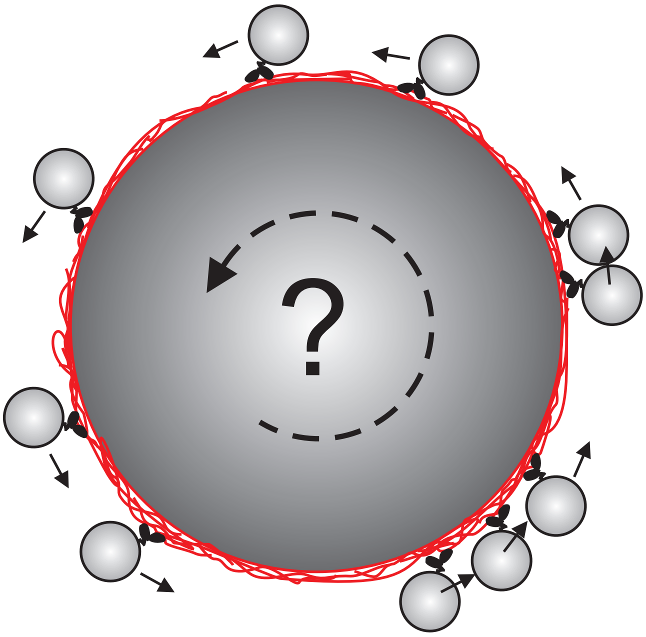

Figure 7.1: *A bead is suspended in a quiescent fluid and is covered with parallel cytoskeletal tracks that span the whole bead. Molecular motors with cargoes walk in unidirectional fashion along the filaments. Does the combined momentum transfer from the active transport make the sphere rotate?*

in viscous fluids such as cytosol. One possible fluid with a viscosity of 1 Pas* is *Xanthan* [45]. It has been shown that using this water-soluble bacterial exopolysaccharide increases the cargo velocity in gliding assays [45]. The experiments could confirm the validity of the hypothesis and give a possible explanation for cytoplast rotation.

Applications For Microfluidic Devices

Recently, many papers have been dedicated to research of microfluidic devices (see reviews [213–216]), which are nanoscale systems that are inspired by cell biology. In these synthetic structures molecular motors are used as a power source to create a mechanical force for either autonomous transport of cargoes and/or for actuation of other processes†. Possible applications are sorting, separation, purification and assembly of materials [216]. In most systems the molecular motors are used in the configuration of a gliding or bead assay. It is possible to guide the motor-cargo complexes directly using the surface of the chip by mechanical confinement in designed channels, selective pat-

---

[*] At a concentration of 2 mg/ml, $M_\mathrm{w} = 1 \times 10^6 - 7 \times 10^6$.

[†] Similarly, artificial cilia are studied to create pumping and/or mixing in microfluidic devices [217].

terning of the surface with motors or filaments or by a combination of both [214]. Additionally it is possible to steer via external stimuli [213,216] such as electrical fields [218], magnetic fields [219] and flow fields [220]. The latter is important for this thesis as the flow fields considered were driven by an external force or a gradient. We propose the via hydrodynamic interactions it is possible to generate a flow field locally by using hydrodynamic interactions between the cargoes. This novel idea might well give rise to a whole new range of applications.

The results presented in this thesis could directly be applied to work presented by Bull et al. [221]. The authors performed simulations of a microfluidic pump. The pump consisted of an annular channel of which the surface was coated with molecular motors. The molecular motors where aligned in unidirectional fashion. Through the channel a single bead was actively transported (gliding assay). The simulations showed that the microfluidic pump produces a flow in the range of 10^{-18}–10^{-12} l/s. The fluid used in the system was water. This result could be improved by increasing the number of beads in the system although this effect would be larger in a more viscous environment.

Appendix A

Dynamics Of The Lattice Model

The bio-filament

In the work of Lipowsky et al [129, 130], the bound motors, are driven along the bio-filament that is defined as an ASEP model (see chapter 3), by imposing a biased diffusion upon them. The velocity, $\boldsymbol{V}_0$, of a single motor is given by the degree of bias. The latter is the difference between the rate to step forward α and backward β and is given by:

$$\boldsymbol{V}_0 = (\alpha - \beta)\, l\hat{\boldsymbol{n}}. \tag{A.1}$$

In the equation above, l, is the lattice spacing, which is typically the size of a motor-organelle complex and, $\hat{\mathbf{n}}$, a normal vector. Typically, more than one motor will be attached to the bio-filament. Thus, similar to traffic on a highway, the motor velocity will depend on the amount of traffic it encounters. The more traffic on the road, the slower cars will move or alternatively the more free space, $(1 - \phi_\mu)$, on the bio-filament, the faster molecular motors walk. Assuming a homogeneous distribution, the velocity of a motor, i, can be estimated:

$$\boldsymbol{V}_{\mathrm{i}} = \boldsymbol{V}_0\,(1 - \phi_\mu)\,. \tag{A.2}$$

This equation predicts a linear velocity decrease with increasing motor density. Similarly, the flux of bound motors, $\boldsymbol{J}_{\mathrm{i}}$, is given by:

$$\boldsymbol{J}_{\mathrm{i}} = \boldsymbol{V}_{\mathrm{i}}\phi_\mu = \boldsymbol{V}_0\,(1 - \phi_\mu)\, l\phi_\mu. \tag{A.3}$$

The equation predicts a maximal flux of motors at an occupation fraction of $\phi_\mu = 0.5$, which yields: $\boldsymbol{J}_{\mathrm{i,max}} = 0.25\boldsymbol{V}_0$. At smaller volume fractions the flux is low due to the small number of motors in the system. At higher values, more motors are present, but their flux is limited by excluded volume interactions. The above equations are well known results from traffic-jam models [222,223].

As mentioned in chapter 1 different types of molecular motors exist. Each motor operates with its particular velocity, processivity and preferred walking direction. The model allows for modelling the different types by changing the degree of bias and the detachment probability. In addition, the polarity of the bio-filament can be reversed by interchanging the values of α and β (for plus or minus-end motors).

Langmuir Kinetics

The flux of motors detaching from the bio-filament and motors attaching to the filament can be used to estimate the bound motor number density, ϕ_μ. This is described by the following equation:

$$\begin{aligned} \text{Particle flux out} &= \text{Particle flux in} \\ \phi_\mu \left(1-\phi_\mathrm{s}\right)\gamma_\mathrm{d} &= p\phi_\mathrm{s}\left(1-\phi_\mu\right)\gamma_\mathrm{a} \\ \phi_\mu &= \frac{1}{1+\frac{\gamma_\mathrm{d}(1-\phi_\mathrm{s})}{p\gamma_\mathrm{a}\phi_\mathrm{s}}}. \end{aligned} \tag{A.4}$$

Where, ϕ_s, is the number density in solution, γ_d and γ_a the rates of respectively detachment and attachment and, p, the probability that a motor in solution diffuses towards the bio-filament. This probability depends upon the geometry of the system and, in case of a lattice model, on the lattice connectivity. For example, in the described lattice model the organelles are moving on a simple cubic lattice. Thus, for an organelle that is located on a lattice node adjacent to a filament, the probability for moving towards the filament (and attach to it) is, $p = 1/2s$. In the latter equation, s, is the number of dimensions in the system.

Appendix B

Spurious Effects On The Lattice

Spurious Effects

The motion of a single molecular motor bound to the cytoskeleton can be described via a biased diffusion. This is a combination of a driving velocity component derived from hydrolysing ATP, $\boldsymbol{V}_0{=}(V_0, 0, 0)$, and a diffusive component, $\boldsymbol{g}_{\mathrm{i}}$. The motor velocity, $\boldsymbol{V}_{\mathrm{i}}$, is given by:

$$\boldsymbol{V}_{\mathrm{i}} = \boldsymbol{V}_0 + \boldsymbol{g}_{\mathrm{i}} = \boldsymbol{\mu}_{\mathrm{ii}} \cdot \boldsymbol{F}_0 + \boldsymbol{g}_{\mathrm{i}}. \tag{B.1}$$

In this equation, $\boldsymbol{\mu}_{\mathrm{ii}} = \mu_0 \hat{\mathbf{I}}$, is the motor mobility with magnitude μ_0 and $\hat{\mathbf{I}}$ is an identity matrix, $\boldsymbol{F}_0 = (F_0, 0, 0)$, is the force generated while a molecular motor hydrolyses ATP and the diffusive component, $\boldsymbol{g}_{\mathrm{i}}$, has the following mean and variance:

$$\begin{aligned} \langle \boldsymbol{g}_{\mathrm{i}}(t) \rangle &= \mathbf{0} \\ \langle \boldsymbol{g}_{\mathrm{i}}(t) \boldsymbol{g}_{\mathrm{j}}(t^{'}) \rangle &= 2\boldsymbol{D}_{\mathrm{ij}} \delta(t - t^{'}) = 2k_{\mathrm{b}} T \boldsymbol{\mu}_{\mathrm{ij}} \delta(t - t^{'}). \end{aligned} \tag{B.2}$$

Note that the hydrodynamic interaction contribution of the Langevin equation (see eq.4.1) is absent from equation B.1 as a motor exerts no hydrodynamic interactions on itself. In the d-lattice model that is used in chapter 4, the motor positions and displacements are restricted to lattice positions. During one simulation time step the motors are allowed to make a move of either zero (dwell), ±1 or ±2 lattice nodes in both x and y directions. To be able to map the Langevin equation on the lattice, the simulation parameters (see table 4.1 in chapter 4) are tuned to be of order one. A velocity that is too small would not utilise the full span of the mapping algorithm and a too large velocity would only trigger steps of maximum value. Moreover, the thermal energy has to be large enough to be able to reach the full displacement range of ±2 lattice nodes. In order to map equation B.1 on the lattice, the algorithm in Fig.B.1 is used (see chapter 4*).

---

*In the section: 'Allowing For Larger Displacements'.

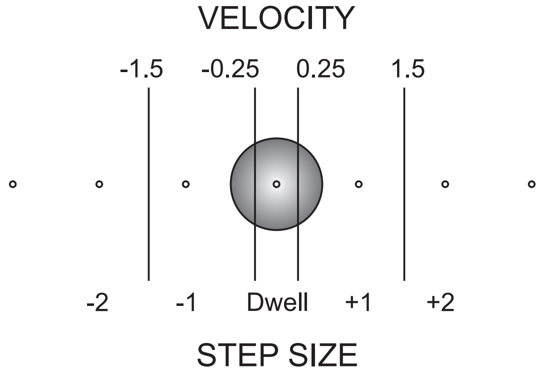

Figure B.1: *Mapping of calculated motor displacements on the lattice. Small displacements, $-0.25l < \Delta x < 0.25l$ will cause the motor to dwell in its current position. Intermediate displacements, $0.25l \leq |\Delta x| \leq 1.5l$, will be mapped on the adjacent lattice node. Large steps, $|\Delta x| \geq 1.5l$ will be mapped on the second neighbour node.*

However, an unwanted side effect of mapping the shifted Gaussian distribution (eq.B.1[*]) on a lattice, is the appearance of spurious dynamics. This results in velocities that deviate from the expected (mean) value. Including the spurious effects, $\boldsymbol{\varepsilon}$, into eq.B.1 yields:

$$\boldsymbol{V}_{\mathrm{i}} = \boldsymbol{V}_0 + \boldsymbol{g}_{\mathrm{i}} + \boldsymbol{\varepsilon} = \langle \boldsymbol{V}_0 \rangle + \boldsymbol{g}_{\mathrm{i}}. \tag{B.3}$$

In this equation, the effective single motor velocity is given by:

$$\langle \boldsymbol{V}_0 \rangle = \boldsymbol{V}_0 + \boldsymbol{\varepsilon}. \tag{B.4}$$

The spurious effects can be understood by means of Fig.B.2. In the absence of a net motor force, i.e. V_0=0, the Gaussian velocity distribution is symmetrical around zero (see Fig.B.2A) and it crosses the threshold values (±0.25 and ±1.5 in Fig.B.1) for stepping forward or back with equal probability. Thus, for the simulation parameters that were determined in Table 4.1 in chapter 4, the mapping algorithm yields the expected average velocity of $\langle V_{\mathrm{i}} \rangle$=$\langle g_{\mathrm{i}}(t) \rangle$=0.

However, as molecular motors can derive motion from hydrolysing ATP, the position of the average velocity is shifted corresponding to the single motor velocity, V_0, but the mapping algorithm remains the same. For example, in Fig.B.2B, the nominal motor velocity is V_0=0.2. The velocity mapping at this point is no longer symmetrical around the average velocity, thus random velocity deviations, g_{i}, in either positive or negative direction have different effects that on average do not cancel each other out. As in Fig.B.2B V_0 is close to the threshold (0.25), a small random displacement towards the

---

[*] The mean value is V_0.

threshold value suffices to cross it, whereas a small displacement in opposite direction of equal size will not yield a displacement. This results in an over or underestimation of the measured single motor velocity $\langle V_0 \rangle$. For V_0=0.2 this leads to an overestimation of the velocity. As shown in Fig.B.3A and B, this overestimation decreases with increasing mobility, μ_0, and V_0. The mobility is a measure for the variance of the Gaussian velocity distribution. Therefore, the larger the mobility[*], the broader the distribution (see eq.B.2). This improves the mapping on the lattice, as it effectively decreases the effect of the shift of the distribution's mean and increases the probability for crossing the established thresholds in both positive and negative direction. The effect of increasing V_0, is shown in Fig.B.2C. The figure shows that choosing the motor velocity further away from the threshold at 0.25 decreases the spurious effects and approximately yields the single motor velocity. This is confirmed in Fig.B.3B, where the normalised single motor velocity is shown for different V_0. However, when V_0 approaches the next threshold at 1.5, the spurious lattice effect causes an underestimation of the velocity.

Fig.B.3C shows that the results from Fig.B.3A-B, are recovered when multiple motors are present in the system. Similar to the single motor data, the spurious effects increase with V_0 and μ_0. In addition, the spurious dynamics increase with the motor concentration until they reach a maximum at ϕ_μ=50%. The filament is modelled as an ASEP[†], where excluded volume is taken into account, and the motors predominantly walk in a forward direction. It is therefore more likely for a motor to collide with another motor when moving backward, against the direction of flow, than for moving forward. This means that, even though the mapping for multiple motors is calculated in the same way as for a single motor, the excluded volume effects in the system will not allow for every (trial) move. For increasing concentrations up to ϕ_μ=50% this effectively changes the shape of the velocity distribution as back stepping becomes less likely due to excluded volume effects. In the forward direction the effect will be less relevant as, on average, all motors walk in the same direction and the next lattice node is more likely to be free. However, at filament occupations beyond ϕ_μ=50% the average motor-motor separations become very small[‡]. Above ϕ_μ=50% displacements of ± 2 become less probable because of space constraints. The magnitude of the spurious velocity increase is shown for different occupation fractions in Fig.B.3D. In this figure the spurious velocity deviation ($\langle V_0 \rangle$ minus the theoretical velocity for an ASEP model (eq.A.2)) is normalised using $\langle V_0 \rangle$. For the simulation settings that were used in chapter 4 to investigate hydrodynamic interactions (V_0=0.4, μ_0=0.3769) the normalised spurious deviation, is found

---

[*] At constant $k_\mathrm{b}T$.

[†] This is a modified ASEP that allows for motor detachment from and attachment to the filament via Langmuir Kinetics. Moreover, the original model only allows for steps of ± 1 lattice nodes per time step (see chapter 3).

[‡] Assuming a homogeneous motor distributed along the bio-filament the free space between 2 motors can be calculated via: $x = \frac{(1-\phi_\mu)}{2\phi_\mu}$ (in lattice spacings l).

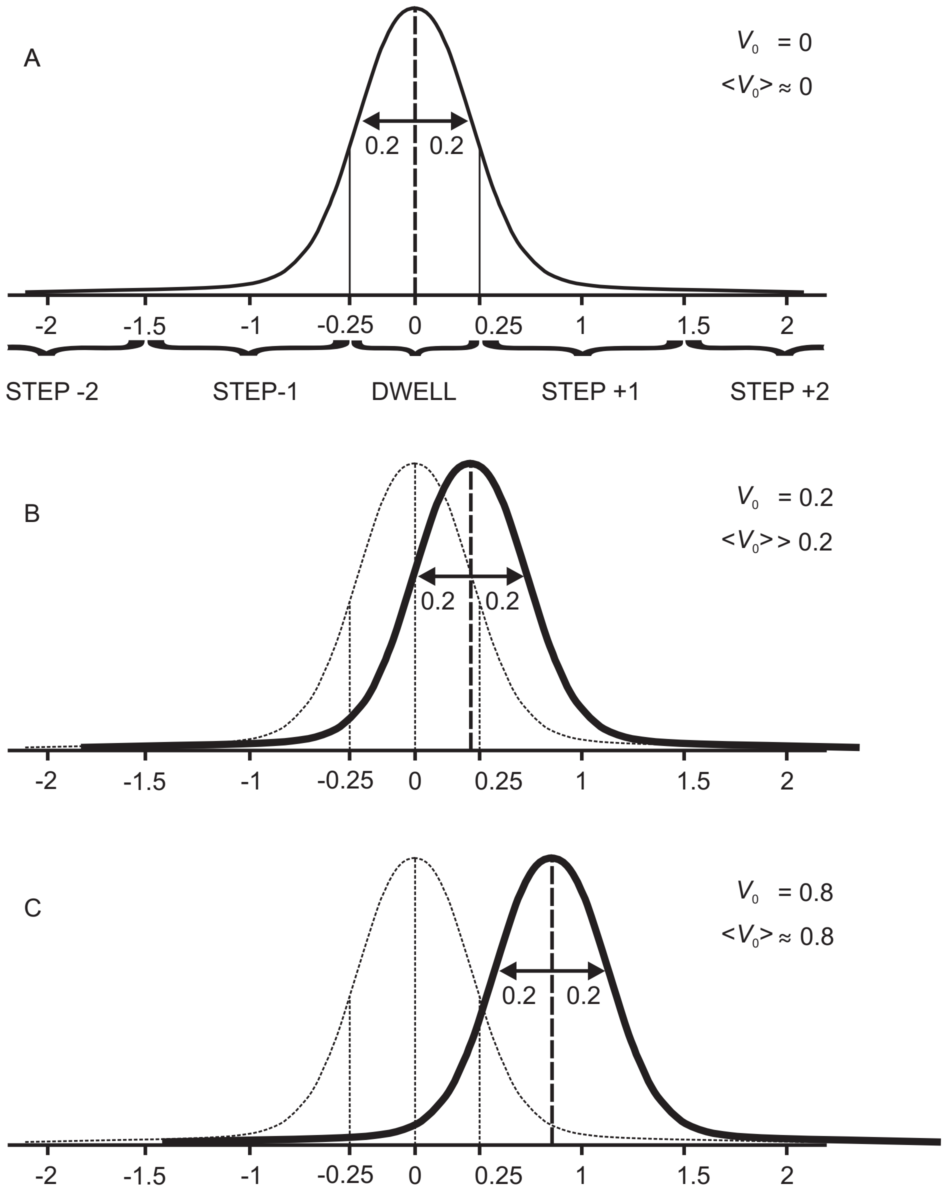

Figure B.2: *A) Mapping of the single motor velocity distribution on the lattice in the absence of a net external force (V_0=0). The measured velocity $\langle V_0 \rangle$ corresponds to the nominal velocity. B) A Single motor moving with a velocity (V_0=0.2) close to the threshold value, for a move of $+1$ lattice node, yields a measured velocity larger than the theoretical velocity.* C) *The deviation of the single motor velocity from the nominal velocity decreases with increasing V_0.*

to have a maximum value of 0.05 for ϕ_μ=50%. This value is small with respect to the velocity increase via hydrodynamic interactions (compare with Fig.4.5A).

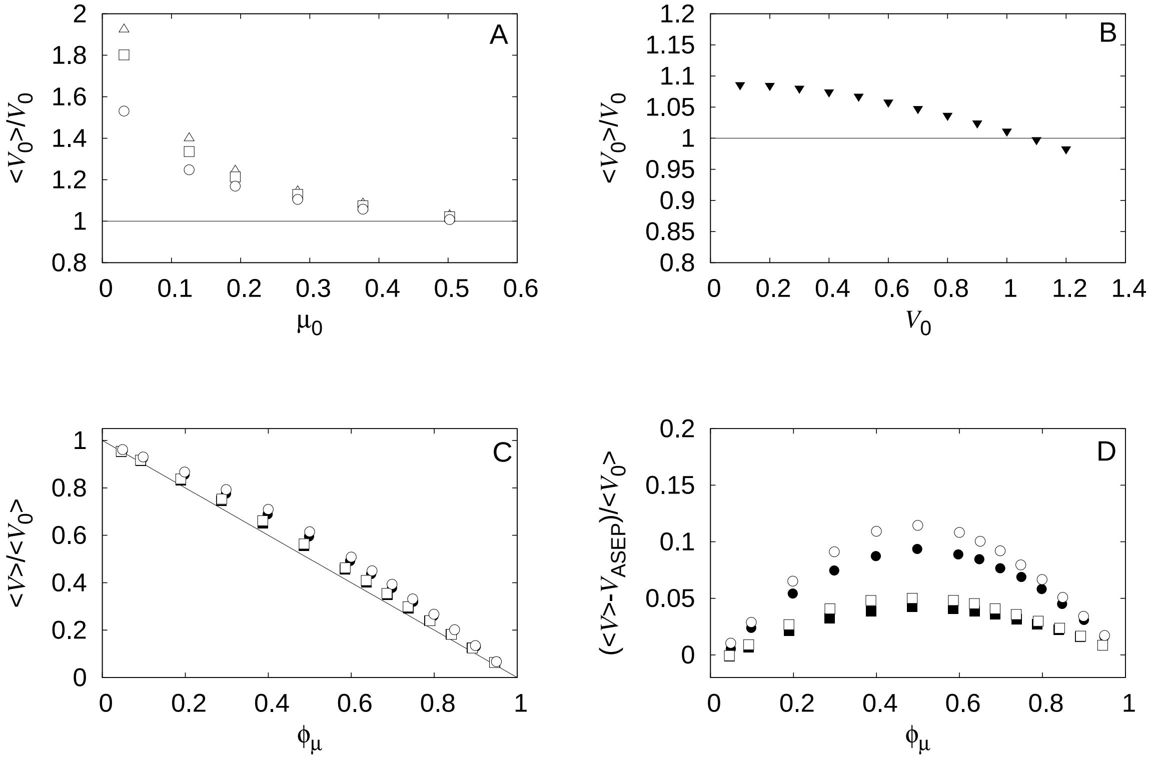

Figure B.3: A) Measured single motor velocity $\langle V_0 \rangle$ divided by the theoretical motor velocity, V_0, for different μ_0. Open triangles - V_0=0.2; Open squares - V_0=0.4; Open circles - V_0=0.6; B) Normalised single motor velocity for different values of the nominal velocity V_0; μ_0=0.3769 and F_0=$n \times 0.26525$ (with $n = 1, 2, \ldots, 12$). Figures A-B: N_{part}=1 and T_{max}=10^8. C) Normalised velocity for different degrees of bio-filament occupation. The line represents the theoretical ASEP velocity (eq.A.2). D) Measured velocity minus ASEP velocity divided by $\langle V_0 \rangle$. Figures C-D: Squares V_0=0.4; Closed squares $\langle V_0 \rangle$=0.43; Open Squares $\langle V_0 \rangle$=0.49; Circles V_0=0.6; Closed circles $\langle V_0 \rangle$=0.63; Open circles $\langle V_0 \rangle$=0.70; Squares, μ_0=0.3769; Circles, μ_0=0.1923; $N_{\mathrm{part}} \approx 1000$, T_{max}=10000.

Discussion

Spurious lattice effects will appear when an symmetrical (around zero) mapping algorithm is used in combination with a shifted Gaussian distribution with finite mean. For a single motor, the magnitude of this effect can be controlled by ensuring that the variance of the distribution is large enough to sample the full mapping range. Moreover, choosing the velocity further away from the mapping thresholds minimises the spurious effects. In addition, spurious dynamics effectively modify the variance of the distribution causing a small over or underestimation of the motor velocity. When multiple motors are present in the system, excluded volume effects influence the magnitude of the spurious effects. This causes larger deviations with increasing filament occupation fraction with a maximum value at filament ϕ_μ=50%. The magnitude of the spurious dynamics are smaller than the magnitude of the motor velocity increase due to hydrodynamic interactions.

Appendix C

Material and Methods of Chapter 5

Introduction

What follows is the experimental procedure followed by Agnieszka Esseling-Ozdoba who did her research in the group of prof. dr. A.M.C. Emons at Wageningen Universiteit. See more more details [150, 162]. Copyright 2013 Wiley. Used with permission from Esseling-Ozdoba et al., Hydrodynamic flow in the cytoplasm of plant cells, *Journal of Microscopy, Blackwell Publishing Ltd*, 2008, 231, 274-283 [150].

Plant material

Tobacco Bright Yellow - 2 (BY-2) suspension cells expressing cytoplasmic GFP (stably transformed with plasmid pBin-35S-smGFP) were used for experiments. Suspension cultures were grown in standard BY-2 medium containing Murashige and Skoog macro- and microsalts, 3% sucrose, 100 mg/l myo-inositol, 200 mg/l $\mathrm{KH_2PO_4}$, 1 mg/l thiamine, and 0.2 μg/l 2,4-dichlorophenoxyacetic acid [224] and 50 mg/l kanamycin. Suspension cells were prepared in about 50-μm-thick, gas-permeable micro-chambers lined on one side with BioFoil (Vivascience, Hanover, Germany) and on the other side with a 24 x 24 mm coverslip [225]. The micro-chamber contained about 20 μl of cell suspensions. *Tradescantia virginiana* plants were grown in a growth chamber with a 16-hrs photoperiod at $25°$C and 8-hrs dark period at $18°$C and 75-80% relative humidity. Stamen hairs with dividing cells in the apical region were dissected from immature flower buds with a length of approximately 5 mm.

Cell treatment with BDM

Tobacco BY-2 suspension cells expressing cytoplasmic GFP were treated with 50 mM BDM from a freshly made stock of 0.5 M in demi water. The control cells were treated with demi water in appropriate amount used for drug treatment. After treatment cells were transferred into micro-chambers and within 30 min. were used for FRAP experiments.

FRAP

FRAP experiments were preformed on a confocal laser scanning microscope (CLSM) Zeiss LSM 510 Meta coupled to Zeiss Axiovert 200M inverted microscope, equipped with 63 × 1.4 NA oil immersion objective. Prebleach and postbleach images were acquired using low levels (2-4%) of excitation at 488 nm. Photobleaching was performed using 10 scans with the 488 nm laser line at 100% transmission in a square region of $2.2\ \mu\mathrm{m} \times 2.2\ \mu\mathrm{m}$ of cytoplasmic strands. The bleached region was always perpendicular to the long axis of the cytoplasmic strands and covered the entire width of the strand. Fluorescence intensity values of the bleached region in the cytoplasmic strand were measured every 0.0491 or 0.0983 s. and followed for 5 or 10 s. Fluorescence intensity values were normalised to compare the experiments of different treatments. The average time for 50 % recovery (half time of recovery, $\mathrm{t}_{1/2}$) was determined from fitting recovery curves.

Microinjection

For microinjection experiments we immobilised *T. virginiana* stamen hairs in a thin layer of 1% low temperature gelling agarose (BDH Laboratory Supplies, Poole, UK) in culture medium (5 mM HEPES, 1 mM $\mathrm{MgCl_2}$, and 0.1 mM $\mathrm{CaCl_2}$, pH 7.0) and 0.025% Triton X-100 (BDH Laboratory Supplies, UK), following the procedure described by *Vos et al, 1998* [226] Synthetic lipid (DOPG) vesicles were made of 98% of the anionic non-fluorescent phospholipid 1,2-Dioleoyl-sn-Glycero-3-[Phospho-rac-(1-glycerol)] (DOPG, Avanti Polar Lipids) and for 2% of the fluorescent phosphocholine Bodipy FC12-HPC (Molecular Probes, excitation maximum at 503 nm, emission maximum at 512 nm). Phospholipids were mixed together and dried onto a glass surface under a stream of nitrogen, followed by at least 2 hours under vacuum to remove the last traces of solvent. The dried lipid mixture was hydrated with microinjection buffer (5 mM HEPES, 0.1 mM KCl, pH 7.0) to a concentration of 0.5 mg/ml. The lipids were freeze-thawed with liquid nitrogen for five cycles to disperse them and pushed through an extruder with a polycarbonate filter with a 60 nm pore size to yield vesicles with a diameter of approximately 80 nm. The vesicle diameter was determined using dynamic light scattering. Stealth vesicles were made in a similar way, only with addition of 2, 5, 10, 20 and 30% of PEG phospholipids (1,2-Distearoyl-sn-Glycero-3-Phosphoethanolamine-N-[Methoxy(Polyethylene glycol)-5000] (Ammonium Salt) (Avanti Polar Lipids)). The microinjection experiments were conducted according to *Vos et al, 1998* [226]. In short, borosilicate needles with filament were back-filled with vesicle solution and mounted onto a micro-needle holder and attached into a screw type syringe (Gilmont Instruments, Barrington, Illinois) via water-filled fine polyethylene tubing. The needle holder was placed into a micro-manipulator (model N0-303, Narashige Scientific Instruments, Tokyo, Japan) mounted on an Eclipse TE-2000-S inverted microscope (Nikon, Tokyo, Japan). Images were collected with a 63x, 1.4 NA DIC lens with a Cell Map IC (BioRad, Hemel Hampstead, UK) confocal laser-scanning microscope.

Appendix D

The Duty Ratio

The Molecular motors that are studied in this thesis are processive motors i.e. a single motor can walk along a filamentous tracks without dissociating from it. A simple theoretical model called the *duty ratio* (originally called the duty cycle [75]) was developed to determine if a motor is processive [3, 76]. The duty ratio, r, (eq.D.1) is the fraction of time, τ_{on}, a single head of a molecular motor spends bound to the cytoskeleton during the hydrolysis of a single ATP. The velocity, V, of a motor head equals the working stroke, δ, divided by the time it spends bound to the cytoskeleton τ_{on}. Moreover, as the stepping cycle is related to the ATPase rate, ATPase, the total cycle time is expected to be $\tau_{\mathrm{tot}}{=}1/\mathrm{ATPase}$. Finally, it is possible to couple the duty ratio to the number of motor heads, N_{min}, needed for continuous movement. Combining the above leads to the following expressions for the duty ratio [3, 76]:

$$r = \frac{\tau_{\mathrm{on}}}{\tau_{\mathrm{on}} + \tau_{\mathrm{off}}} = \frac{\tau_{\mathrm{on}}}{\tau_{\mathrm{tot}}} = \frac{\delta \mathrm{ATPase}}{V} \cong \frac{1}{N_{\mathrm{min}}}. \tag{D.1}$$

Assuming that both heads spend an equal amount of time in bound state, the duty ratio has to be at least 0.5 for processive motors. At lower values there will always be moments at which none of the heads will be attached, and therefore more than two heads or even an array of motors would be required. Additionally, it is known that when a single processive head moves its path distance to the next available binding site, for kinesin this can be 8 nm (Inchworm) or 16 nm (Hand-over-hand), the centre of mass of the molecule only moves the distance of a single binding site. The duty ratio is constrained by the size of the conformational changes the motor makes as well as by the cytoskeletal path. A typical value for a processive kinesin-I motor is $r{=}0.5$ whereas a muscle myosin motor has a duty ratio of only $r{=}0.01$, suggesting that a single motor head only covers a small fraction of the distance between two binding sites [76]. This means that skeletal muscle myosin is not a processive motor and thus an array of motors is needed to work in concert to generate motion.

Bibliography

[1] Yuh-Ru Julie Lee and Bo. Liu. Cytoskeletal motors in arabidopsis. sixty-one kinesins and seventeen myosins. *Plant Physiol.*, 136:3877–3883, 2004.

[2] B. Alberts, A. Johnson, J. Lewis, M. Raff, K. Roberts, and P. Walter. *Molecular Biology of the Cell, 4th edition*. Garland Science, New York, 2002.

[3] Jonathon Howard. *Mechanics of Motor Proteins and the Cytoskeleton*. Sinauer Associates, February 2001.

[4] Lewis G. Tilney and Mary S. Tilney. The wily ways of a parasite: induction of actin assembly by listeria. *Trends in Microbiology*, 1(1):25 – 31, 1993.

[5] Teruo Shimmen and Etsuo Yokota. Cytoplasmic streaming in plants. *Current Opinion in Cell Biology*, 16(1):68 – 72, 2004.

[6] Teruo Shimmen. The sliding theory of cytoplasmic streaming: fiftyyears of progress. *Journal of Plant Research*, 120:31–43, 2007. 10.1007/s10265-006-0061-0.

[7] T. G. Huang and D. D. Hackney. Drosophila kinesin minimal motor domain expressed in escherichia coli. purification and kinetic characterization. *Journal of Biological Chemistry*, 269(23):16493–16501, 1994.

[8] Bert Nitzsche, Volker Bormuth, Corina Bräuer, Jonathon Howard, Leonid Ionov, Jacob Kerssemakers, Till Korten, Cecile Leduc, Felix Ruhnow, and Stefan Diez. Studying kinesin motors by optical 3d-nanometry in gliding motility assays. In Leslie Wilson and John J. Correia, editors, *Microtubules, in vitro*, volume 95 of *Methods in Cell Biology*, pages 247 – 271. Academic Press, 2010.

[9] Claudia Veigel and Christoph F. Schmidt. Moving into the cell: single-molecule studies of molecular motors in complex environments. *Nat Rev Mol Cell Biol*, 12(3):163–176, March 2011.

[10] Karel Svoboda, Christoph F. Schmidt, Bruce J. Schnapp, and Steven M. Block. Direct observation of kinesin stepping by optical trapping interferometry. *Nature*, 365(6448):721–727, October 1993.

[11] N. J. Carter and R. A. Cross. Mechanics of the kinesin step. *Nature*, 435(7040):308–312, May 2005.

[12] Yuichi Taniguchi, Masayoshi Nishiyama, Yoshiharu Ishii, and Toshio Yanagida. Entropy rectifies the brownian steps of kinesin. *Nat Chem Biol*, 1(6):342–347, November 2005.

[13] Charles L. Asbury, Adrian N. Fehr, and Steven M. Block. Kinesin moves by an asymmetric hand-over-hand mechanism. *Science*, 302(5653):2130–2134, 2003.

[14] J. Howard, A. J. Hudspeth, and R. D. Vale. Movement of microtubules by single kinesin molecules. *Nature*, 342(6246):154–158, November 1989.

[15] E. Meyhöfer and J. Howard. The force generated by a single kinesin molecule against an elastic load. *Proc. Nat. Acad. Sci.*, 92:574–578, 1995.

[16] Ronald D. Vale, Takashi Funatsu, Daniel W. Pierce, Laura Romberg, Yoshie Harada, and Toshio Yanagida. Direct observation of single kinesin molecules moving along microtubules. *Nature*, 380(6573):451–453, April 1996.

[17] Koen Visscher, Mark J. Schnitzer, and Steven M. Block. Single kinesin molecules studied with a molecular force clamp. *Nature*, 400(6740):184–189, July 1999.

[18] Eric Bednarski, Charles E. Ribak, and Gary Lynch. Suppression of cathepsins b and l causes a proliferation of lysosomes and the formation of meganeurites in hippocampus. *The Journal of Neuroscience*, 17(11):4006–4021, 1997.

[19] Sandra Moreno, Roberta Nardacci, and Maria Paola Cerù. Regional and ultrastructural immunolocalization of copper-zinc superoxide dismutase in rat central nervous system. *Journal of Histochemistry & Cytochemistry*, 45(12):1611–1622, 1997.

[20] Eileen J. Martin, Manho Kim, James Velier, Ellen Sapp, Hyun-Sook Lee, Genevieve Laforet, Lisa Won, Kathy Chase, Pradeep G. Bhide, Alfred Heller, Neil Aronin, and Marian Difiglia. Analysis of huntingtin-associated protein 1 in mouse brain and immortalized striatal neurons. *The Journal of Comparative Neurology*, 403(4):421–430, 1999.

[21] Soichiro Yamada, Denis Wirtz, and Scot C. Kuo. Mechanics of living cells measured by laser tracking microrheology. *Biophys J*, 78(4):1736–1747, April 2000.

[22] Hans Friberg, Michel Ferrand-Drake, Finn Bengtsson, Andrew P. Halestrap, and Tadeusz Wieloch. Cyclosporin a, but not fk 506, protects mitochondria and neurons against hypoglycemic damage and implicates the mitochondrial permeability transition in cell death. *The Journal of Neuroscience*, 18(14):5151–5159, 1998.

[23] D. B. Hill, M. J. Plaza, K. Bonin, and G. Holzwarth. Fast vesicle transport in pc12 neurites: velocities and forces. *European Biophysics Journal*, 33:623–632, 2004. 10.1007/s00249-004-0403-6.

[24] Sebastien Courty, Camilla Luccardini, Yohanns Bellaiche, Giovanni Cappello, and Maxime Dahan. Tracking individual kinesin motors in living cells using single quantum-dot imaging. *Nano Letters*, 6(7):1491–1495, 2006.

[25] Yuri Shtridelman, Thomas Cahyuti, Brigitte Townsend, David DeWitt, and Jed Macosko. Force-velocity curves of motor proteins cooperating in-vivo. *Cell Biochemistry and Biophysics*, 52:19–29, 2008. 10.1007/s12013-008-9021-8.

[26] Paolo Pierobon, Sarra Achouri, Sébastien Courty, Alexander R. Dunn, James A. Spudich, Maxime Dahan, and Giovanni Cappello. Velocity, processivity, and individual steps of single myosin v molecules in live cells. *Biophys J*, 96(10):4268–4275, May 2009.

[27] Rebecca Skloot. *The Immortal Life of Henrietta Lacks*. New York: Crown/Random House, 2010.

[28] A. Ashkin, Karin Schutze, J. M. Dziedzic, Ursula Euteneuer, and Manfred Schliwa. Force generation of organelle transport measured in vivo by an infrared laser trap. *Nature*, 348(6299):346–348, November 1990.

[29] Nobutaka Hirokawa. Kinesin and dynein superfamily proteins and the mechanism of organelle transport. *Science*, 279(5350):519–526, 1998.

[30] Motoki Tominaga, Hiroaki Kojima, Etsuo Yokota, Hidefumi Orii, Rinna Nakamori, Eisaku Katayama, Michael Anson, Teruo Shimmen, and Kazuhiro Oiwa. Higher plant myosin xi moves processively on actin with 35 nm steps at high velocity. *EMBO J*, 22(6):1263–1272, March 2003.

[31] Valeria Levi, Anna S. Serpinskaya, Enrico Gratton, and Vladimir Gelfand. Organelle transport along microtubules in xenopus melanophores: Evidence for cooperation between multiple motors. *Biophys J*, 90(1):318–327, January 2006.

[32] H. Kojima, E. Muto, H. Higuchi, and T. Yanagida. Mechanics of single kinesin molecules measured by optical trapping nanometry. *Biophys J*, 73(4):2012–2022, October 1997.

[33] A.J. Hunt, F. Gittes, and J. Howard. The force exerted by a single kinesin molecule against a viscous load. *Biophys J*, 67(2):766–781, August 1994.

[34] Frank Gibbons, Jean-François Chauwin, Marcelo Despósito, and Jorge V. José. A dynamical model of kinesin-microtubule motility assays. *Biophys J*, 80(6):2515–2526, June 2001.

[35] D.B. Hill. *Changes in the Number of Molecular Motors Driving Vesicle Transport in PC12.* PhD thesis, Wake Forest University, 2003.

[36] Kenji Kawaguchi and Shinichi Ishiwata. Temperature dependence of force, velocity, and processivity of single kinesin molecules. *Biochemical and Biophysical Research Communications*, 272(3):895 – 899, 2000.

[37] R.D. Allen, J. Metuzals, I. Tasaki, S.T. Brady, and S.P. Gilbert. Fast axonal transport in squid giant axon. *Science*, 218(4577):1127–1129, 1982.

[38] S.T. Brady, R.J. Lasek, and R.D. Allen. Fast axonal transport in extruded axoplasm from squid giant axon. *Science*, 218(4577):1129–1131, 1982.

[39] Jerome J. Freed and Marcia M. Lebowitz. The association of a class of saltatory movements with microtubules in cultured cells. *The Journal of Cell Biology*, 45(2):334–354, 1970.

[40] L. Rebuhn. *Saltatory particle movements and their relation to the mitotic apparatus (in "The cell in mitosis").* Academic Press, New York, 1967.

[41] Comert Kural, Hwajin Kim, Sheyum Syed, Gohta Goshima, Vladimir I. Gelfand, and Paul R. Selvin. Kinesin and dynein move a peroxisome in vivo: A tug-of-war or coordinated movement? *Science*, 308(5727):1469–1472, 2005.

[42] Jed C. Macosko, Jason M. Newbern, Jean Rockford, Ernest N. Chisena, Charlotte M. Brown, George M. Holzwarth, and Carol E. Milligan. Fewer active motors per vesicle may explain slowed vesicle transport in chick motoneurons after three days in vitro. *Brain Research*, 1211:6 – 12, 2008.

[43] Dawen Cai, Kristen J. Verhey, and Edgar Meyhöfer. Tracking single kinesin molecules in the cytoplasm of mammalian cells. *Biophys J*, 92(12):4137–4144, June 2007.

[44] Yakov Gluzman. Sv40-transformed simian cells support the replication of early sv40 mutants. *Cell*, 23(1):175 – 182, 1981.

[45] Jason Gagliano, Matthew Walb, Brian Blaker, Jed Macosko, and George Holzwarth. Kinesin velocity increases with the number of motors pulling against viscoelastic drag. *European Biophysics Journal*, 39:801–813, 2010. 10.1007/s00249-009-0560-8.

[46] B. Corti. *Osservazioni microscopiche sulla Tremella e sulla circolazione del fluido in una pianta acquajuola*. Apresso Guiseppe Rocchi, Lucca, Italia, 1774.

[47] N. Kamiya and K. Kuroda. Velocity distribution of the protoplasmic streaming in nitella cells. *Bot Mag Tokyo*, 69:544–554, 1956.

[48] T. Kohno and T. Shimmen. Accelerated sliding of pollen tube organelles along characeae actin bundles regulated by ca2+. *The Journal of Cell Biology*, 106(5):1539–1543, 1988.

[49] Silvia Romagnoli, Giampiero Cai, and Mauro Cresti. In vitro assays demonstrate that pollen tube organelles use kinesin-related motor proteins to move along microtubules. *The Plant Cell Online*, 15(1):251–269, 2003.

[50] Jonathan S. Berg, Bradford C. Powell, and Richard E. Cheney. A millennial myosin census. *Mol. Biol. Cell*, 12(4):780–794, 2001.

[51] James A. Spudich and Sivaraj Sivaramakrishnan. Myosin vi: an innovative motor that challenged the swinging lever arm hypothesis. *Nat Rev Mol Cell Biol*, 11(2):128–137, February 2010.

[52] H. Lee Sweeney and Anne Houdusse. Myosin vi rewrites the rules for myosin motors. *Cell*, 141(4):573–582, May 2010.

[53] Kohji Ito, Mitsuo Ikebe, Taku Kashiyama, Toshifumi Mogami, Takahide Kon, and Keiichi Yamamoto. Kinetic mechanism of the fastest motor protein, chara myosin. *Journal of Biological Chemistry*, 282(27):19534–19545, 2007.

[54] Jeanmarie Verchot-Lubicz and Raymond Goldstein. Cytoplasmic streaming enables the distribution of molecules and vesicles in large plant cells. *Protoplasma*, 240:99–107, 2010. 10.1007/s00709-009-0088-x.

[55] Claudia Veigel, Stephan Schmitz, Fei Wang, and James R. Sellers. Load-dependent kinetics of myosin-v can explain its high processivity. *Nat Cell Biol*, 7(9):861–869, September 2005.

[56] Yuri Shtridelman, George Holzwarth, Clayton Bauer, Natalie Gassman, David DeWitt, and Jed Macosko. Multimotor force-velocity curves by tracking and sizing sub-diffraction limited vesicles. *Cellular and Molecular Bioengineering*, 2:190–199, 2009. 10.1007/s12195-009-0064-8.

[57] R. Byron Bird, Warren E. Stewart, and Edwin N. Lightfoot. *Transport Phenomena*. John Wiley & Sons, Inc., 2nd edition edition, 2006.

[58] J.M.J. den Toonder. Low reynolds number flows. `http://www.hitech-projects.com/euprojects/artic/index/Low%20Reynolds%20number%20flows.pdf`. [Online; accessed 23-February-2013].

[59] Brian J. Kirby. *Micro- and Nanoscale Fluid Mechanics - Transport in Microfluidic Devices*. Cambridge University Press, 1th edition, 2010. ISBN: 9780521119030.

[60] J. Happel and H. Brenner. *Low Reynolds Number Hydrodynamics*. Mechanics of fluid and transport processes. Martinus Nijhoff Publishers, Dordrecht, second edition, fourth printing edition, 1986.

[61] Savitha Sharma, Sushama Wagh, and Raman Govindarajan. Melanosomal proteins - role in melanin polymerization. *Pigment Cell Research*, 15(2):127–133, 2002.

[62] David L. Coy, Michael Wagenbach, and Jonathon Howard. Kinesin takes one 8-nm step for each atp that it hydrolyzes. *Journal of Biological Chemistry*, 274(6):3667–3671, 1999.

[63] M. Doi. *Introduction to Polymer Physics*. Oxford University Press, 1996.

[64] E. M. Purcell. Life at low reynolds number. *American Journal of Physics*, 45(1):3–11, January 1977.

[65] Steven Vogel. *Life in Moving Fluids: The Physical Biology of Flow*. Princeton University Press, second edition, 1996.

[66] J. K. G. Dhont. *An Introduction to Dynamics of Colloids*. Elsevier science B.V., Amsterdam, 1996.

[67] M. Doi and S.F. Edwards. *The Theory Of Polymer Dynamics*. Oxford University Press, 1986.

[68] W. Hess and R. Klein. Generalized hydrodynamics of systems of brownian particles. *Advances in Physics*, 32(2):173–283, 1983.

[69] M. P. Allen and D. J. Tildesley. *Computer Simulation Of Liquids*. Oxford Science Publications, 1987.

[70] B. Goddard, G. Pavliotis, and S. Kalliadasis. The overdamped limit of dynamic density functional theory: Rigorous results. *Multiscale Model. Simul.*, 10(2):633–663, January 2012.

[71] José A. Fornés. Hydrodynamic interactions induce movement against an external load in a ratchet dimer brownian motor. *Journal of Colloid and Interface Science*, 341(2):376 – 379, 2010.

[72] Donald L. Ermak and J. A. McCammon. Brownian dynamics with hydrodynamic interactions. *The Journal of Chemical Physics*, 69(4):1352–1360, 1978.

[73] Ronald D. Vale and Ronald A. Milligan. The way things move: Looking under the hood of molecular motor proteins. *Science*, 288(5463):88–95, 2000.

[74] Anatoly B. Kolomeisky and Michael E. Fisher. Molecular motors: A theorist's perspective. *Annual Review of Physical Chemistry*, 58(1):675–695, 2007.

[75] P.F. Dillon and R.A. Murphy. High force development and crossbridge attachment in smooth muscle from swine carotid arteries. *Circ Res*, 50(6):799–804, 1982.

[76] Joe Howard. Molecular motors: structural adaptations to cellular functions. *Nature*, 389(6651):561–567, October 1997.

[77] Wei Hua, Johnson Chung, and Jeff Gelles. Distinguishing inchworm and hand-over-hand processive kinesin movement by neck rotation measurements. *Science*, 295(5556):844–848, 2002.

[78] Ahmet Yildiz, Joseph N. Forkey, Sean A. McKinney, Taekjip Ha, Yale E. Goldman, and Paul R. Selvin. Myosin v walks hand-over-hand: Single fluorophore imaging with 1.5-nm localization. *Science*, 300(5628):2061–2065, 2003.

[79] Ahmet Yildiz, Michio Tomishige, Ronald D. Vale, and Paul R. Selvin. Kinesin walks hand-over-hand. *Science*, 303(5658):676–678, 2004.

[80] So Nishikawa, Ikuo Arimoto, Keigo Ikezaki, Mitsuhiro Sugawa, Hiroshi Ueno, Tomotaka Komori, Atsuko H. Iwane, and Toshio Yanagida. Switch between large hand-over-hand and small inchworm-like steps in myosin vi. *Cell*, 142(6):879–888, September 2010.

[81] Steven M. Block. Fifty ways to love your lever: Myosin motors. *Cell*, 87(2):151 – 157, 1996.

[82] Alexander R. Dunn and James A. Spudich. Dynamics of the unbound head during myosin v processive translocation. *Nat Struct Mol Biol*, 14(3):246–248, March 2007.

[83] Katsuyuki Shiroguchi and Kazuhiko Kinosita. Myosin v walks by lever action and brownian motion. *Science*, 316(5828):1208–1212, 2007.

[84] Mitsuhiro Iwaki, Atsuko H Iwane, Tetsuya Shimokawa, Roger Cooke, and Toshio Yanagida. Brownian search-and-catch mechanism for myosin-vi steps. *Nat Chem Biol*, 5(6):403–405, June 2009.

[85] M. von Smoluchowski. Experimentell nachweisbare, der üblichen thermodynamik widersprechende molekularphänomener. *Phys. Zeitschr.*, 13:1069, 1912.

[86] Peter Reimann. Brownian motors: noisy transport far from equilibrium. *Physics Reports*, 361(2-4):57 – 265, 2002.

[87] R.P. Feynman, R.B. Leighton, and M. Sands. *The Feynman lectures on physics. Vol. 1, Mainly mechanics, radiation and heat*. Addison-Wesley, Reading, Massachusetts, 1964. Chapter 46.

[88] Zénó Farkas. *Transport by Ratchet Mechanism: Application to Granules and DNA*. PhD thesis, Eötvös University, Budapest, Hungary, 2001.

[89] Jonne Helenius, Gary Brouhard, Yannis Kalaidzidis, Stefan Diez, and Jonathon Howard. The depolymerizing kinesin mcak uses lattice diffusion to rapidly target microtubule ends. *Nature*, 441(7089):115–119, May 2006.

[90] Benjamin H. Kwok, Lukas C. Kapitein, Jeffrey H. Kim, Erwin J. G. Peterman, Christoph F. Schmidt, and Tarun M. Kapoor. Allosteric inhibition of kinesin-5 modulates its processive directional motility. *Nat Chem Biol*, 2(9):480–485, September 2006.

[91] Yasushi Okada and Nobutaka Hirokawa. Mechanism of the single-headed processivity: Diffusional anchoring between the k-loop of kinesin and the c terminus of tubulin. *Proceedings of the National Academy of Sciences*, 97(2):640–645, 2000.

[92] Frank Jülicher, Armand Ajdari, and Jacques Prost. Modeling molecular motors. *Rev. Mod. Phys.*, 69(4):1269–1282, 1997.

[93] P. Reimann and P. Hänggi. Introduction to the physics of brownian motors. *Applied Physics A: Materials Science & Processing*, 75:169–178, 2002. 10.1007/s003390201331.

[94] R. Dean Astumian. Thermodynamics and kinetics of a brownian motor. *Science*, 276(5314):917–922, 1997.

[95] Frank Jülicher. Force and motion generation of molecular motors: A generic description, 1999.

[96] Jennifer E. Curtis and David G. Grier. Structure of optical vortices. *Phys. Rev. Lett.*, 90(13):133901, Apr 2003.

[97] Michael Reichert and Holger Stark. Circling particles and drafting in optical vortices. *Journal of Physics: Condensed Matter*, 16(38):S4085, 2004.

[98] C. Lutz, M. Reichert, H. Stark, and C. Bechinger. Surmounting barriers: The benefit of hydrodynamic interactions. *EPL (Europhysics Letters)*, 74(4):719, 2006.

[99] James M. Polson, Brian Bylhouwer, Martin J. Zuckermann, Arthur J. Horton, and William M. Scott. Dynamics of a polymer in a brownian ratchet. *Phys. Rev. E*, 82(5):051931, Nov 2010.

[100] Andrej Grimm and Holger Stark. Hydrodynamic interactions enhance the performance of brownian ratchets. *Soft Matter*, 7(7):3219–3227, 2011.

[101] A. Parmeggiani, T. Franosch, and E. Frey. Phase coexistence in driven one-dimensional transport. *Phys. Rev. Lett.*, 90(8):086601, Feb 2003.

[102] A. Parmeggiani, T. Franosch, and E. Frey. Totally asymmetric simple exclusion process with langmuir kinetics. *Phys. Rev. E*, 70(4):046101, Oct 2004.

[103] Carolyn T. MacDonald, Julian H. Gibbs, and Allen C. Pipkin. Kinetics of biopolymerization on nucleic acid templates. *Biopolymers*, 6(1):1–25, 1968.

[104] Debashish Chowdhury. Traffic flow of interacting self-driven particles: Rails and trails, vehicles and vesicles. *Physica Scripta*, 2003(T106):13, 2003.

[105] Dirk Helbing. Traffic and related self-driven many-particle systems. *Rev. Mod. Phys.*, 73(4):1067–1141, Dec 2001.

[106] Irving Langmuir. The constitution and fundamental properties of solids and liquids. part i. solids. *Journal of the American Chemical Society*, 38(11):2221–2295, 1916.

[107] Roop Mallik, Brian C. Carter, Stephanie A. Lex, Stephen J. King, and Steven P. Gross. Cytoplasmic dynein functions as a gear in response to load. *Nature*, 427(6975):649–652, February 2004.

[108] Ambarish Kunwar, Andreas Schadschneider, and Debashish Chowdhury. From aggressive driving to molecular motor traffic. *Journal of Physics A: Mathematical and General*, 39(46):14263, 2006.

[109] Alexander Yu. Morozov, Ekaterina Pronina, Anatoly B. Kolomeisky, and Maxim N. Artyomov. Solutions of burnt-bridge models for molecular motor transport. *Phys. Rev. E*, 75(3):031910, Mar 2007.

[110] Max N. Artyomov, Alexander Yu. Morozov, and Anatoly B. Kolomeisky. Molecular motors interacting with their own tracks. *Phys. Rev. E*, 4(4):040901, Apr 2008.

[111] Johannes H.P. Schulz, Anatoly B. Kolomeisky, and Erwin Frey. Current reversal and exclusion processes with history-dependent random walks, April 2011.

[112] Stefan Klumpp and Reinhard Lipowsky. Asymmetric simple exclusion processes with diffusive bottlenecks. *Phys. Rev. E*, 70(6):066104, Dec 2004.

[113] Philip Greulich and Andreas Schadschneider. Disordered driven lattice gases with boundary reservoirs and langmuir kinetics. *Phys. Rev. E*, 79(3):031107–21, Mar 2009.

[114] Zhong-Pan Cai, Yao-Ming Yuan, Rui Jiang, Katsuhiro Nishinari, and Qing-Song Wu. The effect of attachment and detachment on totally asymmetric exclusion processes with junctions. *Journal of Statistical Mechanics: Theory and Experiment*, 2009(02):P02050, 2009.

[115] Xiao Song, Cai Jiu-Ju, Liu Fei, and Liu Ming-Zhe. Effect of unequal injection rates and different hopping rates on asymmetric exclusion processes with junction. *Chinese Physics B*, 19(9):090202, 2010.

[116] Yan Chai, Stefan Klumpp, Melanie J. I. Müller, and Reinhard Lipowsky. Traffic by multiple species of molecular motors. *Phys. Rev. E*, 80(4):041928, Oct 2009.

[117] S. Klumpp and R. Lipowsky. Phase transitions in systems with two species of molecular motors. *EPL (Europhysics Letters)*, 66(1):90, 2004.

[118] Sudipto Muhuri and Ignacio Pagonabarraga. Lattice-gas model for active vesicle transport by molecular motors with opposite polarities. *Phys. Rev. E*, 82(2):021925–39, Aug 2010.

[119] Alan Gabel, P. L. Krapivsky, and S. Redner. Facilitated asymmetric exclusion. *Phys. Rev. Lett.*, 105(21):210603, Nov 2010.

[120] Carla Goldman and Elisa T. Sena. The dynamics of cargo driven by molecular motors in the context of asymmetric simple exclusion processes. *Physica A: Statistical Mechanics and its Applications*, 388(17):3455–3464, September 2009.

[121] Carla Goldman. A hopping mechanism for cargo transport bymolecular motors on crowded microtubules. *Journal of Statistical Physics*, 140:1–15, 2010. 10.1007/s10955-010-0037-2.

[122] M. R. Evans, Y. Kafri, K. E. P. Sugden, and J. Tailleur. Phase diagram of two-lane driven diffusive systems, 2011.

[123] Maximilian Ebbinghaus and Ludger Santen. A model for bidirectional traffic of cytoskeletal motors. *Journal of Statistical Mechanics: Theory and Experiment*, 2009(03):P03030, 2009.

[124] M. Ebbinghaus, C. Appert-Rolland, and L. Santen. Particle interactions and lattice dynamics: Scenarios for efficient bidirectional stochastic transport?, 2011.

[125] Qi-Hong Shi, Rui Jiang, Mao-Bin Hu, and Qing-Song Wu. Strong asymmetric coupling of two parallel exclusion processes. *Journal of Statistical Physics*, 142(3):616–626, Feb 2011. 10.1007/s10955-011-0128-8.

[126] Anna Melbinger, Tobias Reichenbach, Thomas Franosch, and Erwin Frey. Driven transport on parallel lanes with particle exclusion and obstruction. *Phys. Rev. E*, 83(3):031923, Mar 2011.

[127] Vladislav Popkov and Ingo Peschel. Symmetry breaking and phase coexistence in a driven diffusive two-channel system. *Phys. Rev. E*, 64(2):026126, Jul 2001.

[128] Róbert Juhász. Dynamics at barriers in bidirectional two-lane exclusion processes. *Journal of Statistical Mechanics: Theory and Experiment*, 2010(03):P03010, Mar 2010.

[129] Reinhard Lipowsky, Stefan Klumpp, and Theo M. Nieuwenhuizen. Random walks of cytoskeletal motors in open and closed compartments. *Phys. Rev. Lett.*, 87(10):108101, Aug 2001.

[130] Stefan Klumpp and Reinhard Lipowsky. Traffic of molecular motors through tube-like compartments. *Journal of Statistical Physics*, 113:233–268, 2003. 10.1023/A:1025778922620.

[131] Theo M. Nieuwenhuizen, Stefan Klumpp, and Reinhard Lipowsky. Random walks of molecular motors arising from diffusional encounters with immobilized filaments. *Phys. Rev. E*, 69(6):061911, Jun 2004.

[132] Stefan Klumpp and Reinhard Lipowsky. Active diffusion of motor particles. *Phys. Rev. Lett.*, 95(26):268102, Dec 2005.

[133] Stefan Klumpp, Theo M. Nieuwenhuizen, and Reinhard Lipowsky. Self-organized density patterns of molecular motors in arrays of cytoskeletal filaments. *Biophys J*, 88(5):3118–3132, May 2005.

[134] Stefan Klumpp and Reinhard Lipowsky. Cooperative cargo transport by several molecular motors. *Proceedings of the National Academy of Sciences of the United States of America*, 102(48):17284–17289, 2005.

[135] Melanie J. I. Müller, Stefan Klumpp, and Reinhard Lipowsky. Tug-of-war as a cooperative mechanism for bidirectional cargo transport by molecular motors. *Proceedings of the National Academy of Sciences*, 105(12):4609–4614, 2008.

[136] Melanie J.I. Müller, Stefan Klumpp, and Reinhard Lipowsky. Bidirectional transport by molecular motors: Enhanced processivity and response to external forces. *Biophys J*, 98(11):2610–2618, June 2010.

[137] Stefan Klumpp, Yan Chai, and Reinhard Lipowsky. Effects of the chemomechanical stepping cycle on the traffic of molecular motors. *Phys. Rev. E*, 78(4):041909, Oct 2008.

[138] Yan Chai, Reinhard Lipowsky, and Stefan Klumpp. Transport by molecular motors in the presence of static defects. *Journal of Statistical Physics*, 135:241–260, 2009. 10.1007/s10955-009-9715-3.

[139] H. Grzeschik, R. J. Harris, and L. Santen. Traffic of cytoskeletal motors with disordered attachment rates. *Phys. Rev. E*, 81(3):031929, Mar 2010.

[140] Arne Seitz, Hiroaki Kojima, Kazuhiro Oiwa, Eva-Maria Mandelkow, Young-Hwa Song, and Eckhard Mandelkow. Single-molecule investigation of the interference between kinesin, tau and map2c. *EMBO J*, 21(18):4896–4905, September 2002.

[141] B. Trinczek, A. Ebneth, E.M. Mandelkow, and E. Mandelkow. Tau regulates the attachment/detachment but not the speed of motors in microtubule-dependent transport of single vesicles and organelles. *Journal of Cell Science*, 112(14):2355–2367, 1999.

[142] F. Hernández and J. Avila. Tauopathies. *Cellular and Molecular Life Sciences*, 64:2219–2233, 2007. 10.1007/s00018-007-7220-x.

[143] Thomas Surrey, François Nédélec, Stanislas Leibler, and Eric Karsenti. Physical properties determining self-organization of motors and microtubules. *Science*, 292(5519):1167–1171, 2001.

[144] François Nédélec, Thomas Surrey, and A. C. Maggs. Dynamic concentration of motors in microtubule arrays. *Phys. Rev. Lett.*, 86(14):3192–3195, Apr 2001.

[145] Christian Korn. *Stochastic dynamics of cell adhesion in hydrodynamic flow*. PhD thesis, University of Potsdam, 2007.

[146] Christian B. Korn, Stefan Klumpp, Reinhard Lipowsky, and Ulrich S. Schwarz. Stochastic simulations of cargo transport by processive molecular motors. *The Journal of Chemical Physics*, 131(24):245107, 2009.

[147] Janina Beeg, Stefan Klumpp, Rumiana Dimova, Rubèn Serral Gracià, Eberhard Unger, and Reinhard Lipowsky. Transport of beads by several kinesin motors. *Biophysical Journal*, 94(2):532 – 541, 2008.

[148] Arthur R. Rogers, Jonathan W. Driver, Pamela E. Constantinou, D. Kenneth Jamison, and Michael R. Diehl. Negative interference dominates collective transport of kinesin motors in the absence of load. *Phys. Chem. Chem. Phys.*, 11(24):4882–4889, 2009.

[149] D. Houtman, I. Pagonabarraga, C. P. Lowe, A. Esseling-Ozdoba, A. M. C. Emons, and E. Eiser. Hydrodynamic flow caused by active transport along cytoskeletal elements. *EPL (Europhysics Letters)*, 78(1):18001, 2007.

[150] A. Esseling-Ozdoba, D. Houtman, A.A.M. van Lammeren, E. Eiser, and A.M.C. Emons. Hydrodynamic flow in the cytoplasm of plant cells. *Journal of Microscopy*, 231(2):274–283, 2008.

[151] K. Luby-Phelps. Cytoarchitecture and physical properties of cytoplasm: volume, viscosity, diffusion, intracellular surface area. *International review of Cytology*, 192(0074-7696 (Linking)):189–221, 2000.

[152] L. Lubińska. *Axoplasmic Streaming in Regeneration and in normal nerve fibres*, volume 13 of *Progress in brain research*. Elsevier, 1964.

[153] Mathew J. Wedel. A monument of inefficiency: the presumed course of the recurrent laryngeal nerve in sauropod dinosaurs. *Acta Palaeontologica Polonica*, 57(2):251–256, 2012.

[154] H. Brenner. Coupling between the translational and rotational brownian motions of rigid particles of arbitrary shape i. helicoidally isotropic particles. *Journal of Colloid Science*, 20(2):104–122, February 1965.

[155] Michael Reichert. *Hydrodynamic Interactions in Colloidal and Biological Systems*. PhD thesis, Universität Konstanz, 2006.

[156] Daan Frenkel and Berend Smit. *Understanding molecular simulation: from algorithms to applications*, volume Computational Science Series Volume 1. Academic Press (Elsevier), second edition edition, 2002.

[157] Michael P. Brenner. Screening mechanisms in sedimentation. *Physics of Fluids*, 11(4):754–772, 1999.

[158] Jens Rotne and Stephen Prager. Variational treatment of hydrodynamic interaction in polymers. *Journal of Chemical Physics*, 50(11):4831, 1969.

[159] Hiromi Yamakawa. Transport properties of polymer chains in dilute solution: Hydrodynamic interaction. *Journal of Chemical Physics*, 53(1):436, 1970.

[160] Holler J. Crouch S. Skoog, D. *Principles of Instrumental Analysis.* Thomson Brooks/Cole: Belmont, 6th edition, 2007.

[161] Noburô Kamiya. Cytoplasmic streaming in giant algal cells: A historical survey of experimental approaches. *Journal of Plant Research*, 99:441–467, 1986. 10.1007/BF02488723.

[162] Agnieszka Esseling-Ozdoba. *Getting there: Vesicles en route for plant cytokinesis.* PhD thesis, Wageningen Universiteit, 2007.

[163] Natsumaro Kutsuna and Seiichiro. Hasezawa. Dynamic organization of vacuolar and microtubule structures during cell cycle progression in synchronized tobacco by-2 cells. *Plant Cell Physiol.*, 43:965–973, 2002.

[164] N. Ruthardt, N. Gulde, H. Spiegel, R. Fischer, and N. Emans. Four-dimensional imaging of transvacuolar strand dynamics in tobacco by-2 cells. *Protoplasma*, 225:205–215, 2005. 10.1007/s00709-005-0093-7.

[165] Takumi Higaki, Natsumaro Kutsuna, Emiko Okubo, Toshio Sano, and Seiichiro. Hasezawa. Actin microfilaments regulate vacuolar structures and dynamics: dual observation of actin microfilaments and vacuolar membrane in living tobacco by-2 cells. *Plant Cell Physiol.*, 47:839–852, 2006.

[166] Anja Hoffmann and Andreas Nebenführ. Dynamic rearrangements of transvacuolar strands in by-2 cells imply a role of myosin in remodeling the plant actin cytoskeleton. *Protoplasma*, 224:201–210, 2004. 10.1007/s00709-004-0068-0.

[167] Y. Iwanami. Protoplasmic movement in pollen grains and tubes. *Phytomorphology*, 6:288–295, 1956.

[168] Bjorn Sieberer and Anne Emons. Cytoarchitecture and pattern of cytoplasmic streaming in root hairs of medicago truncatula during development and deformation by nodulation factors. *Protoplasma*, 214:118–127, 2000. 10.1007/BF02524268.

[169] F. Grolig and E. S. Pierson. Cytoplasmic streaming: from flow to track. *Developments in plant and soil sciences*, 89:165–190, 2000.

[170] Deborah D. Miller, Stylianos Scordilis, and Peter K. Hepler. Identification and localization of three classes of myosins in pollen tubes of lilium longiflorum and nicotiana alata. *J. Cell Sci.*, 108:2549–63, 1995.

[171] E. Yokota, A. R. McDonald, B. Liu, T. Shimmen, and B. A. Palevitz. Localization of a 170 kda myosin heavy chain in plant cells. *Protoplasma*, 185:178–87, 1995.

[172] Andreas Nebenführ, Larry A. Gallagher, Terri G. Dunahay, Jennifer A. Frohlick, Anna M. Mazurkiewicz, Janet B. Meehl, and L. Andrew. Staehelin. Stop-and-go movements of plant golgi stacks are mediated by the actomyosin system. *Plant Physiol.*, 121:1127–1141, 1999.

[173] Chris J. Staiger. Signaling to the actin cytoskeleton in plants. *Annu. Rev. Plant Physiol. Plant Mol. Biol.*, 51:257–288, 2000.

[174] R. Bakhuizen, P. C. van Spronsen, F. A. J. Sluiman-den Hertog, C. J. Venverloo, and L. Goosen-de Roo. Nuclear envelope radiating microtubules in plant cells during interphase mitosis transition. *Protoplasma*, 128:43–51, 1985. 10.1007/BF01273234.

[175] Pankaj Dhonukshe, Jaideep Mathur, Martin Hulskamp, and Theodorus Gadella. Microtubule plus-ends reveal essential links between intracellular polarization and localized modulation of endocytosis during division-plane establishment in plant cells. *BMC Biology*, 3(1):11, 2005.

[176] D.J. Flanders, D.J. Rawlins, P.J. Shaw, and C.W. Lloyd. Re-establishment of the interphase microtubule array in vacuolated plant cells, studied by confocal microscopy and 3-d imaging. *Development*, 110(3):897–904, 1990.

[177] Anne Mie C. Emons. The cytoskeleton and secretory vesicles in root hairs of equisetum and limnobium and cytoplasmic streaming in root hairs of equisetum. *Annals of Botany*, 60(6):625–632, 1987.

[178] Deborah D. Miller, Norbert C. A. De Ruijter, Ton Bisseling, and Anne Mie C. Emons. The role of actin in root hair morphogenesis: studies with lipochito-oligosaccharide as a growth stimulator and cytochalasin as an actin perturbing drug. *Plant J.*, 17:141–154, 1999.

[179] Etsuo Yokota, Luis Vidali, Motoki Tominaga, Hiroshi Tahara, Hidefumi Orii, Yosuke Morizane, Peter K. Hepler, and Teruo Shimmen. Plant 115-kda actin-filament bundling protein, p-115-abp, is a homologue of plant villin and is widely distributed in cells. *Plant and Cell Physiology*, 44(10):1088–1099, 2003.

[180] Silvia Romagnoli, Giampiero Cai, Claudia Faleri, Etsuo Yokota, Teruo Shimmen, and Mauro. Cresti. Microtubule- and actin filament-dependent motors are distributed on pollen tube mitochondria and contribute differently to their movement. *Plant Cell Physiol.*, 48:345–361, 2007.

[181] Anna H. N. de Win, Marcel Worring, Jan Derksen, and Elisabeth S. Pierson. Classification of organelle trajectories using region-based curve analysis. *Cytometry*, 29(2):136–146, 1997.

[182] Jan Derksen, Bart Knuiman, Karin Hoedemaekers, Anouchka Guyon, Sandrine Bonhomme, and Elisabeth S. Pierson. Growth and cellular organization of arabidopsis pollen tubes in vitro. *Sexual Plant Reproduction*, 15(3):133–139, 2002. 10.1007/s00497-002-0149-1.

[183] Carola L. Holweg. Living markers for actin block myosin-dependent motility of plant organelles and auxin. *Cell Motility and the Cytoskeleton*, 64(2):69–81, 2007.

[184] Encyclopedia Britannica. Fluid mechanics. `http://www.britannica.com/EBchecked/topic/211272/fluid-mechanics`.

[185] C. Herrmann, J. Wray, F. Travers, and T. Barman. Effect of 2,3-butanedione monoxime on myosin and myofibrillar atpases. an example of an uncompetitive inhibitor. *Biochemistry*, 31:12227–32, 1992.

[186] Tasha M. Molchan, Aline H. Valster, and Peter K. Hepler. Actomyosin promotes cell plate alignment and late lateral expansion in tradescantia stamen hair cells. *Planta*, 214:683–693, 2002.

[187] M. Tominaga, E. Yokota, S. Sonobe, and T. Shimmen. Mechanism of inhibition of cytoplasmic streaming by a myosin inhibitor, 2,3-butanedione monoxime. *Protoplasma*, 213:46–54, 2000.

[188] Gregory Jedd and Nam-Hai. Chua. Visualization of peroxisomes in living plant cells reveals acto-myosin-dependent cytoplasmic streaming and peroxisome budding. *Plant Cell Physiol.*, 43:384–392, 2002.

[189] K. Van Gestel, R.H. Kohler, and J-P. Verbelen. Plant mitochondria move on f-actin, but their positioning in the cortical cytoplasm depends on both f-actin and microtubules. *Journal of Experimental Botany*, 53(369):659–667, 2002.

[190] Dennis E. Discher and Adi. Eisenberg. Materials science: Soft surfaces: Polymer vesicles. *Science (Washington, DC, U. S.)*, 297:967–973, 2002.

[191] C. J. Staiger and M. Schliwa. Actin localization and function in higher plants. *Protoplasma*, 141:1–12, 1987.

[192] Kohsuke Hashimoto, Hisako Igarashi, Shoji Mano, Mikio Nishimura, Teruo Shimmen, and Etsuo. Yokota. Peroxisomal localization of a myosin xi isoform in arabidopsis thaliana. *Plant Cell Physiol.*, 46:782–789, 2005.

[193] Daniel Reisen and Maureen Hanson. Association of six yfp-myosin xi-tail fusions with mobile plant cell organelles. *BMC Plant Biology*, 7(1):6, 2007.

[194] Lior Golomb, Mohamad Abu-Abied, Eduard Belausov, and Einat Sadot. Different subcellular localizations and functions of arabidopsis myosin viii. *BMC Plant Biology*, 8(1):3, 2008.

[195] Tijs Ketelaar, Norbert C. A. De Ruijter, and Anne Mie C. Emons. Unstable f-actin specifies the area and microtubule direction of cell expansion in arabidopsis root hairs. *Plant Cell*, 15:285–292, 2003.

[196] A. Dauphin, N. C. A. De Ruijter, A. M. C. Emons, and V. Legue. Actin organization during eucalyptus root hair development and its response to fungal hypaphorine. *Plant Biol. (Stuttgart, Ger.)*, 8:204–211, 2006.

[197] Roger R. Lew. Mass flow and pressure-driven hyphal extension in neurospora crassa. *Microbiology (Reading, U. K.)*, 151:2685–2692, 2005.

[198] Nira Pollock, Eugenio L. de Hostos, Christoph W. Turck, and Ronald D. Vale. Reconstitution of membrane transport powered by a novel dimeric kinesin motor of the unc104/kif1a family purified from dictyostelium. *The Journal of Cell Biology*, 147(3):493–506, 1999.

[199] A.D. Mehta, R.S. Rock, M. Rief, J.A. Spudich, M.S. Mooseker, and R.E. Cheney. Myosin-v is a processive actin-based motor. *Nature*, 400(6744):590–593, August 1999.

[200] Shane R. Nelson, M. Yusuf Ali, Kathleen M. Trybus, and David M. Warshaw. Random walk of processive, quantum dot-labeled myosin va molecules within the actin cortex of cos-7 cells. *Biophys J*, 97(2):509–518, July 2009.

[201] J. Inoue Chaen, S. and H. Sugi. The force-velocity relationship of the atp-dependent actin-myosin sliding causing cytoplasmic streaming in algal cells, studied using a centrifuge microscope. *The journal of Experimental Biology*, 198:1021–1027, 1995.

[202] K. Oiwa, S. Chaen, E. Kamitsubo, T. Shimmen, and H. Sugi. Steady-state force-velocity relation in the atp-dependent sliding movement of myosin-coated beads on actin cables in vitro studied with a centrifuge microscope. *Proceedings of the National Academy of Sciences*, 87(20):7893–7897, 1990.

[203] R. M. Spudich J. A. Finer, J. T. Simmons. Single myosin molecule mechanics: piconewton forces and nanometre steps. *Nature*, 6467:113, 1994.

[204] A. Ishijima, H. Kojima, H. Higuchi, Y. Harada, T. Funatsu, and T. Yanagida. Multiple- and single-molecule analysis of the actomyosin motor by nanometer-piconewton manipulation with a microneedle: unitary steps and forces. *Biophysical Journal*, 70(1):383 – 400, 1996.

[205] Haruo Sugi and Shigeru Chaen. Force-velocity relationships in actin-myosin interactions causing cytoplasmic streaming in algal cells. *The Journal of Experimental Biology*, 206:1971–1976, 2003.

[206] Tobias R. Zahn, Joseph K. Angleson, Margaret A. MacMorris, Erin Domke, John F. Hutton, Cindi Schwartz, and John C. Hutton. Dense core vesicle dynamics in caenorhabditis elegans neurons and the role of kinesin unc-104. *Traffic*, 5(7):544–559, 2004.

[207] Luciana Bruno, Maria Echarte, and Valeria Levi. Exchange of microtubule molecular motors during melanosome transport in xenopus laevis melanophores is triggered by collisions with intracellular obstacles. *Cell Biochemistry and Biophysics*, 52:191–201, 2008. 10.1007/s12013-008-9034-3.

[208] Steven P. Gross, Michael A. Welte, Steven M. Block, and Eric F. Wieschaus. Coordination of opposite-polarity microtubule motors. *The Journal of Cell Biology*, 156(4):715–724, 2002.

[209] Raymond E. Goldstein, Idan Tuval, and Jan-Willem van de Meent. Microfluidics of cytoplasmic streaming and its implications for intracellular transport. *Proceedings of the National Academy of Sciences*, 105(10):3663–3667, 2008.

[210] G.S. Perkins and R.B. Jones. Hydrodynamic interaction of a spherical particle with a planar boundary: Ii. hard wall. *Physica A: Statistical Mechanics and its Applications*, 189(3-4):447–477, November 1992.

[211] B. Cichocki and R.B. Jones. Image representation of a spherical particle near a hard wall. *Physica A: Statistical Mechanics and its Applications*, 258(3-4):273–302, September 1998.

[212] C. B. Korn and U. S. Schwarz. Mean first passage times for bond formation for a brownian particle in linear shear flow above a wall. *The Journal of Chemical Physics*, 126(9):095103, 2007.

[213] Ashutosh Agarwal and Henry Hess. Molecular motors as components of future medical devices and engineered materials. *J. Nanotechnol. Eng. Med.*, 1(1):011005–9, February 2010.

[214] D. J. G. Bakewell and D. V. Nicolau. Protein linear molecular motor-powered nanodevices. *Australian Journal of Chemistry*, 60(5):314–332, 2007.

[215] Henry Hess. Engineering applications of biomolecular motors. *Annu. Rev. Biomed. Eng.*, 13(1):429–450, July 2011.

[216] Martin G. L. van den Heuvel and Cees Dekker. Motor proteins at work for nanotechnology. *Science*, 317(5836):333–336, 2007.

[217] J.M.J. den Toonder and P.R. Onck. *Artificial Cilia*, chapter Introduction. RSC Nanoscience & Nanotechnology Series. RSC Publishing, ISBN 978-1-84973-597-1, In press, 2013.

[218] Daniel Riveline, A. Ott, Frank Julicher, Donald A. Winkelmann, Olivier Cardoso, Jean-Jacques Lacapère, Soffia Magnúsdóttir, J. L. Viovy, Laurence Gorre-Talini, and Jacques Prost. Acting on actin: the electric motility assay. *European Biophysics Journal*, 27(4):403–408, 1998.

[219] Benjamin M. Hutchins, Mark Platt, William O. Hancock, and Mary Elizabeth Williams. Directing transport of cofe2o4-functionalized microtubules with magnetic fields. *Small*, 3(1):126–131, 2007.

[220] Taesung Kim, Ming-Tse Kao, Edgar Meyhöfer, and Ernest F. Hasselbrink. Biomolecular motor-driven microtubule translocation in the presence of shear flow: analysis of redirection behaviours. *Nanotechnology*, 18(2):025101, 2007.

[221] Joseph Bull, Alan Hunt, and Edgar Meyhöfer. A theoretical model of a molecular-motor-powered pump. *Biomedical Microdevices*, 7:21–33, 2005. 10.1007/s10544-005-6168-6.

[222] Kai Nagel and Michael Schreckenberg. A cellular automaton model for freeway traffic. *J. Phys. I France*, 2(12):2221–2229, 1992.

[223] Debashish Chowdhury, Ludger Santen, and Andreas Schadschneider. Statistical physics of vehicular traffic and some related systems. *Physics Reports*, 329(4-6):199 – 329, 2000.

[224] T. Nagata and F. Kumagai. Plant cell biology through the window of the highly synchronized tobacco by-2 cell line. *Methods Cell Sci*, 21:123–7, 1999.

[225] Jan W. Vos, Marileen Dogterom, and Anne Mie C. Emons. Microtubules become more dynamic but not shorter during preprophase band formation: A possible search-and-capture mechanism for microtubule translocation. *Cell Motility and the Cytoskeleton*, 57(4):246–258, 2004.

[226] Jan W. Vos, Aline H. Valster, and Peter K. Hepler. Chapter 21 methods for studying cell division in higher plants. *Methods Cell Biol*, 61:413–37, 1998.

Summary

Why this thesis?

All organisms (plants, animals, fungi and bacteria) are built up from cells. These are the smallest building blocks of an organism that contains its genetic material (DNA). In eukaryotic cells the DNA is stored in the cell nucleus. Eukaryotic cells are membrane bound structures that are filled with cytoplasm and a cytoskeleton. The latter consists of microtubules and filaments that determine the internal organisation of the cell and gives the cell its shape. The cytoplasm consists of cytosol (the liquid component) and membrane bound organelles e.g. vesicles, mitochondria, chloroplasts, peroxisomes, lysosomes, golgi apparatus, cell nucleus, etc.

In this thesis I study the influence of the cytosol on organelle transport in the eukaryotic cell. In particular, I am interested in the phenomena cytoplasmic and axoplasmic streaming. In both these phenomena, many organelles are transported in the same direction over relatively long distances. This molecular cargo transport is powered by molecular motors. These molecular motors are transport proteins that literally walk along the cytoskeleton while carrying a cargo such as an organelle. When a cargo is dragged through the cytosol it will experience resistance in the form of an opposing fluid friction force. The magnitude of this force depends upon the size and shape of the cargo as well as on the viscosity of the fluid. The latter is a physical material property that indicates how strongly a fluid resists deformation. In the cytosol the viscosity is a factor 1000 larger than in water. This means that, in the cell, molecular motors need to deliver a much larger force to obtain the same velocity as in water. However, the motor-cargo velocities measured *in vivo* (in a living cell) are similar to, or even larger than, the single motor velocities from *in vitro* (laboratory environment) experiments in water. The goal of this thesis is to explain the underlying mechanism that makes this possible and to provide a possible explanation for cytoplasmic and axoplasmic streaming.

Molecular Motors

In chapter 1, the molecular motors are introduced. These are proteins that, by hydrolysis of ATP, are capable of converting chemical energy into mechanical work. I am interested in linear motors that walk along cytoskeletal tracks while carrying cargoes such as vesicles or other organelle types. This is called active transport. There are three different families of motor proteins: kinesin and dynein that are associated with microtubules and myosin that walks on actin filaments. In the chapter results from both *in vitro* and *in vivo* experiments are discussed.

The physics

In chapter 2 the fluid dynamics equations are introduced that can be used to describe the motion of molecular motors with cargoes (organelles) in a fluid medium. These equations describe both the transport in solution and along the cytoskeleton. In addition, the forces that are acting upon the motor-organelle complexes and the transport properties are discussed. The latter is treated using dimensionless numbers such as the Reynolds (inertia versus friction forces), Péclet (diffusion versus directed transport) and Stokes (sensitivity to a flow field) numbers. For small objects, such as molecular motors and their cargoes, the friction and thermal forces dominate over inertial forces and over the influence of gravity. This is called a *low Reynolds number* environment, where the fluid motion can be described using the *Stokes equation*. In the course of (active) directed organelle transport along the cytoskeleton, there will be collisions between the organelles and the surrounding fluid molecules. During these collisions momentum is transferred from the organelle to the fluid molecules. The fluid molecules in turn will collide with their neighbours, transfer momentum, etc., etc. This momentum transfer does not continue indefinitely as at each collision a small part of the energy is dissipated. I assume that cytosol is a *Newtonian fluid*, in this type of fluid the magnitude of the momentum transfer decreases linearly with the inverse of the distance. The motion of other organelles, either suspended or bound to the cytoskeleton, will be influenced by the momentum transport via the fluid and vice versa. When many organelles are simultaneously transported in the same direction by molecular motors along the cytoskeleton, then the momentum transfer to the fluid molecules will give rise to a directed fluid flow. This fluid flow will give the bound motors a 'push in the back' making them walk faster along the cytoskeleton. In addition, the suspended organelles will go with the flow resulting in directed motion. In this thesis I investigate if this flow field, driven by momentum transfer, can explain biological phenomena such as cytoplasmic streaming in plants and axoplasmic streaming in neurons. Mathematically, the flow field can be modelled using a hydrodynamic interaction tensor (e.g. using the *Oseen* or the *Rotne-Prager* tensor). Finally, at the end of the chapter, a *Langevin type* equation is introduced. This equation describes the motion of suspended and bound motor-organelle complexes and the hydrodynamic interactions between them. This equation will be solved using computer simulations in chapters 4 and 6.

Models For Molecular Motor Transport

The theoretical models that inspired the simulation models that are introduced in this thesis are reviewed in chapter 3. From these models is learned that a model for molecular motors should include the following features:

- Directed motion of molecular motors along the cytoskeleton.
- Thermal fluctuations (diffusion) of motors attached to the cytoskeleton or in solution.
- Adsorption of motors on, and desorption from, the cytoskeleton.

However, all the models that are discussed neglect the effects of momentum transfer via the fluid. In chapters 4 and 6 two new simulation models are introduced that include all the above features and additionally include the hydrodynamic interactions via the fluid. The two models are a *lattice model* and a *Brownian dynamics* model.

Results

In chapters 4 and 6 computer simulations are presented of a Newtonian fluid embedded between two parallel sections of cytoskeleton with identical polarisation. In the system, the molecular motors with cargoes alternate between periods of directed active transport when bound to the filament and periods of passive diffusion in solution. The switching between these states is driven by the fact the motors can detach from and (re)attach to the cytoskeleton, thus taking the motor processivity into account. In the simulations the motor-cargo complexes are modelled either as hard-spheres (chapter 4) or as soft repulsive hard-spheres (chapter 6). Hence, it is prevented that two motors can occupy the same volume at a given moment in time i.e. excluded volume is taken into account.

The simulations show that the collective effect of the hydrodynamic interactions leads to a substantial increase in the average velocity of motors attached to a filament. This effect is enhanced when the number of active motors in the system increases. Moreover, the momentum transfer leads to a non-negligible, directed flow of suspended organelles. The hydrodynamic coupling is robust enough for suspended objects to flow across gaps in the cytoskeleton. Naturally, the more ordered the environment in the cell, the stronger the effect of the hydrodynamic coupling. Such an ordered environment can be found in cytoplasmic strands that cross the central vacuole in mature plant cells and in axons.

That hydrodynamic interactions can give rise to a flow of suspended material is confirmed in chapter 5 where experiments on the stamen hair cells of the flower *Tradescantia* *virginiana* and of cells of *Nicotiana tabacum* are presented. In these cells cytoplasmic streaming takes place in cytoplasmic strands which are essential transport routes for the distribution of organelles and metabolites. In the strands active directed organelle transport takes place powered by molecular motors. When the molecular motor activity is inhibited then the directed transport changes to a diffusive motion. Using a technique called *Fluorescence Recovery After Photobleaching* (FRAP) it can be determined if there is any fluid flow (and in which direction) present in the cytoplasmic strand. The technique consists of injecting *Green Fluorescent Proteins* (GFP) into the cell's cytosol. Next, the fluorescent material in a small area is destroyed using a laser. Subsequently, the fluorescent recovery in the area is followed i.e. the entry of active GFP. The direction from which the GFP enter the area is an indicator of the direction of fluid flow. If there is no directed fluid flow, the recovery will occur with equal velocity from all directions. However, in the cytoplasmic strands the recovery is observed to take place in the same direction as the active transport. More importantly, suspended organelles are observed to move in the same direction. Thus, both simulations and experiments suggest that momentum transfer through the solution, coming from actively transported cargoes, is the underlying mechanism of cytoplasmic streaming. This is a novel transport mechanism additional to diffusion and active motor transport.

Outlook

The reader is presented with a potential follow-up project in chapter 7. In addition to the linear hydrodynamic interactions between the organelles via momentum transfer, there exist rotational hydrodynamic interactions. Following the same physical mechanism, these interactions give rise to a rotational fluid flow field surrounding the organelles. This mechanism could e.g. be used to explain biological phenomena such as the rotating chloroplasts that have been reported in cytoplasmic drops. Additionally, the mechanism could make accessible all kinds of novel applications for microscopic devices that are interesting for both 'proof-of-principle' experiments and technological applications.

Finally, the results presented in this thesis could be useful for medical researchers to better understand the influence of the fluid medium on organelle transport. This may be important as axonal transport deficiencies are linked to neurodegenerative conditions such as Alzheimer's decease.

Samenvatting

Waarom dit proefschrift?

Alle organismen (planten, dieren, schimmels en bacteriën) zijn opgebouwd uit cellen. Dit zijn de kleinste bouwblokken van een organisme die het genetisch materiaal (DNA) bevatten. Bij eukaryote cellen is het DNA opgeslagen in de celkern. Eukaryote cellen worden omgeven door een celmembraan en zijn gevuld met cytoplasma en een cytoskelet dat is opgebouwd uit microtubuli en microfilamenten die de interne organisatie en vorm van de cel bepalen. Het cytoplasma bestaat zelf uit cytosol (het vloeibare gedeelte) en membraan omgeven organellen zoals vesikels, mitochondria, chloroplasten, peroxisomen, lysosomen, golgi-apparaat, celkern, etc.

In dit proefschrift onderzoek ik het effect dat het cytosol heeft op het transport van organellen binnen de eukaryote cel. In het bijzonder ben ik geïnteresseerd in de fenomenen cytoplasmastroming en axonemaal transport. Voor beide worden veel organellen gericht getransporteerd over relatief grote afstanden. Dit moleculair transport wordt uitgevoerd door moleculaire motoren, dit zijn transport eiwitten die letterlijk over het cytoskelet van de cel lopen terwijl zij een vracht in de vorm van een organel meeslepen. Wanneer de vracht door het vloeistof medium in de cel wordt gesleept zal deze een weerstand in de vorm van vloeistoffrictie ondervinden. De grootte van de weerstand hangt af van de vorm en de afmetingen van het object en van de viscositeit van de vloeistof. De viscositeit is een fysische materiaaleigenschap die aangeeft in welke mate de vloeistof weerstand biedt tegen vervorming. In het cytosol, is de viscositeit een factor 1000 groter dan in water. Dit betekent dat moleculaire motoren in de cel een veel grotere kracht moeten leveren om zich met dezelfde snelheid voor te bewegen als in water. Echter, de motor snelheden die gemeten worden *in vivo* (in een levende cel) zijn vergelijkbaar aan, of zelfs sneller dan, de snelheden gemeten tijdens *in vitro* (laboratorium omgeving) experimenten in water. Het doel van dit onderzoek is te verklaren hoe dit theoretisch mogelijk is en te begrijpen hoe cytoplasmastroming en axonemaal transport plaatsvindt.

Moleculaire Motoren

De moleculaire motoren worden geïntroduceerd in hoofdstuk 1. Dit zijn transport eiwitten die, via de hydrolyse van ATP, chemische energie omzetten in mechanische arbeid. Ik ben geïnteresseerd in lineaire motoren die over het cytoskelet lopen terwijl zij een vracht in de vorm van een vesikel (of andere soorten organellen) meedragen. Dit wordt actief transport genoemd. Er zijn drie verschillende families van transport eiwitten: kinesine, dyneine en myosine. De eerste twee worden geassocieerd met microtubuli terwijl myosine over actinefilamenten loopt. In het hoofdstuk worden resultaten van zowel *in vitro* als *in vivo* experimenten besproken.

De natuurkunde

In hoofdstuk 2 worden de vergelijkingen van de vloeistof dynamica geïntroduceerd waarmee de beweging van moleculaire motoren met vracht in een vloeistof kunnen worden beschreven. Deze vergelijkingen beschrijven zowel het transport van de motoren en organellen in oplossing als het transport over het cytoskelet. Het hoofdstuk besteedt ook aandacht aan de krachten die worden uitgeoefend op deze organellen en de eigenschappen van de stroming. Deze zullen besproken worden aan de hand van dimensieloze kentallen zoals het Reynolds getal (inertie versus frictie), Péclet nummer (diffusie versus gericht transport) en Stokes getal (de gevoeligheid voor een stromingsveld). Voor kleine objecten, zoals organellen, domineren de frictie- en thermische krachten over inertie en de zwaartekracht. Dit is een zogenaamde *lage Reynolds getallen* omgeving, waar de beweging van de vloeistof kan worden beschreven door middel van de *Stokes vergelijking*. Tijdens het gerichte organel transport over het cytoskelet zullen er botsingen plaatsvinden tussen het organel en de omringende vloeistofmoleculen. Gedurende deze botsingen wordt impuls overgedragen naar de vloeistofmoleculen. Deze vloeistofmoleculen botsen op hun beurt weer met andere moleculen, etc., etc. De impulsoverdracht gaat niet oneindig door, bij elke botsing gaat een klein deel van de energie verloren. Wij nemen aan dat cytosol een Newtonse vloeistof is, in dit type vloeistof neemt de impulsoverdracht in kracht af met de inverse van de afstand. De beweging van andere organellen, in suspensie of gebonden aan het cytoskelet, zal worden beïnvloed via deze impulsoverdracht en vice versa. In het geval dat er veel organellen door moleculaire motoren in dezelfde richting over het cytoskelet worden gesleept, dan zal dit een gerichte vloeistofstroming tot gevolg hebben. Deze vloeistofstroming zorgt ervoor dat de gebonden organellen een duwtje in de rug krijgen en sneller gaan lopen over het cytoskelet. Aanvullend zullen ook de vrije organellen in de vloeistof met de stroom meegaan. In dit proefschrift onderzoek ik of dit stroomveld, opgewekt door impulsoverdracht, biologische fenomenen als cytoplasmastroming in planten en axonemaal transport in neuronen kan verklaren. Het stroomveld kan wiskundig worden opgelost met behulp van een hydrodynamische interactie tensor (bijvoorbeeld met de *Oseen*- of de *Rotne-Prager* tensor). Tenslotte wordt aan het eind van dit hoofdstuk een

Langevin type vergelijking geïntroduceerd. Deze vergelijking beschrijft zowel de beweging van gesuspendeerde en gebonden organellen als de hydrodynamische interacties tussen de organellen. Deze vergelijking zal worden opgelost middels computersimulaties in de hoofdstukken 4 en 6.

Transport modellen voor moleculaire motoren.

In hoofdstuk 3 staat een overzicht van de theoretische modellen voor moleculaire motoren waarop de simulatie modellen, die worden gebruikt in de hoofdstukken 4 en 6, zijn gebaseerd. De belangrijkste eigenschappen die met deze modellen worden beschreven zijn:

- Gericht transport van moleculaire motoren over het cytoskelet.
- Thermische fluctuaties (diffusie) van de organellen in oplossing en op het cytoskelet.
- Adsorptie van motoren aan en desorptie van het cytoskelet.

Al deze modellen verwaarlozen echter het effect dat impulsoverdracht via de vloeistof heeft op het transport. In de hoofdstukken 4 en 6 worden twee nieuwe simulatie modellen geïntroduceerd die al de bovenstaande eigenschappen hebben en aanvullend ook de hydrodynamische interacties via de vloeistof meenemen. De modellen zijn een *rooster model* en een *Brownse dynamiek model*.

Resultaten

In de hoofdstukken 4 en 6 worden computersimulaties gepresenteerd van een Newtonse vloeistof die ingesloten is tussen twee parallelle segmenten van het cytoskelet. In het systeem alterneren de moleculaire motoren met lading tussen periodes van gericht actief transport over het cytoskelet en diffuus passief transport in de vloeistof. Dit wordt gedreven door desorptie van gebonden motoren van, en absorptie van motoren aan, het cytoskelet. De motoren met vracht worden gemodelleerd als harde bollen (hoofdstuk 4) of als harde bollen omringd door een repulsieve schil (hoofdstuk 6). Op deze manier wordt voorkomen dat twee bollen op hetzelfde moment dezelfde plaats innemen.

De simulaties tonen aan dat het collectieve effect van de hydrodynamische interacties een substantiële toename van de gemiddelde motor snelheid op het cytoskelet tot gevolg heeft. Dit effect wordt versterkt als het aantal motoren met lading op het cytoskelet toeneemt. Tevens leidt de impulsoverdracht in de vloeistof tot een niet verwaarloosbare gerichte stroom van gesuspendeerde organellen. De hydrodynamische koppeling is zelfs robuust genoeg om organellen over gaten in het cytoskelet heen te laten stromen. Uiteraard zal de kracht van dit effect sterker zijn naarmate het systeem meer geordend is. Een voorbeeld van een geordend systeem zijn de draden van cytoplasma die de centrale vacuole doorkruisen in volwassen planten cellen en in axonen.

Dat hydrodynamische interacties leiden tot een gerichte stroom van gesuspendeerd materiaal is bevestigd in hoofdstuk 5. Hier worden experimenten gepresenteerd in cellen van haartjes op de meeldraad van de bloem *Tradescantia virginiana* en in cellen van *Nicotiana tabacum*. In deze cellen vindt cytoplasmastroming plaats in draden gevuld met cytosol die dienen als transport routes voor de distributie van organellen en metabolieten. In de draden worden organellen gericht getransporteerd via moleculaire motoren. Als het transport van de moleculaire motoren wordt gestopt, door gebruik te maken van een inhibitor, wordt dit transport overgenomen door diffusie en stopt het transport. Middels een techniek genaamd *Fluorescence Recovery After Photobleaching* (FRAP) wordt de stromingsrichting van het cytosol in de draad onderzocht. In deze techniek worden groen fluorescente eiwitten (GFP) in de cel geïnjecteerd. Vervolgens wordt een klein gebied met een laser bestraald waarbij het fluorescente materiaal kapot gaat. De richting waaruit het GFP terugkeert in het bestraalde gebied geeft aan in welke richting de vloeistof stroomt. Zonder gericht transport (geen stroming) zal dit herstel met gelijke snelheid uit alle richtingen tegelijk plaatsvinden. Echter, in de draden vindt het herstel in dezelfde richting plaats als het actieve organel transport via transport eiwitten. Belangrijker nog, gesuspendeerde organellen bewegen ook in deze richting. Zowel de computersimulaties als de experimenten suggereren dat impulsoverdracht van de actief getransporteerde organellen naar de vloeistof het onderliggende mechanisme is achter cytoplasmastroming. Dit is een nieuw transport mechanisme naast diffusie en actief motor transport.

Mogelijke toepassingen

In hoofdstuk 7 wordt een potentieel vervolg project gepresenteerd. Naast de lineaire hydrodynamische interacties tussen de organellen via impuls overdracht bestaan er ook rotationele hydrodynamische interacties. Deze interacties, die gebaseerd zijn op hetzelfde fysische mechanisme, veroorzaken een rotationele stroming rondom de organellen. Dit mechanisme zou kunnen worden gebruikt om biologische fenomenen te verklaren zoals bijvoorbeeld de roterende chloroplasten die zijn geobserveerd in druppels cytoplasma. Ook zou dit mechanisme nieuwe applicaties voor microfluidische apparaten apparaten mogelijk kunnen maken. Dit is interessant voor zowel bewijs van concept experimenten als voor technologische toepassingen.

Tenslotte, kunnen de resultaten die gepresenteerd zijn in dit proefschrift, medische wetenschappers helpen om beter te begrijpen welke rol het vloeistof medium speelt bij organel transport in neuronen. Dit kan belangrijk zijn aangezien afwijkingen in axonemaal transport samengaan met neurodegeneratieve condities zoals Alzheimer.

Acknowledgements

'A perfect circle of acquaintances and friends'.

R.E.M. - Perfect Circle

“Het proefschrift is af”. Voordat ik naar Australië verhuisde dacht ik dat ik deze woorden nooit zou uitspreken. Deels uit frustratie dat ik het niet eerder afgemaakt had, deels uit hervonden motivatie en deels gedwongen door de economische crisis ben ik in 2011 opnieuw begonnen. Waarom het mij in de eerste periode niet gelukt is? Ik denk dat ik er toen nog niet klaar voor was. Waarom het nu wel is gelukt? In de tussenliggende jaren ben ik gegroeid als persoon, heb ik geleerd hoe ik bij zo een groot en overweldigend project het overzicht en rust kan bewaren, en heb ik de juiste mensen om mij heen verzameld. Ik ben gedurende de twee perioden (2003-2007, 2011-2012) waarin dit proefschrift tot stand is gekomen door veel mensen geholpen. Dit hoofdstuk is geschreven om hen te bedanken.

Erika, mijn dagelijkse begeleider, bedankt voor je engelengeduld en onvoorwaardelijke steun. Ondanks de lange duur van dit promotietraject ben jij altijd in de goede uitkomst van dit project blijven geloven. Jouw kennis, inzicht en enthousiasme waren onmisbaar. Het was niet altijd eenvoudig om op afstand de hoofdstukken en resultaten te bespreken, zeker gezien het tijdsverschil tussen Engeland en Australië maar het is ons gelukt.

Prof. dr. B. Jérôme, Blandine, mijn oorspronkelijke promotor, bedankt voor je steun gedurende de eerste periode dat ik aan mijn proefschrift werkte. Ik heb veel van je geleerd. Ik wil je ook graag bedanken dat je hebt toegestaan dat Evert Jan het van je overgenomen heeft. Mijn promotor, Prof. dr. E.J. Meijer, Evert Jan, bedankt dat je mij zo laat in het promotietraject als promovendus hebt geaccepteerd. Ik heb veel geleerd van de feedback die jij mij gedurende de jaren van het promotietraject hebt gegeven. Dr. C.P. Lowe, Christopher, thank you for all your input into this project and for our fruitful discussions.

Prof. dr. I. Pagonabarraga, Ignacio, thank you for endless discussions about the project, for being a great mentor, always pleasant, friendly and patient, in short a fantastic person. You have gone out of your way to help me and I wouldn't have been able to finish the thesis without your unconditional support and advice.

De overige leden van de promotiecommissie: Prof. dr .ir. P.J. Schoenmakers, Prof. dr. A.M.C. Emons, Prof. dr. A.M. Brouwer and dr. C. Storm. Ik wil jullie graag bij dezen bedanken voor het kritisch bestuderen van dit proefschrift.

Prof. dr. Daan Frenkel was diegene die met het idee kwam voor het onderzoek in dit proefschrift. Bedankt hiervoor.

UVA: Javier, jij was altijd een bron van gezelligheid, informatie en positieve energie op kantoor en daarbuiten. Ik ben blij dat je een goede vriend bent geworden. Un abrazo fuerte (y a Alex también)! Nienke, ik leerde je eigenlijk pas echt kennen na mijn tijd bij de UvA. Onze etentjes, eindeloze gesprekken en uitstapjes naar bevrijdingspop en Haarlem jazz waren geweldig. Maya for bringing life, drama and excitement to the office. Marco, for sharing an office and for always being friendly and helpful, I wish we had spend more time together, Peter V. voor support en mooie DVD's, Petra voor reflectie en wandelingen tijdens lunchtijd, Maikel en Daniel die mij af en toe een duw in de juiste riching gaven, Jürg bij wie ik mijn eerste project aan de UvA deed, Gooitzen, Peter B., Berend, Gadi, Annalisa, Prof. Krishna, Renate, Nicole, AIO's, post-doc's, HIMS staf, en overige collega's.

Barcelona: *El Departament de Física Fonamental* at la Universitat de Barcelona, thank you for supplying me with an office and allowing me to use your facilities. Manel for being a great friend and who was always there to help me. Nikos for great fun and for abusing the Spanish language, and finally Eva, Anna, Segundo, Isabel and Marc who made it possible for me to live, study and work in Barcelona. Thank you so much for your opening your home to me.

Wageningen: Thank you Anne-Mie and Agnieszka for helping me find the experimental piece of the puzzle. Our discussions were invaluable. Moreover, I had a great time visiting you in Wageningen.

Ook ben ik mijn voormalige collega's bij Neville Chemical Europe B.V. (nu Rütgers Resins B.V.) niet vergeten. Bedankt dat jullie mij de vrijheid en het ver-trouwen hebben gegeven om mij verder te ontwikkelen. Zonder deze ervaring was dit proefschrift er niet gekomen. Allereerst Gert, de ideale mentor, kantoorgenoot en goede vriend, Marcel H. een geweldige vent en vriend met wie ik heerlijk kon sparren en lachen om wat er nu weer was gebeurd, Ruud K. voor motivatie ("Maak in hemelsnaam dat proefschrift af!") en onvoorwaardelijke steun, Marcel de K. die ervoor zorgde dat ik snel weer vergeten was, Ruud V. die ook het lef had zijn gevoel te volgen, Mischa en Ron voor foute praat op vrijdagmiddag, Peter voor de mooie verhalen en Paula en Kim die altijd voor mij klaarstonden, Gerard H. van wie ik op de valreep nog veel geleerd heb, Chris die vanaf dag één in mij geloofde en Humphrey voor coaching en reflectie, Daniëlle voor feedback en prettige gesprekken. En dan zijn er natuurlijk nog de geweldige mensen op het lab, technische dienst, Shiftleaders, Process Operators, ICT-team en wie ik ook vergeten mocht zijn. Als laatste wil ik Rob van Pernis van Koppers bedanken omdat hij mij de kans gaf om management ervaring op te doen.

USC: Ik heb hier veel geleerd over mijn lichaam en ook hoe zelfverzekerd voor een groep te staan als sportinstructeur. Bedankt Josta, Miriam en Sin Mee voor de feedback. Ik pas dit ook in het dagelijks leven toe en heb hier vooral als projectleider veel aan gehad. Bedankt USC dat ik als spinning en bodyshape instructeur zoveel mooie ervaringen op mocht doen. Rolf, Michiel en Jan-Marc, het was altijd prettig om met jullie samen te werken op het PCH, en natuurlijk ook met mijn andere collega's binnen de groepsfitness. Dan nog een speciaal woord voor Maurice en Gabriela (te echo de menos chica!), ik heb altijd genoten van de hardloop training en heb nog steeds plezier van wat ik van jullie heb opgestoken. Frank Cabooter, bedankt dat je mij deed inzien dat dit proefschrift er alleen maar zou komen als ik het voor mijzelf zou doen en daar de motivatie uit zou halen.

AMS Instrumentation and Calibration: Thank you for welcoming a Dutchman in your family business. I appreciate that you have given me the opportunity to further develop my Project Management skills from a commercial perspective. Thank you Dirk, Thomas, Mike, Jon, Angela, Lawrence, Andrew, Kerry, Anna, Karen, Brian, Richard, Elie, the interstate boys and neighbours at Trimec Flow Products.

My friends: Thomas, dearest Tomboy, I miss our lengthy discussions, watching Robotech, dinners and long runs on the weekend. Meeting you made my life in Amsterdam infinitely better. Simon, we keep on popping in and out of each other's lives no matter where we are. Your great sense of humour, lust for adventure and beer, made safaris in Tasmania, the Canadian Rockies or in any random bar quite the experience. Jana (Janka) for always being a great friend with whom I had heaps of great conversations and good laughs. Daan, je dronk je allereerste biertje met mij en er zouden er nog een paar volgen. Met de jaren werden de nachtelijke avonturen vervangen door avondvullende etentjes en er zat geen saaie avond tussen. Robin, de broer die ik nooit heb gehad, je was overal bij. Bedankt dat je mij laat lachen tot het pijn doet, altijd open staat voor gekke avonturen, en mij altijd mezelf laat zijn. Ik mis je heel erg hier in Australië. En dan natuurlijk nog Diana, Helene, Iris en wie ik ook maar vergeten mocht zijn.

Mijn familie: Rob voor de vriendschap en de mooie concerten in Melkweg en Paradiso, Lenneke voor de fijne gesprekken en etentjes, John die mij het beeldverhaal leerde kennen, die dingen soms beter begrijpt dan anderen en mij meenam naar de duinen, Peter die mij leerde open te staan voor mensen die anders zijn en die tevens verantwoordelijk is voor een deel van de titel van dit proefschrift, oma Gaartman bij wie ik altijd welkom ben en die nog steeds alle spelletjes wint, opa Gaartman met wie ik heerlijk gelachen heb, mijn opa en oma Houtman die mij de mooiste vakanties gaven die een kind zich maar kan wensen, André, neefjes en nichtjes voor gezelligheid als we elkaar zien.

My support crew in Australia: Clare for cupcakes, adventures in Tasmania and nice musicals, Brett for beers, and interesting discussions on the academic world, Caroline for great fun, laughter and dinners, Lance, the semi-Dutchman, for burgers and a multitude of films that are long forgotten before you even leave the theatre, Heather and Peter for lovely runs and conversations. Melbourne University Athletics Club, and in particular Hamish and Tony, for the great atmosphere, fantastic training sessions and for giving me the opportunity to coach the beginner squad.

Mijn lieve ouders, aan jullie dank ik wie ik ben. Ik weet dat ik jullie met mijn vertrek naar Australië veel verdriet heb gedaan. Niemand heeft zo een groot offer gebracht als jullie en ik zal dat nooit vergeten. Bedankt voor alles.

My extended family in Australia: Ross and Libby without whom this thesis would never have been completed. Your love, understanding, patience and unconditional support were invaluable. Charlotte for great laughs, adventures and holidays. Chad, your drive and positivity are contagious. Hammie and Saffie for being great companions. The rest of the Knight family for adopting a Dutchman and making him feel at home. And most importantly Georgia. With your sense of humour, our shared interests in cooking, music, sports, travelling and your endless support and encouragement you have made all the difference. I am forever in your debt.

About the author

Dion Houtman was born in Haarlem, the Netherlands on October 28^{th} 1977. After finishing high school he studied MBO Procestechniek at the *Nova-College* in Santpoort-Noord. He followed this with a BSc. in Chemical Technology at the *Hogeschool van Amsterdam* and a MSc. Chemical Engineering at the *University of Amsterdam*. The latter he finished cum laude (with distinction). The Master's thesis titled 'Modelling hydrodynamic interactions between molecular motors' was written in Barcelona during an academic exchange at the Universitat de Barcelona under supervision of dr. Erika Eiser and Prof. dr. Ignacio Pagonabarraga.

From 2003 till 2007, Dion worked on his PhD thesis at the *University of Amsterdam, Van 't Hoff Institute for Molecular Sciences* in the *Complex Fluids group* under supervision of dr. Erika Eiser. The research was performed in close collaboration with Prof. dr. Ignacio Pagonabarraga of the Universitat de Barcelona and dr. Agnieszka Esseling-Ozdoba and Prof. dr. Anne Mie C. Emons of Wageningen University. This resulted in two publications.

At the end of his contract Dion left the University of Amsterdam with the PhD-thesis pending to pursue a career in industry. After having worked as Process Engineer for 3 years at *Neville Chemical Europe B.V.* (first seconded via *XDES Projects B.V.*) he emigrated in December 2010 to Australia where he currently resides in Melbourne.

In Melbourne he took a professional sabbatical to complete the thesis by adding original research, performing an extensive literature search and writing it all down. The work and results of the full PhD-project are presented in this thesis.